Master's thesis
Master's Programme in Particle Physics and Astrophysical Sciences
Particle Physics and Cosmology

The nature of moving solar radio bursts associated with coronal mass ejections

Juska Räsänen
April 5, 2021

Supervisors: Diana E. Morosan,
Emilia K. J. Kilpua

Examiners: Diana E. Morosan,
Emilia K. J. Kilpua

UNIVERSITY OF HELSINKI
DEPARTMENT OF PHYSICS

PL 64 (Gustaf Hällströmin katu 2a)
00014 University of Helsinki

HELSINGIN YLIOPISTO — HELSINGFORS UNIVERSITET — UNIVERSITY OF HELSINKI

Tiedekunta — Fakultet — Faculty	Laitos — Institution — Department
Faculty of Science	Department of Physics

Tekijä — Författare — Author

Juska Räsänen

Työn nimi — Arbetets titel — Title

The nature of moving solar radio bursts associated with coronal mass ejections

Oppiaine — Läroämme — Subject

Particle Physics and Cosmology

Työn laji — Arbetets art — Level	Aika — Datum — Month and year	Sivumäärä — Sidantal — Number of pages
Master's thesis	April 2021	84

Tiivistelmä — Referat — Abstract

Coronal mass ejections (CMEs) are large-scale eruptions of plasma entrained in a magnetic field. They occur in the solar corona, and from there they propagate into interplanetary space along with the solar wind. If a CME travels faster than the surrounding solar wind, a shock wave forms. Shocks driven by CMEs can act as powerful accelerators of charged particles. When charged particles like electrons are accelerated, they emit electromagnetic radiation, especially in the form of radio waves.

Much of the radio emission from CMEs comes in the form of solar radio bursts. Traditionally solar radio bursts are classified into five types, called type I–V bursts, based on their characteristics and appearance in a dynamic spectrum. Of these five types of bursts, especially type II radio bursts are believed to be signatures of shock waves in the corona and interplanetary space. There are, however, also radio bursts associated with CMEs and shocks that do not fit the description of any of the five standard types of radio bursts.

In this thesis three moving radio bursts associated with a CME that erupted on May 22, 2013 are identified and studied in detail. The characteristics of the bursts do not match those of the usual five types of solar radio bursts. The aim of the work is to ascertain the emission mechanism that causes the observed radio bursts, as well as locate the sites of electron acceleration that are the sources of the emission. The kinematics and the spectral features of the emission are studied in order to find answers to these questions.

Analysis of the spectral features of the moving bursts showed that the bursts were emitted via plasma emission. Analysis of the kinematics revealed that the moving radio bursts originated unusually high up in the corona from the northern flank of the CME. The CME studied in this work was preceded by another one which erupted some hours earlier, and the disturbed coronal environment likely caused the radio emission to be emitted from an unusual height. It was found that the bursts likely originated from electrons accelerated at the shock driven by the CME.

Avainsanat — Nyckelord — Keywords

solar physics, coronal mass ejection, solar radio burst

Säilytyspaikka — Förvaringsställe — Where deposited

Kumpula Campus Library

Muita tietoja — Övriga uppgifter — Additional information

Contents

1 Introduction

Coronal mass ejections (CMEs) are the most extreme phenomena in the Solar System. They expel energetic plasma from the corona into interplanetary space, sometimes with speeds exceeding thousands of kilometers per second. When the ejected plasma moves at a speed sufficiently greater than that of the surrounding solar wind, a shock wave forms in front of it. These shock waves, or shocks, can act as highly efficient particle accelerators. The efficiency of this particle acceleration depends for example on the orientation of the shock relative to the surrounding magnetic field. The accelerated charged particles emit electromagnetic radiation, often in the form of radio waves.

Radio emission is ubiquitous on the Sun. In addition to the constant background emission provided by the quiet Sun, the Sun also produces radio bursts, which are relatively short-lived and can be very intense. These bursts are especially associated with active regions, solar flares and CMEs. For example bursts known as type II radio bursts are believed to be caused by electrons accelerated by shocks driven by flares and CMEs.

Type II bursts are one of the five types of radio bursts, which have been widely studied since the 1960s. There are, however, solar radio bursts, which do not fit the descriptions of any of these five types. Examples of these are radio spikes (e.g., Benz et al. 1996; Melnik et al. 2014), solar S-bursts (e.g., Clarke et al. 2019), and supershort radio bursts (e.g., Magdalenić et al. 2006). Solar radio bursts can also be classified as moving or stationary, depending on whether their source regions appear to propagate through the corona or stay in the same location for the entire lifetime of the burst.

In this thesis a detailed study of moving radio bursts that do not appear to match the characteristics of any of the usual five types of solar radio bursts is presented. A set of moving radio bursts were observed in conjunction with a fast CME that erupted on May 22, 2013. In addition to the moving radio bursts the CME was accompanied for example by type II radio bursts. The aim of this thesis is to investigate the cause of these atypical bursts, the emission mechanism behind them, and where their source regions are in relation to the CME and/or the shock driven by it. These questions are answered by studying the kinematics and the spectral features of the moving

bursts. To determine the source regions of the bursts their locations are compared with imaging from other instruments. The kinematics are also compared with the kinematics of the CME and related radio emission from previous studies. The analysis is conducted in Python, with code that was in parts written by the author of this thesis, and in parts adapted from existing code.

This thesis is divided into two parts. The first part, consisting of Chapters 2 – 4, contains the necessary background information and theory. Then the second part, consisting of Chapters 5 – 7, describes the methods and results of the analysis conducted for the thesis.

In Chapter 2 coronal mass ejections are introduced, their general properties are presented, and their kinematic evolution in the corona and beyond is described. A brief introduction to magnetohydrodynamic shocks, such as ones driven by CMEs, follows. The chapter closes on a discussion of one important mechanism by which charged particles like electrons are accelerated at shock fronts, called shock drift acceleration. Then, Chapter 3 goes through properties of solar radio emission, and the emission mechanisms most relevant for CMEs are introduced. The chapter also contains descriptions of two important types of radio bursts, type II and type IV bursts. In Chapter 4 concepts relating to measuring radio emission are discussed. The units used in the thesis are also explained. Finally, the spectral index is introduced as a diagnostic tool that can be used to probe the possible emission mechanism of observed radio emission.

Chapter 5 describes the data, the CME that is studied and the different methods employed in the analysis of the radio emission associated with the CME. In Chapter 6 the results of the analysis are presented. Finally, Chapter 7 concludes the thesis by summarizing the findings, discussing them and relating them to earlier studies. Possible avenues of future research are also considered.

2 | Coronal mass ejections

Coronal mass ejections are the largest disturbances occurring in the solar atmosphere. They consist of plasma eruptions entrained in a magnetic field propagating outwards through the corona and into the heliosphere. They are capable of driving shock waves in the corona and interplanetary space. These shocks are powerful accelerators of charged particles and thus are sources of electromagnetic radiation.

This chapter introduces coronal mass ejections and describes their properties and their evolution in the corona and beyond. Then, a general introduction to magnetohydrodynamic shocks is given, followed by a description of shock drift acceleration, which is one important mechanism by which charged particles are accelerated by coronal and interplanetary shocks.

2.1 What is a coronal mass ejection?

A coronal mass ejection (CME) is a large expulsion of plasma, magnetic field and energy from the Sun into the heliosphere (Webb and Howard 2012). CMEs are the most energetic and the largest-scale phenomenon in the Solar System, and as such they are the primary drivers of heliospheric disturbances and of space weather near the Earth. Though their study is understandably confined to our own home star, CMEs have been observed on other stars as well (e.g., Argiroffi et al. 2019).

CMEs are most often observed in white light using a coronagraph, which is an instrument that blocks out the photosphere in order to make the orders of magnitude less bright corona visible. CMEs do not themselves radiate visible light. Rather, light originating in the photosphere is Thomson scattered[1] off the free electrons in

[1]Thomson scattering is the elastic scattering of electromagnetic radiation by a charged particle, e.g., an electron. In Thomson scattering electromagnetic radiation incident on a charged particle is absorbed by the particle. Absorbing the light accelerates particle, which in turn causes it to emit electromagnetic radiation. The energy of the incident radiation is assumed to be so low compared to the rest energy of the particle that momentum transfer between them can be ignored. As a result, the wavelength of the radiation emitted by the particle is the same as that of the incident radiation, and the radiation appears to have scattered off the charged particle (Howard 2011).

the plasma expelled along the CME into the solar wind, and this is the light that is observed. In addition to white light CMEs can also be seen at soft X-ray and extreme ultraviolet (EUV) wavelengths (Priest 2014). And, importantly for this thesis, as CMEs accelerate charged particles to high energies, they are powerful sources of radio emission. CME structures have even been directly imaged at radio wavelengths (Bastian et al. 2001; Maia et al. 2007).

A white-light example of a CME can be seen in Figure 2.1, which shows an image of a CME taken by the *Large Angle Spectroscopic Coronagraph* (LASCO; see Section 5.1.4) C3 coronagraph on board the *Solar and Heliospheric Observatory* (SOHO). The image also demonstrates the scale to which CMEs can extend, even dwarfing the Sun (indicated in the image by the white circle in the middle) by many times. What the image also highlights well is the so-called "classic" three-part structure of a CME, first identified by Illing and Hundhausen (1983, 1985). This kind of CME consists of a bright core, followed by a dark (low density) region known as a cavity, and having a bright looplike outer edge. Though widely considered to be the "classic" structure of a CME, only about 30 percent of recorded CMEs have this structure (Priest 2014).

As mentioned above, CMEs can significantly impact space weather near the Earth and affect the Earth's magnetosphere. Most geoeffective CMEs originate close to the center of the solar disk. In such a case, if observed by a spacecraft on the Sun–Earth line, the CME appears to surround the occulting disk of the coronagraph, and is known as a *halo CME*. Figure 2.2 shows an image of a halo CME taken by the LASCO C2 coronagraph.

According to a statistical study conducted by Gopalswamy et al. (2007) most halo CMEs that erupt from the side of the Sun visible to the Earth are geoeffective, with those erupting from the disk (source longitude within 45° of the central meridian) being more likely to be geoeffective than those erupting from the limb (source longitude $45° < \phi < 90°$ from the central meridian). They also found that intense geomagnetic storms are mostly due to disk halo CMEs. Halo CMEs that are Earth-directed constitute only a few percent of all erupted CMEs (Gopalswamy et al. 2007; Howard 2011).

Though halo CMEs are widely believed to be nothing but normal CMEs that happen to propagate in a direction that gives them the appearance of a halo (Chen 2011), their average apparent speed is twice that of "normal" CMEs (Yashiro et al. 2004). There is no consensus on whether this difference stems from factors related to projection effects in the observations or if halo CMEs are somehow different from non-halo CMEs. They could for example be the combination of the CME and a shock wave driven by it (Chen 2011).

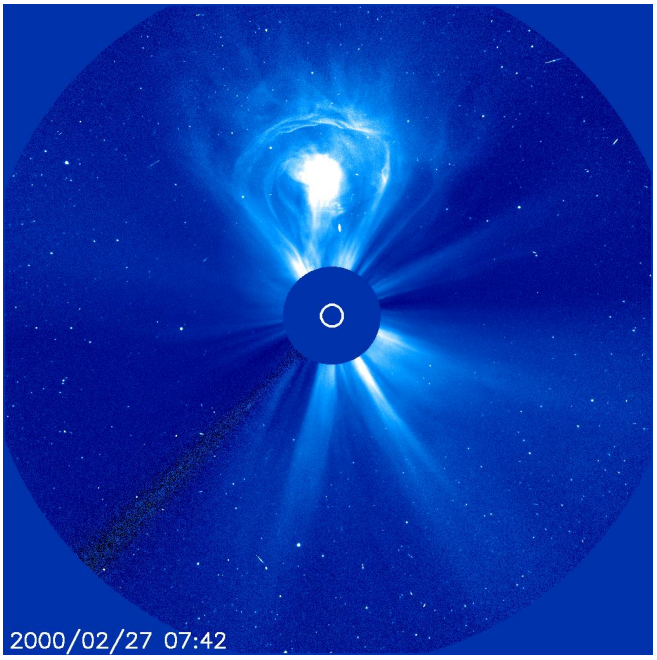

Figure 2.1 An image of a CME that erupted on February 27, 2000, taken by SOHO/LASCO C3. The blue disk in the middle is the occulting disk, which blocks out the Sun, which is indicated by the white circle. Image courtesy of NASA/ESA.

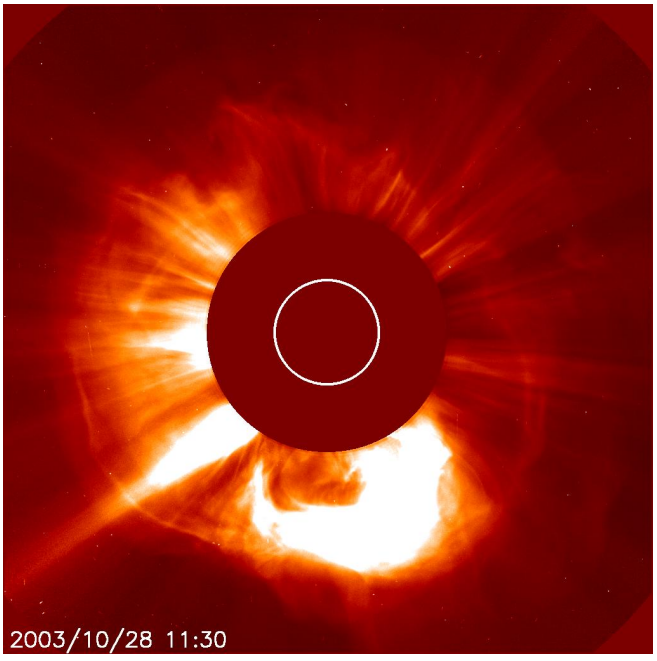

Figure 2.2 An image of a halo CME observed on October 28, 2003, taken by SOHO/LASCO C2. Image courtesy of NASA/ESA.

2.2 Properties of coronal mass ejections

Thousands of CMEs have been observed since their discovery in late 1971 (Howard 2006), most of them by LASCO on board SOHO, which was launched in 1995. In the interval from 1996 to the end of 2008 LASCO observed over 14 000 CMEs (Howard 2011), and it continues observing the Sun to this day. From the data provided by LASCO and many other coronagraphs that were sent into space before or have been sent after it, the physical properties of CMEs such as mass, speed, width, and location (relative to the solar disk) have been ascertained in large-scale statistical studies.

Based on LASCO data the average mass of a CME is around 1.3×10^{12} kg, though it can be as much as 4.4×10^{12} kg (Vourlidas et al. 2010, 2011). The Sun loses about 10^{14} kg of mass every day to the solar wind (Cargill and Harra 2007), so the contribution of a typical CME to this mass loss is a few percent. The measured speeds[2] of CMEs are widely distributed, ranging from speeds as low as 35 km s^{-1} (Hundhausen et al. 1994) for the slowest events all the way to over 3000 km s^{-1} (Gopalswamy et al. 2014) for some extremely fast events. Most CMEs, however, accelerate or decelerate towards the speed of the ambient solar wind, which is typically between ~300 km s^{-1} and ~800 km s^{-1}, as they propagate outwards from the corona. Indeed, in most statistical studies the average speed of a CME falls somewhere in the neighborhood of 400 km s^{-1} (e.g., Hundhausen et al. 1994; Yashiro et al. 2004). Properties like the mass, speed, and energy of a CME are dependent on the level of solar activity. Studying over 7800 CMEs that were recorded by LASCO over a full solar cycle, Vourlidas et al. (2010, 2011) found that for example the average speed of a CME ranged from about 210 km s^{-1} around solar minimum to about 490 km s^{-1} around solar maximum. Depending on their initial speed and the acceleration or deceleration they experience in interplanetary space, CMEs usually take anywhere from less than a day to a few days to arrive to the orbit of the Earth (Kilpua et al. 2019).

The rate of occurrence of CMEs has also been well documented in these statistical studies. The number of erupting CMEs is also dependent on the level of solar activity and varies over the 11-year solar cycle. During solar minimum CMEs occur on average once every two days, meaning 0.5 CMEs per day, while during solar maximum as many as 6 CMEs can erupt per day (Cargill and Harra 2007). The source location of a CME also depends on the solar cycle. During solar minimum most

[2]What is recorded in white-light coronagraph images, from which these properties were derived, is the projection of a CME in the plane of the sky, which is the plane passing through the center of the Sun and which is normal to the Sun–observer line. This means that properties like speed are subject to projection effects, and what is measured is not the true speed but the "apparent speed". This is the speed that the CME would have if it erupted from the solar limb into the plane of the sky. Since most of the CMEs erupt from somewhere other than the solar limb, the apparent speed is an underestimate of the true speed of the ejection. It has been argued, however, that in most cases this underestimation is less than 18 % of the true speed of the CME (Hundhausen et al. 1994). Similarly, the apparent width of a CME is an overestimate of the actual width, if the CME erupts off-limb (Webb and Howard 2012).

CMEs erupt from around the equator, whereas during solar maximum they are seen to erupt from all latitudes (Yashiro et al. 2004).

2.3 Kinematic evolution of a CME

It is known that CMEs originate in the low corona, but the exact physical mechanisms responsible for their onset and evolution are not known. It is, however, clear that CME onset and early evolution are magnetically driven phenomena (Howard 2011). It is also accepted that CME acceleration happens primarily in the low corona, below $2\,R_\odot$ (Priest 2014), but once the CME clears the corona and continues to propagate through the heliosphere, the mechanism that propels it forward is not well understood (Howard 2011).

While there is no consensus on what exactly causes the onset and acceleration of a CME, what is well understood from observations is the kinematic evolution of a CME (Zhang and Dere 2006; Zhang et al. 2001). The evolution can be divided into three phases: *initiation*, *acceleration*, and *propagation*. Figure 2.3 shows schemati-

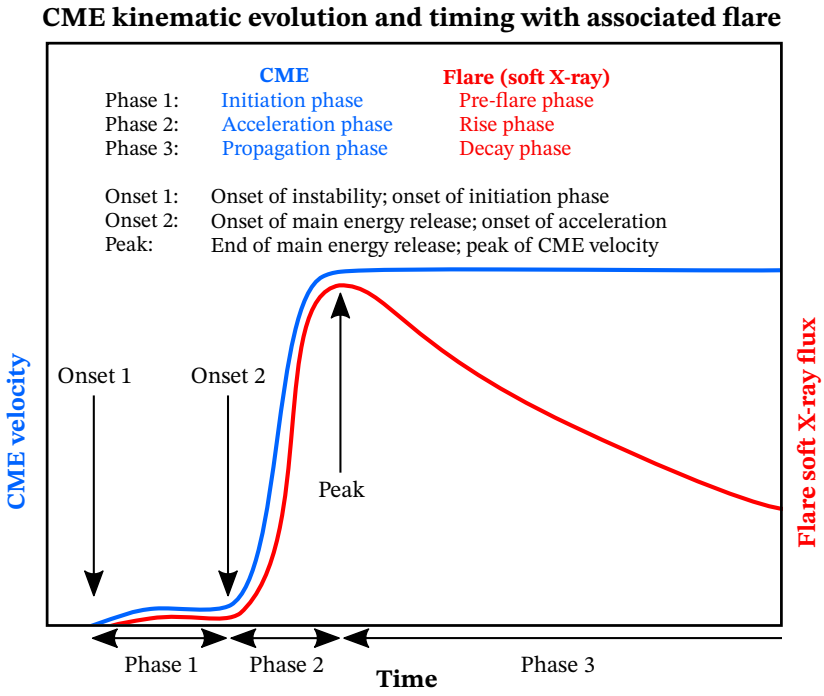

Figure 2.3 Schematic plot showing the three-phase kinematic evolution of a CME and how it is related to the evolution of a solar flare as measured by its soft X-ray flux. The three phases of the CME evolution are initiation, acceleration, and propagation. These correspond to the pre-flare, rise, and the decay phases of a solar flare, respectively. Usually the CME achieves its peak velocity when the flare reaches its peak flux. Adapted from Zhang and Dere (2006).

cally how the velocity of a CME changes as it goes through these phases. The figure also shows the temporal correlation that has been observed (e.g., Zhang et al. 2001) between the evolution of a CME and that of a soft X-ray flare, if the CME is accompanied by one.

Figure 2.3 shows that after the initial phase, during which there is only a small gain in velocity, the velocity of the CME increases greatly in a short period of time. However, this is not true for all CMEs. Some CMEs show extremely impulsive acceleration, which is strong and happens over a relatively short period of time, while others may evolve very gradually. Gradual CMEs undergo weak acceleration that is usually much longer-lasting than that experienced by impulsive CMEs. Most CMEs, however, are neither very impulsive nor very gradual, but something in between (Zhang and Dere 2006).

The first phase, which is initiation, happens primarily in the inner corona (Zhang and Dere (2006) put the threshold between the inner and the outer corona at $2\,R_\odot$). It lasts for some tens of minutes and involves the process that causes the onset of the CME. Usually there is some large-scale structure that starts to rise slowly, at a speed that is on the order of tens of kilometers per second.

Following initiation, the CME undergoes its main acceleration. This phase is typically characterized by a period of fast increase in velocity, or at least the period during which most of the change in velocity takes places, be that impulsively or gradually. The main acceleration also takes place in the inner corona, and lasts for anything from a few minutes to a few hours, though the usual duration is some tens of minutes. The magnitude of the acceleration experienced by the CME during this phase is also widely distributed. The acceleration of some gradual events may be very low, even under $10\,\mathrm{m\,s^{-2}}$, while the acceleration of the most impulsive ejections can exceed $1000\,\mathrm{m\,s^{-2}}$. Typically the acceleration is somewhere around a few hundred $\mathrm{m\,s^{-2}}$, e.g., the average acceleration found by Zhang and Dere (2006) was $330.9\,\mathrm{m\,s^{-2}}$. Zhang et al. (2001) found that if the CME is associated with a flare, the main acceleration phase of the CME coincides well with the rise phase of the flare, and the peak velocity is achieved around the same time as the soft X-ray flux of flare reaches its maximum.

During the final propagation phase the CME continues its movement into the outer corona and from there into the heliosphere. There may be some residual acceleration that is small compared to the acceleration of the main acceleration phase, but mostly the CME velocity remains relatively constant during this phase. The angular width and position angle also remain the same during this phase, so that when the CME reaches this phase, it can be considered to be more or less fully developed (Zhang and Dere 2006).

2.4 Shocks driven by CMEs

A *shock wave* (see, e.g., Boyd and Sanderson 2003; Koskinen 2011; Parks 2004), or just *shock*, is a boundary in plasma that forms when a disturbance moves through the plasma at a speed greater than the local magnetosonic speed,

$$v_{\mathrm{ms}} = \sqrt{v_{\mathrm{A}}^2 + v_{\mathrm{s}}^2}, \tag{2.1}$$

where $v_{\mathrm{A}} = \sqrt{B^2/(\mu_0 \rho_{\mathrm{m}})}$ is the Alfvén speed[3] and $v_{\mathrm{s}} = \sqrt{\gamma kT/m}$ is the speed of sound, i.e., the speed of a longitudinal compression wave. In the expressions for the two speeds B is the magnetic field magnitude, μ_0 is the vacuum permeability, ρ_{m} is the mass density of the plasma, γ is the adiabatic index (the ratio of the heat capacity at constant pressure to the heat capacity at constant volume), k is the Boltzmann constant, T is the plasma temperature, and m is the average mass of a plasma particle.

Alfvén speed is the speed of *Alfvén waves*, which are transverse, low-frequency magnetohydrodynamic (MHD) waves propagating in plasma. Alfvén waves are transverse oscillations of the magnetic field lines (similar to the oscillations of a guitar string), which cause plasma particles to also oscillate transverse to the magnetic field (Krall and Trivelpiece 1973). The waves themselves propagate parallel to the magnetic field lines. Together the Alfvén speed v_{A} and the speed of sound v_{s} are the two characteristic speeds of MHD (Koskinen 2011).

The interface of the shock is called the *shock front*, and it divides the plasma into two regions, the *upstream* and *downstream* regions. The plasma that has not yet encountered the shock is upstream of the shock, while the plasma through which the shock has already passed is downstream of the shock. As the upstream plasma encounters the shock front, it undergoes changes in its properties like density and pressure. The changes may be approximated to be happening discontinuously. Due to this discontinuity it is not possible to describe the plasma conditions in the shock itself. Instead, the plasma upstream and downstream of the shock and how the two are related can be described using the *Rankine–Hugoniot relations*,[4] also known as the *shock-jump conditions*. These relations describe the conservation of mass, momentum, energy and magnetic flux across the shock. The relations will not be listed here, but they can be found for example in any of the plasma physics textbooks mentioned at the beginning of this section.

Most space plasmas are collisionless (Kivelson and Russell 1995). This means that the mean free path of the particles (i.e., the average distance a particle travels before colliding with another particle) is much larger than the spatial scale of the

[3] Named after the Swedish physicist Hannes Alfvén (1908–1995), who was awarded the Nobel Prize in Physics in 1970 for his foundational work on the theory of magnetohydrodynamics (MHD).

[4] Originally the Rankine–Hugoniot conditions referred to the jump conditions across a hydrodynamic shock, but in plasma physics the term is widely used to refer to the jump conditions in magnetohydrodynamic shocks.

interactions being studied. In the case of shocks this means that the shock is much thinner than the mean free path of the plasma particles. The shocks driven by CMEs are essentially collisionless.

Strictly speaking the Rankine–Hugoniot relations apply to MHD shocks, in which the collisions between plasma particles are responsible for the changes that take place in the shock. In collisionless plasmas, however, collisions cannot be responsible for anything that happens in the shocks. In general, the theory of MHD cannot fully explain the behavior of collisionless plasmas. For example, in MHD the plasma is assumed to be one fluid that has one temperature, but in a collisionless plasma the ions and electrons that make up the plasma do not interact via collisions and therefore can have different temperatures. Still, MHD does work "remarkably well in collisionless tenuous space plasmas" (Koskinen 2011), and tools from MHD can be used to describe the behavior of collisionless shocks.

In ideal MHD, in which plasma is assumed to be perfectly conductive, there are three fundamental wave modes, *slow*, *intermediate*, and *fast* modes. The intermediate wave mode is also known as the *shear Alfvén wave mode*. All three wave modes have characteristic velocities, which are given by

$$v_{\mathrm{fm/sm}}^2 = \frac{1}{2}\left[(v_\mathrm{s}^2 + v_\mathrm{A}^2) \pm \sqrt{(v_\mathrm{s}^2 + v_\mathrm{A}^2)^2 - 4v_\mathrm{s}^2 v_\mathrm{A}^2 \cos^2\theta}\right], \tag{2.2}$$

$$v_\mathrm{i}^2 = v_\mathrm{A}^2 \cos^2\theta, \tag{2.3}$$

where the plus and minus signs give the fast-mode speed v_fm and the slow-mode speed v_sm, respectively, and v_i is the intermediate-mode speed. In the expressions v_A is the Alfvén speed, v_s is the speed of sound, and θ is the angle between the magnetic field $\boldsymbol{B}$ and the wave vector $\boldsymbol{k}$ of the propagating plasma wave.

Corresponding to the fast- and slow-mode MHD waves, shocks can be divided into fast and slow shocks. There is no shock corresponding to the shear Alfvén mode, since that mode is purely transverse, meaning that shear Alfvén waves are not compressive and cannot form shocks. However, the fast- and slow-mode waves are compressive, which means that they change the properties of the plasma they propagate in, and in a supersonic flow they can form shocks (Parks 2004).

In a fast shock the magnetic field strength increases across the shock front, while in a slow shock it decreases. According to the Rankine–Hugoniot relations the normal component of the magnetic field (the component parallel to the shock normal) is continuous across the shock, so the increase or decrease is in the transverse component of the magnetic field. This means that moving across the shock front of a fast shock, the magnetic field lines bend away from the shock normal, while in a slow shock the field lines bend towards it. This is illustrated in Figure 2.4. Observations of shocks in space plasmas show that fast shocks are much more common than slow shocks (Kivelson and Russell 1995). The shocks driven by CMEs are fast shocks.

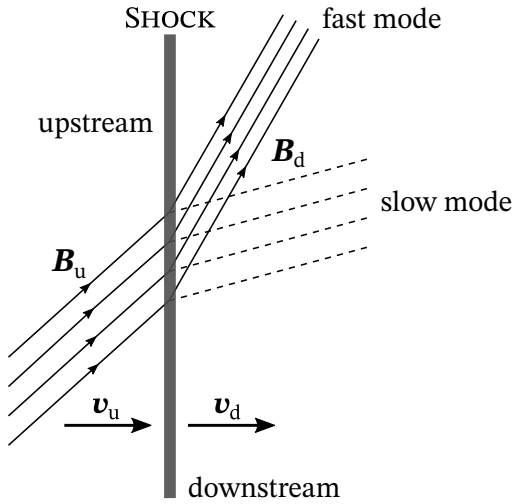

Figure 2.4 The effect of a fast or slow shock on the magnetic field lines. Moving across the shock front of a fast shock, magnetic field lines bend away from the shock normal. In the case of a slow shock the field lines bend towards the shock normal. The situation is shown in the rest frame of the shock, in which the upstream plasma approaches the shock with velocity $\boldsymbol{v}_\mathrm{u}$, and the downstream plasma recedes from the shock with velocity $\boldsymbol{v}_\mathrm{d}$. Adapted from Kivelson and Russell (1995).

Another property by which shocks can be classified is the angle θ_Bn between the shock normal $\hat{\boldsymbol{n}}$ and the upstream magnetic field $\boldsymbol{B}_\mathrm{u}$. The angle θ_Bn is an important parameter in collisional shocks, because the orientation of the shock relative to the upstream magnetic field affects the particle acceleration that occurs at the shock front. If $\theta_\mathrm{Bn} = 0°$, the shock is said to be a *parallel* shock, if $0° < \theta_\mathrm{Bn} < 90°$, the shock is an *oblique* shock, and if $\theta_\mathrm{Bn} = 90°$, it is a *perpendicular* shock. Oblique shocks can further be divided into *quasi-parallel* shocks if $0° < \theta_\mathrm{Bn} < 45°$, and *quasi-perpendicular* shocks if $45° < \theta_\mathrm{Bn} < 90°$ (Parks 2004).

Collisionless shocks driven by CMEs are powerful accelerators of charged particles, and as such they are sources of electromagnetic radiation, especially at radio wavelengths. Acceleration of electrons by coronal or interplanetary shocks is the accepted emission mechanism of type II radio bursts (Bougeret and Pick 2007; see Section 3.3.1). The mechanism thought to be responsible for these radio bursts is *shock drift acceleration*, a process in which electrons drift along the shock front and reflect back upstream or are transmitted downstream. The electrons emit electromagnetic radiation as a result of the acceleration they undergo.

2.5 Shock drift acceleration

When a charged particle such as an electron encounters a shock, the interaction between the shock front and the particle can cause the particle to be accelerated, which in turn causes it to emit electromagnetic radiation. The particle can interact once or many times with the shock, and in general multiple interactions lead to more acceleration than a single one (Aschwanden 2006). There are two main mechanisms that cause particle acceleration at shock fronts, *shock drift acceleration*, and *diffusive shock acceleration* (Koskinen 2011). In shock drift acceleration an electron (or an ion, but solar radio emission is caused almost exclusively by the acceleration of electrons so they will by used when describing the process) interacts once with the shock, drifting along it and being accelerated in the process. In diffusive shock acceleration the electron interacts with magnetic irregularities in the plasma flow in such a way that it crosses the shock front multiple times and is thus accelerated by the shock. Shock drift acceleration will be discussed here.

Consider a fast quasi-perpendicular shock that moves through plasma and magnetic field at velocity $\boldsymbol{v}_{\mathrm{sh}}$. In the rest frame of the shock the upstream plasma moves towards the shock at velocity $\boldsymbol{v}_{\mathrm{u}} = -\boldsymbol{v}_{\mathrm{sh}}$, and after crossing the shock front, the plasma continues moving downstream at some velocity $\boldsymbol{v}_{\mathrm{d}}$ (in general $\boldsymbol{v}_{\mathrm{u}} \nparallel \boldsymbol{v}_{\mathrm{d}}$). Let $\boldsymbol{B}_{\mathrm{u}}$ and $\boldsymbol{B}_{\mathrm{d}}$ denote the upstream and downstream magnetic fields, respectively. Since we assumed that the shock is fast, the downstream magnetic field is stronger than the upstream field, $\boldsymbol{B}_{\mathrm{d}} > \boldsymbol{B}_{\mathrm{u}}$. In the rest frame of the shock the motion of the plasma in the magnetic field induces an electric field $\boldsymbol{E} = -\boldsymbol{v}_{\mathrm{u}} \times \boldsymbol{B}_{\mathrm{u}}$, which is parallel to the shock front (Pesses et al. 1982).

Now, consider an electron moving along the upstream plasma towards the shock front. Moving in a magnetic field the electron gyrates, i.e., performs circular motion, perpendicular to the field lines. The characteristic frequency and radius of the circular motion are

$$\omega_{\mathrm{c}} = \frac{eB}{m_{\mathrm{e}}}, \quad r_{\mathrm{c}} = \frac{v_{\perp}}{\omega_{\mathrm{c}}} = \frac{m_{\mathrm{e}} v_{\perp}}{eB},$$

where e is the elementary charge, B is the magnetic field strength, m_{e} is the mass of the electron, and $v_{\perp}$ is the magnitude of the velocity perpendicular to B. These quantities are known as the *gyrofrequency* and *gyroradius* (or Larmor frequency and Larmor radius), respectively. We notice that in this situation the motion of the electron consists of the superposition of two different motions, the circular Larmor motion and the overall drift of the electron towards the shock front. The drift, which in general happens much more slowly than the circular motion, can be approximated as the motion of the center around which the electron gyrates. This central point is known as the *guiding center*. In the rest frame of the shock the motion of the electron is caused by the so-called $\boldsymbol{E} \times \boldsymbol{B}$ *drift* (Sarris and Van Allen 1974; for a description of $\boldsymbol{E} \times \boldsymbol{B}$ drift see, e.g., Boyd and Sanderson 2003), in which an electric field perpendic-

ular to a magnetic field causes the guiding center of a gyrating charged particle to drift in a direction perpendicular to both fields.

In general, the electron's gyroradius is much smaller than the shock thickness, so that when the electron hits the shock front, it experiences a continuous change in magnetic field. The scale L of this change however is assumed to be much larger than the electron gyroradius, $r_c \ll L$, which means that the change in magnetic field that the electron feels is continuous but small. In this case the magnetic moment of the electron,

$$\mu_B = \frac{W_\perp}{B} = \frac{m v_\perp^2}{2B}, \tag{2.4}$$

where $W_\perp$ is the kinetic energy of the perpendicular component of the electron's motion, is also constant (Pesses 1981). The magnetic moment μ_B is also known as the *first adiabatic invariant*.[5]

When the electron interacts with the shock, it experiences another drift, called *gradient drift* (see, e.g., Boyd and Sanderson 2003), in which the guiding center of the electron drifts due to the change in the strength of the magnetic field. The velocity caused by the gradient drift is given by

$$\boldsymbol{v}_{\nabla B} = \frac{\mu_B}{eB^2} \boldsymbol{B} \times (\nabla B). \tag{2.5}$$

From this we see that the direction of the drift is perpendicular to both the magnetic field and the gradient of the magnetic field. For a quasi-perpendicular shock this implies that the drift is along the shock front. Thus, the drift is also anti-parallel to the electric field, and therefore the electron is accelerated.

Once the electron has drifted along the shock front, it can either be transmitted downstream or reflected back upstream. Though both transmitted and reflected electrons gain energy, the gain is much larger when the electrons are reflected back upstream (Ball and Melrose 2001). From (2.4) we see that the conservation of magnetic moment requires that for transmitted electrons the energy gain is in the perpendicular component of motion, since $B_d > B_u$, so that $v_{\perp,d} > v_{\perp,u}$ in order for $\mu_{B,d} = \mu_{B,u}$ to be satisfied. Similarly, since reflected electrons re-enter the upstream region where the magnetic field remains the same, the conservation of magnetic moment requires that for reflected electrons the energy gain is in the parallel component of motion (Holman and Pesses 1983).

In order for type II radio bursts to be produced via shock drift acceleration of electrons, the shock must be close to perpendicular, with $\theta_{Bn} > 80°$ (Mann 1994).

[5] In plasma physics adiabatic invariants are approximate constants of motion which are associated with the periodic motion of charged particles in magnetic fields (see, e.g., Boyd and Sanderson 2003; Koskinen 2011). This means that adiabatic invariants, like magnetic moment, remain constant if the parameters describing the motion change slowly. Again, using the first adiabatic invariant, magnetic moment, as an example, it remains constant if the particle moves in a magnetic field whose temporal or spatial change happens slowly compared to the Larmor frequency or radius of the particle.

This is because the electron distributions that can produce the type II emission are formed upstream of the shock, meaning that they consist of electrons reflected from the shock front. Reflection is most efficient for nearly perpendicular shocks. However, when $\theta_{\mathrm{Bn}} \to 90°$ electrons are not reflected by the shock and thus no type II emission is produced. According to Holman and Pesses (1983) a 1000 km s^{-1} shock produces type II radio bursts if $80° \lesssim \theta_{\mathrm{Bn}} \lesssim 87°$. For a faster 2000 km s^{-1} shock the interval is even smaller, with type IIs occurring only if $80° \lesssim \theta_{\mathrm{Bn}} \lesssim 83°$. An earlier study by Sarris and Van Allen (1974) found that the same holds for protons accelerated at quasi-perpendicular shocks, namely that energy gain is greatest when $\theta_{\mathrm{Bn}} > 80°$, though they also noted that reflection of particles falls off when $\theta_{\mathrm{Bn}} \to 90°$.

Thus, it can be concluded that type II radio bursts are produced only within a relatively narrow range of angles between the shock normal and the magnetic field. This implies that only some parts of the shock, with a favorable geometry between the shock front and the upstream magnetic field, can be expected to produce type II radio bursts. This mean that the production can be highly localized so that it only occurs on some regions of the shock.

3 Radio emission associated with CMEs

Radio waves cover the electromagnetic spectrum from as low as 30 Hz all the way up to 300 GHz and as such they form the largest section of it. The Sun produces radio emission at frequencies that range from a few kHz to a few hundred GHz, or the top end of the radio frequency spectrum (Bougeret and Pick 2007). CMEs involve the acceleration of charged particles to high energies. Therefore they too emit radio waves on a wide band of frequencies, the range running from tens of kHz all the way to hundreds of MHz.

Much of the radio emission from CMEs comes in the form of *solar radio bursts*. In the 1960s solar radio bursts at frequencies below about 300 MHz were classified into five different types (Wild et al. 1963), named type I–V radio bursts. These bursts are emitted through many different mechanisms. This chapter will summarize first the different ways solar radio emission can be classified based on emission mechanism, then the emission mechanisms themselves, and finally the types of radio bursts relevant to CMEs.

3.1 Classifying solar radio emission

There are two broad ways of classifying radio emission from the Sun and elsewhere in the cosmos. These are *coherent* vs. *incoherent* (see, e.g., Melrose 2017; Nindos 2020), and *thermal* vs. *non-thermal* (see, e.g., Condon and Ransom 2016) radio emission. The first classification relates to the emission mechanism, such that a particular mechanism can be coherent or incoherent. The second one relates to the source of the emission, which virtually always means electrons (Wilson et al. 2009). An electron distribution can be thermal or non-thermal, and these distributions emit radio waves via different mechanisms, so there is overlap to these classifications.

3.1.1 Coherent and incoherent emission

Incoherent radio emission emerges when each electron in a radio source emits photons randomly and independently from the other electrons in the distribution (Gary and Hurford 2004). Since the electrons radiate photons independently, the number of emitted photons is proportional to the number of emitting electrons (Nindos 2020), and this implies that the total emission from the distribution is simply the sum of the emissions from the individual electrons (Melrose 2017).

In turn, coherent radio emission comes about when the electrons in the radio source "come together", e.g., when instabilities in the plasma induce collective motions of electrons, causing them to accelerate and emit photons in phase with each other (Nindos et al. 2008). In general, coherent emission mechanisms are capable of converting the kinetic energy of electrons into electromagnetic radiation more efficiently than incoherent emission mechanisms (Benz 2004). This is because in coherent mechanisms the emitting electrons act together as a larger emitting entity, whereas incoherent emission is emitted by a collection of individual electrons.

Both incoherent and coherent emission are encountered on the Sun. Of the emission mechanisms via which electrons in the solar atmosphere emit at radio frequencies, bremsstrahlung or free–free and gyromagnetic emission mechanisms are incoherent, while plasma emission is an example of a coherent mechanisms (Bastian 2004). For descriptions of these emission mechanisms see Section 3.2.

3.1.2 Thermal and non-thermal emission

Whether radio emission is classified as thermal or non-thermal depends on the energy or velocity distribution the emitting electrons have. Thermal emission is produced by a source whose electrons follow a Maxwell–Boltzmann velocity distribution. A thermal source is also said to be in local thermodynamic equilibrium (LTE), which means that the material is in thermal equilibrium with itself, so that there is negligible change in temperature within the mean free path of the emitting electrons and emitted photons (Condon and Ransom 2016; Nindos 2020).

The radiation from a thermal source is emitted via the thermal motion of particles and as such is essentially a random process. There is thus a limit to the possible brightness temperature T_B (see Section 4.1.2) of the radiation, set by the electron temperature T_e (Gelfreikh 2004),

$$T_\mathrm{B} \leq T_\mathrm{e}.$$

Non-thermal radio emission originates from electrons that are not in LTE and their velocities do not follow a Maxwell–Boltzmann distribution. Rather the electrons in non-thermal sources have a power-law energy distribution (Condon and Ransom 2016). Most radio emission in radio astronomy is emitted by non-thermal electrons via different mechanisms (Wilson et al. 2009). Whereas the brightness tem-

perature, i.e., the intensity, of thermal radiation is limited by the thermodynamic temperature of the emitting electrons, in non-thermal sources this is not so. The intensity of non-thermal emission (measured in kelvins as brightness temperature) may be significantly greater than the thermodynamic temperature of the source. In many cases non-thermal sources do not even have well defined temperatures (Condon and Ransom 2016).

All thermal radio emission is incoherent, while non-thermal emission can be incoherent or coherent. The Sun is a source of both thermal and non-thermal radio emission. Thermal emission dominates the radio emission from the quiet Sun, while non-thermal radiation is principally emitted during flares and CMEs, though both are sources of thermal emission too (Nindos 2020).

3.2 Emission mechanisms

The previous section described the division of astronomical and solar radio emission into coherent or incoherent and thermal or non-thermal emission. This section will discuss three emission mechanisms relevant to CMEs, free–free, gyrosynchrotron, and plasma emission. The focus will be on plasma emission, since it is the main source of radio emission associated with CMEs (Vourlidas 2004).

3.2.1 Free–free emission

When an electric charge q undergoes an acceleration a, it emits electromagnetic radiation with power P according to the Larmor formula (Condon and Ransom 2016)

$$P = \frac{q^2 a^2}{6\pi\epsilon_0 c^3}, \tag{3.1}$$

where ϵ_0 is the permittivity of free space and c is the speed of light. Free–free radiation is emitted when electrons pass by ions (mostly protons) in plasma, causing them to be deflected and thus accelerated (or decelerated, since for conservation of energy to be satisfied, the electron necessarily loses kinetic energy) by the Coulomb interaction between them and the ions. Free–free emission is named such because the electron is free before the interaction and it remains free after it. Because the electron loses energy in the interaction, free–free emission is also known as *bremsstrahlung*, which is German for “braking radiation” (Condon and Ransom 2016).

Free–free radiation is emitted by thermal electrons and it is the primary emission mechanism responsible for radio emission of the quiet Sun (Nindos 2020). CMEs, which cause coronal plasma trapped in a magnetic field to expand outward from the Sun, also produce free–free emission. If observed, the free–free emission has a structure similar to that of the CME seen in white-light coronagraph images, but

often this type of radio emission is hard to observe. This is because as it is coming from thermal electrons, free–free emission is often masked by the much brighter emission emanating from non-thermal sources (Vourlidas 2004).

3.2.2 Gyrosynchrotron emission

Gyrosynchrotron is one type of *magnetobremsstrahlung*, or "magnetic braking radiation". While free–free emission comes from the electric interaction between electrons and ions in plasma, gyrosynchrotron radiation is emitted by electrons being accelerated by a magnetic field. When an electron moves in a magnetic field, it experiences a force acting on it according to the magnetic part of the Lorentz law

$$\boldsymbol{F} = e\boldsymbol{v} \times \boldsymbol{B}, \tag{3.2}$$

where e is the charge of the electron, $\boldsymbol{v}$ its velocity, and $\boldsymbol{B}$ the magnetic flux density. A force causes an acceleration, and an accelerating electric charge emits electromagnetic radiation. The acceleration caused by the magnetic force does not affect the magnitude of the velocity of the electron, only the direction of its motion. The direction of the acceleration is such that it causes the electron to move along a spiral in the magnetic field.

In general, the radio emission by electrons moving in a magnetic field is termed *gyromagnetic emission* (Nindos 2020). Depending on the energy of the emitting electrons, there are three varieties of gyromagnetic emission. If the electrons are non-relativistic (the Lorentz factor $\gamma \approx 1$) the emission is called *gyroresonance* or *cyclotron* emission. Gyrosynchrotron emission comes from mildly relativistic electrons (for which $\gamma < 3$). If the electrons are ultra-relativistic ($\gamma \gg 1$), the emission is termed *synchrotron* emission (Dulk 1985).

Of these three forms of gyromagnetic emission, gyrosynchrotron can be associated with CMEs (Vourlidas 2004), though observations of it in conjunction with them are rare (Nindos 2020). On the Sun gyroresonance emission is primarily seen as microwaves coming from strong magnetic fields above sunspots. Synchrotron emission is very common in astronomical radio sources, for example the radio emission discovered by Jansky was synchrotron emission from non-thermal electrons gyrating in the magnetic field of the Milky Way galaxy (Burke et al. 2019). Gyroresonance radiation is emitted by thermal electrons, while gyrosynchrotron and synchrotron radiation can come from either thermal or non-thermal electrons. Gyrosynchrotron emission from CMEs tends to be non-thermal, and most of the astronomical sources of synchrotron radiation have power-law energy distributions, i.e., they are non-thermal sources.

3.2.3 Plasma emission

Plasma radiation is a coherent emission mechanism that plays an important role in the radio emission of the Sun especially at frequencies below 1 GHz. In and below the hundreds of MHz range most emission from solar radio bursts comes from plasma emission (Gary and Hurford 2004). As a coherent mechanism plasma emission can produce radiation of a far greater intensity than the incoherent mechanisms described above. Plasma radiation is emitted by non-thermal electrons.

The mechanism behind plasma emission is more complex than the mechanism behind free–free or gyrosynchrotron emission. Plasma emission occurs when an exciting agent causes the generation of *Langmuir waves* in plasma, from which energy then escapes as electromagnetic radiation. Langmuir waves, also known as *electron plasma waves*, are longitudinal waves of the electrons in the plasma itself (Aschwanden 2006). Plasma emission occurs primarily at the local plasma frequency ν_p and its second harmonic $2\nu_\mathrm{p}$. The local plasma density is defined by

$$\nu_\mathrm{p} = \frac{1}{2\pi}\sqrt{\frac{n_\mathrm{e}e^2}{m_\mathrm{e}\epsilon_0}} \approx 9\sqrt{n_\mathrm{e}}, \tag{3.3}$$

where n_e is the electron density in m^{-3}, e is the charge of an electron, m_e is its mass and ϵ_0 is again the permittivity of free space. This expression gives the plasma frequency in Hz. Since the plasma density decreases when moving further out from the Sun's surface, the local plasma frequency also decreases. Emission at higher harmonics is also possible, but very rare (Dulk 1985).

There are many possible versions of plasma emission processes and many possible mechanisms that are responsible for the intermediate steps in the overall process. The original theory of plasma emission was developed by Ginzburg and Zheleznyakov, who published it in 1958. Here we will provide a qualitative description of a variant of their original theory following Melrose (1991). This variant, shown schematically in Figure 3.1, consists of three stages.

In the first stage, an electron beam in the plasma generates an instability that drives the production of Langmuir waves in the plasma. One accepted instability that produces Langmuir waves is the so-called *bump-in-the-tail* or *two-stream* instability (e.g., Aschwanden 2006; Dulk 1985), where fast electrons outpacing slower ones and arriving at some location before them causes a transient bump to form at the higher end of the electron velocity distribution.

The second stage of the plasma emission process involves the production of transverse waves[6] at the fundamental plasma frequency. A number of ways for the energy to escape from the Langmuir waves as electromagnetic radiation have been proposed.

[6]The term used for electromagnetic radiation by Melrose (1991). The term is also used in other works on the subject.

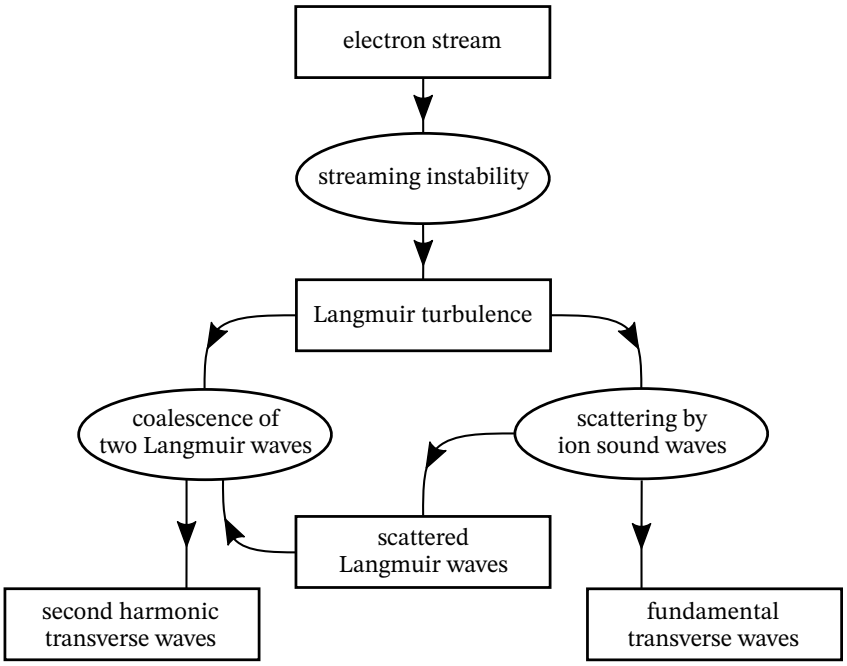

Figure 3.1 Schematic diagram of a variant of the theory of plasma emission originally put forward by Ginzburg and Zheleznyakov in 1958. In this version of the theory the Langmuir waves scatter from ion sound waves. In other versions some other non-linear process is responsible for the scattering. Diagram adapted from Melrose (1991).

Here the process of *three-wave interactions* will be described. As the name suggests, this involves the interaction of three waves, either the production of a third wave from the coalescence of two, or the production of two waves as a result of the decay of a single wave. There are three types of waves that can take part in these three-wave interactions: Langmuir waves (L), ion acoustic waves (S), and transverse waves (T). *Ion acoustic waves* or *ion sound waves* (see, e.g., Parks 2004) are low-frequency longitudinal oscillations of ions in plasma, similar to Langmuir waves, which are high-frequency electron oscillations. They are similar to ordinary sound waves, such as those propagating in air, though whereas the propagation of sound waves in a neutral fluid is driven by the collisions between particles, ion acoustic waves are driven mainly by the electrostatic interaction between the ions.

Looking first at the right-hand branch of the diagram in Figure 3.1, we see that Langmuir waves can scatter off ion acoustic waves to generate either radio emission at the fundamental plasma frequency or alternatively they can scatter into secondary Langmuir waves. These two processes can be written as $L + S \rightarrow T$ and $L + S \rightarrow L'$, respectively, where L' indicates once-scattered Langmuir waves. In addition to these coalescence processes there are two possible decay processes, $L \rightarrow S + T$ and $L \rightarrow S + L'$, that can occur.

Then on the left-hand branch of Figure 3.1 we have the production of radio emission at the second harmonic of the plasma frequency. This occurs via the process $L + L' \rightarrow T$, in which Langmuir waves and once-scattered Langmuir waves coalesce to produce the higher-frequency emission.

The version of the theory presented here does not take into account for example the effects of a magnetic field on the plasma emission process. Over the years modifications have been made to the theory to address this and other factors such as the polarization of plasma emission. Melrose (2017) provides a recent and comprehensive summary of many of these modifications, as well as references to more thorough treatments of them.

On the Sun plasma emission occurs in radio bursts, and contributions from it are not seen in the radio spectrum of the quiet Sun. This is not surprising, as plasma emission requires the acceleration of electrons in order to produce the Langmuir waves that are the source of the radio emission. As mentioned at the start of this section, plasma emission is the main source of radio emission associated with CMEs. Flares are also significant sources of plasma emission (see, e.g., Bastian et al. 1998). Plasma emission is the accepted emission mechanism of type II, III, and IV radio bursts, which are all associated with CMEs (Gopalswamy 2011; Vourlidas 2004; for descriptions see the following section).

3.3 CME-related radio bursts

Of the five different types of radio bursts mentioned at the start of the chapter, types II, III, and IV are associated with CMEs (Gopalswamy 2011). All of these three bursts are seen in the metric range, and all are produced by non-thermal distributions of electrons. Figure 3.2 shows the three types of radio bursts in a simplified representation of a dynamic spectrum. Types II and IV are discussed below in more detail, type III will only be briefly described here.

Type III radio bursts are characterized by a fast drift from high to low frequencies. The drift rate is higher for higher frequencies (White 2007). Often type III bursts occur in groups that can contain as many as 20 individual bursts, each lasting only for a few seconds (Dulk 1985). Type III radio bursts are produced by plasma emission, which is caused by electron beams that propagate outward from the Sun along open magnetic field lines (Bougeret and Pick 2007).

Figure 3.2 also includes a fourth type of radio burst, the type V radio burst. Type V bursts are associated with type III bursts, appearing in conjunction with around 10 % of them. They appear as extended wideband continuum phases following type III bursts (Wild et al. 1963).

3.3.1 Type II radio bursts

Type II radio bursts are characterized by a slow drift from higher to lower frequencies that lasts typically around 10 minutes (Wild and Smerd 1972). They mostly occur at frequencies below 150 MHz (Gopalswamy 2006) and drift to lower frequencies at a rate of around 0.25 to 1 MHz s^{-1} (Melrose 2017; Street et al. 1994). Type II radio bursts are usually either unpolarized or weakly polarized (Dulk 1985; Wild et al. 1963). They are caused by non-thermal electrons that are accelerated in the upstream regions of coronal or interplanetary shocks, such as those driven by CMEs (Bougeret and Pick 2007).

The emission from type II radio bursts is mostly observed in the fundamental and the harmonic of the local plasma frequency and thus the accepted emission mechanism of the radiation is plasma emission (Gopalswamy 2006; Vourlidas 2004). The plasma emission is thought to result from electrons which are reflected from the shock front via shock drift acceleration, which makes the upstream plasma unstable to the production of Langmuir waves (see Sections 2.5 and 3.2.3).

As with other radiation caused by plasma emission, the higher frequencies of the emission originate from lower in the solar corona, while lower frequency emission comes from higher up in the corona (Gopalswamy 2006). The drift in frequency is therefore interpreted as being caused by the outward motion of the source, i.e., the shock, and the emitting electrons through the corona. If the coronal density can be estimated, the drift rate of a type II radio burst can be used to calculate the speed of the shock that causes it (e.g., Magdalenić et al. 2010).

Emission at the second harmonic of the plasma frequency is seen in about 60 % of type II radio bursts (Street et al. 1994). Many times, both the fundamental and har-

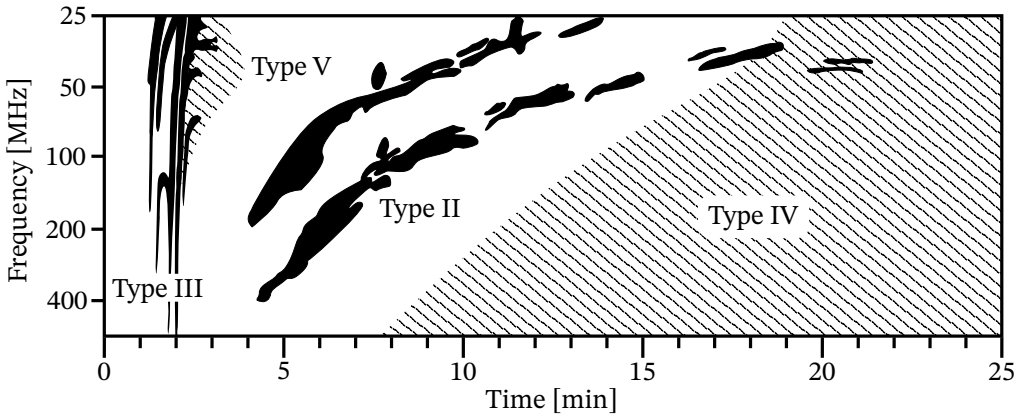

Figure 3.2 Idealized dynamic spectrum showing four of the five different types of solar radio bursts appearing in the metric to decametric wavelength range. Of these, types II, III, and IV are related to CMEs, with type V radio bursts rarely accompanying type III radio bursts. Adapted from Cliver (2001).

monic bands are split into two subbands in a phenomenon known as *band splitting*. The relative split in frequency typically ranges between 0.05 and 0.6 of the central frequency, though lower in the corona the split tends to be on the smaller end of the range, around 0.1 (Vršnak et al. 2001). One possible explanation for band splitting, put forward by Holman and Pesses (1983), is that the two bands originate from different regions in the shock front and that this separation results in the observed difference in their frequencies. Another possible explanation is that the two bands originate on the upstream and downstream regions of the shock (Smerd et al. 1974, 1975). Observations of type II band splitting can be used for example to estimate the coronal magnetic field (e.g., Mahrous et al. 2018).

In addition to the slow-drift component of the burst, a type II can have fast-drift lanes that emanate towards higher and lower frequencies from the slow-drift component. These fast-drift structures are known as *herringbones* (see, e.g., Aschwanden 2006; Mann and Klassen 2005), and an example of a type II with these bursts can be seen in Figure 3.3. In a type II that has these herringbones the slow-drift component is typically called the *backbone*. It has been estimated that herringbones are seen in about 20 % of type II radio bursts (Benz and Thejappa 1988). Whereas the backbone

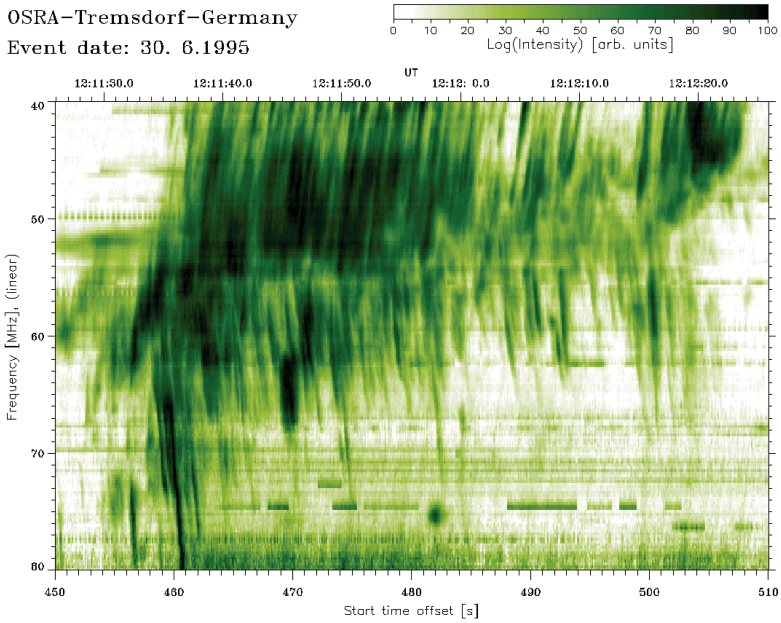

Figure 3.3 Dynamic spectrum showing a type II radio burst with the slowly drifting backbone (starting around 458 s at 62 MHz) and on both sides of it the fast-drift herringbones. The herringbones appear on either side of the backbone, the ones above drifting down in frequency, and the ones below drifting up in frequency. The herringbones are produced by electron beams being accelerated via shock drift acceleration at the shock front of a CME-driven shock. Adapted from Miteva and Mann (2007).

is at most weakly polarized, herringbones can be somewhat more strongly polarized (Cairns and Robinson 1987). The sense of polarization between the two components is always the same (Benz and Thejappa 1988).

Herringbones are similar in structure to type III radio bursts, though on average they have a drift rate about half that of type IIIs (Mann and Klassen 2002) and the range over which the frequency drifts in herringbones is much smaller than in type IIIs (Mann and Klassen 2005). Typically herringbones have a drift rate of around $10\,\mathrm{MHz\,s^{-1}}$. Herringbones, like type III radio bursts, are thought to originate from electron beams that travel along open magnetic field lines (Mann and Klassen 2005).

Herringbones are believed to be produced via shock drift acceleration along with the type II backbone (Holman and Pesses 1983). The electrons that produce herringbones are accelerated at the shock front along with those that produce the backbone, but escape in beams along open magnetic field lines. Herringbone production, just as the production of type II bursts in general, requires the shock to be nearly perpendicular (Mann and Klassen 2005). Holman and Pesses (1983) have also noted that just as a backbone may be seen without herringbones, herringbones may be observed without a backbone (see also, e.g., Morosan et al. 2019a). The presence of the backbone and herringbones depend on the geometry of the shock and the locations of the particle acceleration regions.

3.3.2 Type IV radio bursts

Type IV radio bursts are characterized by broadband continuum emission that mainly occurs in the tens of MHz to GHz range and typically lasts for tens of minutes. The original definition of type IV radio bursts referred to continuum emission from a source moving outward through the corona (Dulk 1985). Later on bursts with similar spectral characteristics whose sources did not appear to propagate in the corona were identified. They were also termed type IV bursts, which led to these two varieties being separated into *moving type IV* (IVm) and *stationary type IV* (IVs) radio bursts (Weiss 1963). Since the source of a type IVm propagates outward from the Sun, the burst shows a frequency drift in a dynamic spectrum, while a type IVs does not (Liu et al. 2018).

A number of different emission mechanisms have been proposed to be responsible for type IV radio bursts, among them synchrotron (Bastian et al. 2001), gyrosynchrotron (Bain et al. 2014; Carley et al. 2017), and plasma emission (Gary et al. 1985; Salas-Matamoros and Klein 2020; Vasanth et al. 2019). Morosan et al. (2019b) have also shown that the emission mechanism of a type IV radio burst can change over the lifetime of the burst. If the emission mechanism can be determined, type IV bursts can be used as diagnostic tools to probe the plasma conditions of the emitting region. Properties such as electron density or magnetic field can be estimated from observations of type IV bursts (Carley et al. 2020).

Most type IV bursts are associated with CMEs. A recent statistical study by Kumari et al. (2021) found that out of 446 type IV radio bursts that occurred over solar cycle 24, around 81 % were associated with a CME. The converse however is not true, i.e., most CMEs are not accompanied by type IV bursts. In their study, Kumari et al. (2021) found that only 2.2 % of CMEs were accompanied by type IV radio bursts. They also found that type IVs bursts are much more common than type IVm bursts, with only about 18 % of the type IV bursts being moving.

Type IV radio bursts are also associated with flares. In a statistical study of 685 radio events which included type II and type IV radio bursts, Cane and Reames (1988a) found that around 84 % of type IV bursts were associated with a flare. Most of the type IV-associated flares were intense, long-duration events. In an associated study on the same data set Cane and Reames (1988b) found that 88 % of the type IV bursts were preceded by a type II burst. Just as with CMEs, the converse was found not to be true: only about 30 % of type II bursts were followed by a type IV. Some type IV bursts that follow type II bursts may be caused by electrons transmitted to the downstream region of a shock, where they can interact with the enhanced magnetic field to produce gyrosynchrotron radiation (Holman and Pesses 1983).

4 | Theory

This chapter introduces some relevant concepts from the theory of radiative transfer, including specific intensity, flux density and brightness temperature. The units commonly used in radio astronomy to measure these quantities are also described. Finally, the concept of spectral index is introduced, describing what it is and how it can be used to probe the possible nature of observed radio emission.

4.1 Measuring radio emission

The radio data used in this thesis is recorded as *brightness temperature* (see, e.g., Condon and Ransom 2016; Rybicki and Lightman 2004; Wilson et al. 2009) which, though it is called a temperature and measured in kelvins, is not the same as physical temperature. Rather, brightness temperature is a measure of the specific intensity, or the brightness, of radiation. Let us now see where this convention of using temperature as a measure of brightness comes from.

4.1.1 Specific intensity and flux density

Starting with terminology, *brightness* or *intensity* refers to the power of radiation per unit area per unit solid angle. Some distinguish between these two, with brightness referring to the power emitted at the source, and intensity to the power along the path of the radiation to the detector. Assuming there is no emission or absorption happening along the way (such is the case in empty space), the two powers are the same, and here the two are used to refer to the same thing. Brightness is independent of distance, meaning in other words that the brightness measured at the source and at the detector are equal. As an example, this means that the Sun has the same brightness regardless of whether it is viewed from the Earth or from Venus.

Whereas brightness refers to the total power contributed by all frequencies, *specific intensity* or *spectral brightness*, denoted by I_ν is the intensity of radiation per unit

frequency. The units of I_ν are $\mathrm{W\,m^{-2}\,Hz^{-1}\,sr^{-1}}$.[7] As solar observations are usually conducted in narrow passbands, this quantity is more useful to consider than the total brightness across the entire spectrum.

Measuring specific intensity is usually possible for solar radio sources, since most of the time the source is larger than the beam of the observing telescope (the beam is the area from which the radiation arrives at the antenna). This, however, is not so for most astrophysical radio sources. They are unresolved in the sense that the source itself is smaller than the beam of the receiving telescope and thus the angular information is lost. In cases such as this what can be measured is the *flux density*, denoted by S_ν, which is the spectral power received by a detector per unit projected area. The units of S_ν are $\mathrm{W\,m^{-2}\,Hz^{-1}}$ (Burke et al. 2019). The flux densities of astronomical and solar radio sources are very small, so astronomers mostly use the unit *jansky*,[8] defined as

$$1\,\mathrm{Jy} = 10^{-26}\,\mathrm{W\,m^{-2}\,Hz^{-1}},$$

when measuring flux densities. In addition to this, in solar radio physics the unit *solar flux unit* (Bougeret and Pick 2007), defined as

$$1\,\mathrm{sfu} = 10^{-22}\,\mathrm{W\,m^{-2}\,Hz^{-1}} = 10^{4}\,\mathrm{Jy},$$

is used for measuring flux densities.

Flux density can be defined using specific intensity. The flux density of a source of radiation is given by the integral of the specific intensity of the source over the solid angle Ω_s subtended by it, i.e.,

$$S_\nu = \int_{\Omega_\mathrm{s}} I_\nu(\theta,\phi)\cos\theta\,\mathrm{d}\Omega, \tag{4.1}$$

where $\mathrm{d}\Omega$ is a solid angle element and θ is the angle between the line of sight and a normal to the surface of the detector. Assuming that the source's specific intensity is constant over Ω_s, and that $\theta \ll 1$ (meaning that the detector is directed at the source and the source is small so that θ remains small over the extent of the source), i.e., $\cos\theta \approx 1$, then (4.1) simply gives

$$S_\nu = I_\nu \Omega_\mathrm{s}. \tag{4.2}$$

As we will shortly see, flux density is useful when studying the spectral properties of solar radio bursts. Using the relationship given above between specific intensity

[7] In radio astronomy frequency is used more than wavelength, but naturally specific intensity can also be defined as the intensity of radiation per unit wavelength. In this case it is denoted by I_λ and has the units $\mathrm{W\,m^{-2}\,m^{-1}\,sr^{-1}} = \mathrm{W\,m^{-3}\,sr^{-1}}$.

[8] In honor of the American physicist Karl G. Jansky (1905–1950), who is widely considered to be the father of radio astronomy due to his 1931 discovery of radio emission coming from the Milky Way galaxy (Burke et al. 2019).

and flux density we can estimate the flux density of an extended radio burst from the recorded brightness data.

4.1.2 Brightness temperature

A *black body* is an idealized absorber and emitter of electromagnetic radiation. It absorbs all electromagnetic radiation incident on it, reflecting nothing. In addition to this, a black body in thermal equilibrium with its surroundings will necessarily (in order to remain in thermal equilibrium) emit electromagnetic radiation, termed *black-body radiation*. The radiation emitted by a black body is isotropic, meaning that the black body radiates equally in all directions. The spectral distribution of black-body radiation at a given temperature T is given by *Planck's law*,

$$B_\nu(T) = \frac{2h\nu^3}{c^2}\frac{1}{\mathrm{e}^{h\nu/(kT)} - 1}, \tag{4.3}$$

where B_ν is the specific intensity of the black-body radiation, ν is the frequency of the radiation, c is the speed of light, h is the Planck constant, and k is the Boltzmann constant.

In the limit of low frequencies, where $h\nu \ll kT$, the exponential in the denominator of (4.3) can be approximated as

$$\mathrm{e}^{h\nu/(kT)} = 1 + \frac{h\nu}{kT} + \cdots \approx 1 + \frac{h\nu}{kT}.$$

Then, using this in (4.3) we get

$$B_\nu(T) \approx \frac{2h\nu^3}{c^2}\frac{kT}{h\nu} = \frac{2k\nu^2}{c^2}T. \tag{4.4}$$

This is known as the *Rayleigh–Jeans law*, and it gives the specific intensity of black-body radiation at low frequencies. We see that B_ν given by (4.4) diverges for high frequencies. The Rayleigh–Jeans law was first derived in the beginning of the 20th century by the British physicists Lord Rayleigh and James Jean using assumptions from classical physics (see, e.g., Beiser 2003). The breakdown between the predictions of classical physics and experimental results became known as the *ultraviolet catastrophe*. The problems caused by this breakdown were solved by the German physicist Max Planck, who in 1900 discovered the law which now bears his name, and is described mathematically by equation (4.3).

We see from equation (4.4) that at low frequencies, a condition that certainly holds for observations conducted in radio astronomy, the specific intensity of the radiation that is emitted by a black body is directly proportional to its temperature. Thus we can define the brightness temperature T_B as the temperature a black-body

radiator would need to have in order to produce radiation of the same specific intensity as the observed source. From (4.4) we can write specific intensity in terms of brightness temperature as

$$I_\nu = \frac{2k\nu^2}{c^2} T_\mathrm{B}. \tag{4.5}$$

Putting this together with (4.2) we see that flux density and brightness temperature are related to each other by

$$S_\nu = \frac{2k\nu^2\Omega_\mathrm{s}}{c^2} T_\mathrm{B}. \tag{4.6}$$

This expresses flux density in terms of the frequency of the radiation. Equivalently, flux density can be written in terms of the wavelength of the radiation, so that

$$S_\lambda = \frac{2k\Omega_\mathrm{s}}{\lambda^2} T_\mathrm{B}. \tag{4.7}$$

4.2 Spectral index

Just as with black-body radiation, the intensity of radio emission radiated by a typical solar (or astrophysical) radio source is not constant across the frequency spectrum of the radiation. The relationship between intensity and frequency is described by the *spectral index* α (see, e.g., Burke et al. 2019; Condon and Ransom 2016), though usually the relationship is between the flux density and frequency, but as we see from above flux density is just the total intensity integrated over the source, so their frequency-dependence is the same.

The spectral index is usually defined by the expression

$$S_\nu(\nu) \propto \nu^\alpha, \tag{4.8}$$

which shows that the flux density of the radio source follows a power law in frequency. Another equivalent way of defining the spectral index is by defining it as the slope of the flux spectrum in a log–log plot, namely

$$\alpha = \frac{\mathrm{d}\log S_\nu}{\mathrm{d}\log \nu}, \tag{4.9}$$

where log is the base-10 logarithm. Looking at both of these definitions, we see that if $\alpha > 0$, the flux density of the source increases with frequency, and if $\alpha < 0$, the flux density decreases with frequency.

It should be noted that in many astrophysics and space physics textbooks and articles, especially older ones, the spectral index is defined with the opposite sign convention so that $S_\nu(\nu) \propto \nu^{-\alpha}$ (e.g., Rybicki and Lightman 2004 and the first edition of Burke et al. 2019 use this convention). The reason for this choice was that many

sources that were discovered in the early days of radio astronomy radiated more intensely at low frequencies than at high frequencies (Condon and Ransom 2016), and therefore it made sense to include the minus sign in the definition.

Different emission mechanisms have different shapes to their spectra, and thus their spectral indices may differ significantly. In general, optically thick (opaque) emission is characterized by flux increasing with frequency, which implies a positive spectral index, while the flux of optically thin (transparent) emission falls off with increasing frequency (Nindos 2020).

At low frequencies thermal emission, for example, has a spectral index of $\alpha \approx 2$. This is because at low frequencies thermal sources mostly radiate according to the Rayleigh–Jeans law, and as we see from (4.6), in the Rayleigh–Jeans regime $S_\nu \propto \nu^2$. For example, the radio emission of the quiet Sun is largely thermal in origin. At some higher frequency, $\nu \gg 1\,\mathrm{GHz}$, the emission becomes optically thin and the spectral index flattens to $\alpha \approx -0.1$ (Condon and Ransom 2016).

In contrast many astrophysical radio sources such as radio galaxies have synchrotron spectra at low frequencies, which are characterized by a relatively steep fall in flux with frequency, meaning that for synchrotron emission $\alpha < 0$. In general, a negative spectral index indicates that the emission is non-thermal in origin (Bastian et al. 2001), though similar to the spectrum of thermal emission, the spectrum of gyrosynchrotron emission can be divided into optically thick and optically thin parts (Nindos 2020). The emission is optically thick at low frequencies, meaning the spectral index is positive, and becomes optically thin at some higher frequency, at which point the spectral index turns negative. For solar radio bursts the turnover frequency, i.e., the frequency for which the emission turns from optically thick to optically thin, is $\nu \gtrsim 1\,\mathrm{GHz}$ (Carley et al. 2017; Nita et al. 2004). Therefore a negative spectral index in the hundreds of MHz range indicates that the radiation is due to plasma emission.

5 | Methods

In this thesis the radio emission associated with a CME is studied in detail. The investigation employs not only radio data but white-light and EUV images as well. In this chapter the sources of data and the methods of analysis are explained in detail. The CME that the radio bursts accompanied is also described. The description of the CME event largely summarizes the findings of previous studies of the ejection.

5.1 Data sources

Here the sources of data used in the thesis work are described in some detail. This being a work of solar radiophysics, the main source of data is the Nançay Radioheliograph. Using only radio data is not enough however, but they need to be compared with data from other sources. Here imaging from white-light coronagraph and EUV instruments is used to support the analysis of the radio data. The white-light and EUV data sources are also described.

5.1.1 Nançay Radioheliograph (NRH)

The *Nançay Radioheliograph* (NRH; Kerdraon and Delouis 1997), part of the Nançay Radio Observatory located in central France, is a T-shaped interferometer array dedicated to observing the Sun at a number of radio wavelengths.

The Nançay Radio Observatory was established in 1953, and the predecessor to NRH started operating there in June 1956 (Pick et al. 2011). The original interferometer consisted of eight 5 m dishes spaced at 50 m intervals. Over the decades the original system has been developed into the radioheliograph that is still in used today. The current version of NRH consists of two perpendicular antenna arrays, one oriented along an east–west direction, the other one north–south. Together the arrays contain 43 antennas. In addition to these NRH has four antennas outside the array to improve image quality, bringing the total number of antennas to 47 (https://www.obs-nancay.fr/radioheliographe). The antennas are motor-

ized so that they can follow the Sun as it moves in the sky during the daily 7.5 hour observation period. Depending on observation frequency and direction, the spatial resolution of NRH is between 0.3 and 6 arcmin.

The east–west array contains 19 of the 47 antennas. Four of the antennas have parabolic collectors, while the other 15 antennas have no dishes and instead consist only of thick dipole antennas. Of the antennas with parabolic collectors, two have 10 m dishes, one has a 7 m dish and one a 5 m dish. This last antenna is situated at the crossing point of the east–west and the north–south arrays and is shared among them. The main part of the array, that is the 15 dipole antennas and the central dish, are spaced at 100 m intervals. Then the 7 m dish is 50 m from the most easterly dipole, and the 10 m dish is another 50 m east. The other 10 m dish is 1600 m east, meaning that the possible baselines of the east–west array range from 50 m to 3200 m.

The north–south array, which was added in 1980 (The Radioheliograph Group 1983), contains 25 antennas, including the one shared with the east–west array. The first 24 antennas have 5 m parabolic collectors and are spaced at 54.3 m intervals, meaning that the main part of the north–south array has a maximum baseline of 1248 m. The 25th antenna, which was added later, has a 7 m parabolic collector and is located 1200 m south of the main array. Thus the entire north–south array has a maximum baseline of about 2448 m.

Currently NRH can perform measurements at up to 10 frequencies ranging from 150 MHz to 450 MHz, with an observing bandwidth of 700 kHz. Observations at different frequencies are not done simultaneously. Instead, during standard operations each frequency is observed for 5 ms, after which the next frequency is chosen during a 100 µs switch period. The observed frequencies can be chosen in 100 kHz steps.

The feed system of the multifrequency antennas consists of thick folded dipoles. Each dipole has a bandwidth of about one octave, which means that two such dipoles are needed to cover the full band of frequencies from 150 MHz to 450 MHz. The two dipoles in each feed cover the ranges 150 – 260 MHz and 260 – 450 MHz. The antennas of the north–south array and the four antennas of the east–west array that have dishes are equipped with two orthogonal pairs of dipoles, while the rest of the east–west antennas have only one such pair. The orthogonal pairs are needed to measure circular polarization. To illustrate this, consider the east–west array. If we denote the orthogonal dipole pairs of the dish antennas as (X, Y) and the single dipole pair of the other antennas as (x), then performing the correlations X, x and Y, x give us the Stokes I and Stokes V parameters, i.e., total intensity and circular polarization, respectively. The dipoles are oriented in such a way that X is parallel to, and Y is perpendicular to x.

For the first 20 years of operations, NRH only provided one-dimensional images of the Sun's radio emission. Limited two-dimensional imaging was possible (Alissandrakis et al. 1985) by using Earth-rotation aperture synthesis, which means using the Earth's rotation to improve the uv-coverage of the interferometer array. But while

two-dimensional maps of the Sun could be produced this way, it required a full day's observations to be able to compute such maps (The Radioheliograph Group 1993). Fast two-dimensional imaging was made possible in 1996, when the analog correlator used by NRH was upgraded into a digital one (Kerdraon and Delouis 1997). The first two-dimensional images were produced using the north–south array together with the western 17 antennas of the east–west array (i.e., excluding the 10 m antennas). Because all the antennas of the east–west array were not used in the two-dimensional imaging, the spatial resolution of the two-dimensional images was four times lower than in one-dimensional east–west scans. The current version of NRH uses all the antennas, including the four outside the arrays, for two-dimensional imaging so spatial resolution does not suffer.

The total number of correlations possible with the array configuration that was used for the first two-dimensional images was 861. This included many redundant correlations that were not needed, mostly in the directions of the north–south and east–west arrays, and thus the first digital correlator was limited to 576 correlations. This number included all the products between north–south and east–west antennas as well as some redundant correlations. The current correlator, installed in 2015, can handle all the correlations between all the 47 antennas.

From the correlator the correlations are passed on to a computer, which calculates the visibilities and calibrates the data. Calibration is done based on observations of known sources of intense radio emission, like the radio galaxy Cygnus A, one of the strongest observable radio sources in the sky. In addition to data processing the computer also handles data storage. The computer produces and displays some raw images in real time. This is done to ensure that the system works correctly, and this also allows some measure of real time scientific interaction.

5.1.2 Atmospheric Imaging Assembly (AIA)

The *Atmospheric Imaging Assembly* (AIA; Lemen et al. 2012) is an EUV imaging instrument that provides continuous full-disk observations of the solar chromosphere and corona up to 0.5 $R_\odot$ above the solar limb. AIA is a part of NASA's *Solar Dynamics Observatory* (SDO; Pesnell et al. 2012) mission, which was launched in February 2011. The primary goal of SDO has been to enhance our understanding of how the Sun influences the Earth and near-Earth space. AIA has worked towards this goal by providing high cadence and high resolution images of the Sun's atmosphere at a multitude of wavelengths, enabling the study of coronal variations and the evolution of the solar magnetic environment.

AIA consists of four telescopes that image the Sun and its atmosphere at seven different EUV wavelengths. In addition to EUV imaging, AIA provides images of the Sun at two UV wavelengths as well as one visible wavelength. The visible bandpass enables coalignment with images from other telescopes. Three of the telescopes have

Table 5.1 The wavelengths observed by AIA, along with their primary ions. The temperature is the characteristic emission temperature corresponding to the wavelength. Adapted from Lemen et al. (2012).

Channel	Primary ion(s)	Region of atmosphere	T [K]
4500 Å	continuum	photosphere	5000
1700 Å	continuum	temperature minimum, photosphere	5000
1600 Å	C IV + continuum	transition region, upper photosphere	1.0×10^6
335 Å	Fe XVI	active-region corona	2.5×10^6
304 Å	He II	chromosphere, transition region	5.0×10^5
211 Å	Fe XIV	active-region corona	2.0×10^6
193 Å	Fe XII, XXIV	corona and hot flare plasma	1.6×10^6, 2.0×10^7
171 Å	Fe IX	quiet corona, upper transition region	6.3×10^5
131 Å	Fe VIII, XXI	transition region, flaring corona	4.0×10^5, 1.0×10^7
94 Å	Fe XVIII	flaring corona	6.3×10^6

two EUV bandpasses, while the remaining telescope houses an EUV bandpass on one half and a broadband UV coating on the other half. The visible bandpass filter is also included on this telescope. The desired wavelength channel is chosen using a filter wheel in three of the telescopes, while one uses a selector mechanism for this.

The EUV wavelengths range from 94 Å to 335 Å, and together with the UV and visible wavelengths they correspond to temperatures ranging from 5000 K all the way to 20 MK. All ten channels are listed in Table 5.1. All of the EUV wavelengths correspond to emission lines of iron (and in one case of helium) ions, and these are also listed in Table 5.1. The table also lists the likely source regions of the radiation as well as their characteristic emission temperatures.

When EUV radiation enters one of the telescopes, it is passed via the primary and the secondary mirrors to the charge-coupled device (CCD), which is the same for all telescopes. Each CCD has 4096×4096 pixels, and each pixel has a size of 12 µm, which corresponds to 0.6 arcsec. This gives all of AIA's telescopes a field of view of 41 arcmin along the detector axes. The spatial resolution that is achieved with AIA is 1.5 arcsec.

The standard temporal resolution of AIA is 12 seconds. In that 12 seconds each telescope can take two pictures, which means that an image at each of the EUV and one of the UV (or visible) wavelengths is produced. As each 12 seconds is divided into two 6 second intervals, one for each bandpass, and 3.1 seconds is needed to perform the camera readout and other system functions, in normal operations the maximum exposure time is 2.9 seconds. If the need arises, however, the cadence can be shortened to 10 seconds, which shortens the exposure time to around 2 seconds.

SDO was placed into an inclined geosynchronous orbit 35 800 km above the surface of the Earth. This orbit is such that it not only permits continuous transmission

of data from the satellite down to the ground, but also gives SDO an almost uninterrupted coverage of the Sun for months at a time. From the entire year, a total of around 44 hours of coverage is lost due to eclipses of the Sun by the Earth. The coverage loss happens twice a year, taking place over some weeks around the equinoxes. In addition to the Earth blocking the Sun, SDO will experience a few lunar transits per year, though this does not cause much data loss.

The AIA images are distributed to the public as FITS files (Pence et al. 2010), and they are made available at Level 1 or Level 1.5 processing. Level 1 processing includes for example filtering for bad pixels and orienting the picture such that the solar north points up. Level 1.5 processing includes for example scaling all the images to the same scale and shifting the image so that the center of the Sun is in the middle of each image. Additionally Level 1.5 AIA data come with magnetograms provided by *Helioseismic Magnetic Imager* (HMI), another instrument on board SDO. The file header structure for both Level 1 and Level 1.5 images is the same, i.e., both have the same keywords but the values reflect the level of processing.

SDO has been observing the Sun for over 10 years and continues to do so to this day, more than doubling the initial baseline mission lifetime of five years. Indeed, it is expected that SDO and its instruments will continue to work and observe the Sun for at least another decade (Johnson-Groh 2020), providing valuable data to the scientific community.

5.1.3 Sun Watcher Using Active Pixel Sensor and Image Processing (SWAP)

Like AIA, the *Sun Watcher Using Active Pixel Sensor and Image Processing* (SWAP; Halain et al. 2013; Seaton et al. 2013) is an EUV telescope, but unlike AIA, SWAP observes the Sun only at one bandpass that is centered around 174 Å. SWAP is on board ESA's *Project for On-Board Autonomy 2* (PROBA2; Santandrea et al. 2013) mission, which was sent into space in November 2009 and which is one of a series of microsatellites launched by ESA, whose main objective "is the demonstration and validation in flight of innovative space technologies and techniques, in order to promote their utilisation in future space missions" (Santandrea et al. 2013). While this is the main objective of the missions, the PROBA satellites also include science payloads, one of which is SWAP

While at first glance it seems that SWAP does not offer much compared to AIA, with only one EUV bandpass compared to AIA's seven, and lower spatial and temporal resolution, the data it produces is still useful for the scientific community. Where SWAP excels over AIA and other instruments is that at 54 arcmin it offers the widest field of view of the Sun from Earth's orbit. During nominal operations SWAP has a temporal resolution of about two minutes.

Whereas AIA uses CCD detectors, SWAP employs a complementary metal-oxide-semiconductor active-pixel sensor (CMOS-APS) technology. It is the first such detector to be used for scientific solar observation from space. The sensor has 1024×1024 pixels with a pixel size of 18 µm, which corresponds to 3.2 arcsec. The CMOS-APS is more resistant to blooming during bright solar phenomena such as strong flares than the detectors used in many other instruments.

The bandpass centered on 174 Å was chosen for SWAP because it "contains the brightest coronal emission lines in the EUV spectrum, and simultaneously provides satisfactory response to emission from the features and events that serve as the drivers of space weather" (Seaton et al. 2013). There are three primary emission lines in SWAP's bandpass, one of Fe IX (171.07 Å) and two of Fe X (174.53 Å, 177.24 Å), with the Fe IX line being the most intense one.

PROBA2 was placed into a circular Sun-synchronous orbit with an altitude of 730 km. The orbit was chosen such that it provides the satellite an almost continuous view of the Sun, with a limited eclipse season from mid-November until the end of January. During the eclipse season the Sun is eclipsed by the Earth for a maximum of 18 minutes per orbit, and for the rest of the year the satellite can observe the Sun without interruption.

There is one special feature in PROBA2 that can be used to better observe and track CMEs, and that is the ability to quickly adjust the pointing of SWAP in any direction. This functionality leverages the nearly real-time onboard processing of SWAP images, as this allows the onboard detection of eruptive events in some predefined set of sectors. If such an event, a CME for example, were detected by the computer, an off-pointing procedure that enables SWAP to follow the CME as it propagates outward from the Sun would be triggered. Image cadence can also be increased in order to better capture the event.

While in theory this ability increases SWAP's total field of view by a factor of three, in reality there are limitations that many times make the process not worthwhile. A big limitation is the fact that the onboard software has trouble identifying CMEs correctly from other bright transients that may appear in the images. There have also been relatively few events bright enough to be seen well outside SWAP's normal field of view to make the off-pointing procedure worth the effort.

The off-pointing ability can, however, also be used to create a mosaic image with an extended field of view to better show large-scale coronal structures. An example showing the extent to which the field of view widened can be seen in Figure 5.1, in which the mosaic image's field of view is compared to SWAP's nominal field of view as well as to AIA's field of view. In the figure we also see how some coronal structures may not fully fit into AIA images, but can be observed in images taken by SWAP.

The images taken by SWAP are available to the scientific community as FITS files at two different data levels. Level-0 refers to uncalibrated images, and Level-1 to calibrated and corrected images. Additional information is included as keywords in

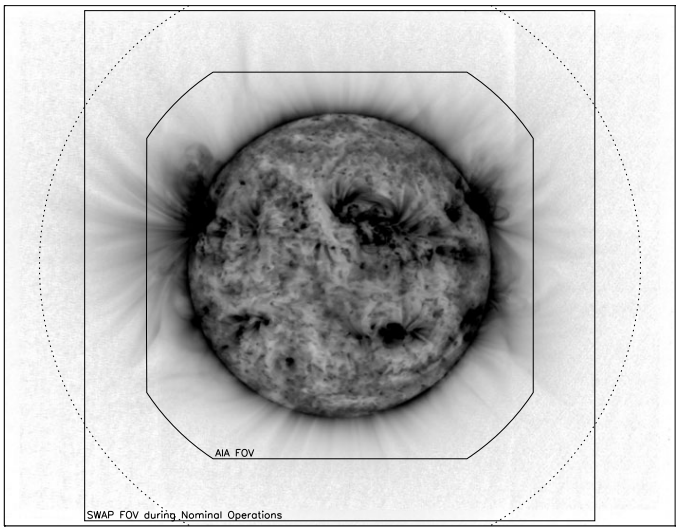

Figure 5.1 Comparison between the standard SWAP and AIA fields of view and the field of view of a mosaic image produced using SWAP's off-pointing ability. The dotted line marks the two solar radii distance from the center of the Sun. Reprinted from Seaton et al. (2013).

the FITS headers, with the Level-0 image headers containing all information needed to calibrate the images. The Level-0 archive contains all the images taken by SWAP, while the Level-1 archive contains only images useful for scientific analysis.

5.1.4 Large Angle Spectroscopic Coronagraph (LASCO)

The *Large Angle Spectroscopic Coronagraph* (LASCO; Brueckner et al. 1995) is an imaging instrument consisting of three coronagraphs, C1, C2, and C3, observing the solar corona from 1.1 to 30 $R_\odot$. Two of the coronagraphs, C2 and C3, are white-light coronagraphs. The C1 coronagraph, which is no longer operational, was equipped with a Fabry–Pérot interferometer, which could be used to produce images of the low corona in narrow passbands in wavelength in the visible domain.

LASCO is part of the *Solar and Heliospheric Observatory* (SOHO; Domingo et al. 1995b) mission, which is a joint project of ESA and NASA, launched in December 1995. The main objectives of the SOHO mission have been "to reach a better understanding of the structure and dynamics of the solar interior using techniques of helioseismology" (Domingo et al. 1995a), and also "to gain a better insight into the physical processes that form and heat the Sun's corona, maintain it and give rise to its acceleration into the solar wind" (Domingo et al. 1995a). SOHO includes 12 instruments that employ a number of different techniques to observe the Sun and its surrounding space.

The C2 and C3 coronagraphs are externally occulted and observe the Sun in visible light. The field of view of C2 is from 1.5 to 6 $R_\odot$, while the field of view of C3 is

from 3.7 to 30 $R_\odot$. The wide field of view of C3 makes LASCO the first instrument to image the solar corona beyond 10 $R_\odot$. In addition to the external occulter, which blocks out most of the photospheric light incident on the instrument, the telescope design for both C2 and C3 includes an internal occulter as well. This functions to suppress the largest source of stray light in the coronagraph, i.e., the diffracted light originating from the edges of the external occulter. The pixel size is 11.3 arcsec in C2 and 56.3 arcsec in C3, meaning that the telescopes have spatial resolutions of around 23 arcsec and 113 arcsec, respectively. For both telescopes the spatial resolution is maintained over most of the field of view, but there is a loss of resolution due to vignetting near the inner edge of the field of view.

Each telescope uses a front-illuminated 1024×1024 pixel CCD to record the images of the solar corona. The pixels are 21 µm on a side, and scaling that with the field of view gives each of the telescopes the effective pixel size in arcsec mentioned above. Exposure times used for capturing the images are on the order of a few minutes. This means that for example dark current, which is thermally generated noise in the CCD sensor, is negligible. After exposure the image is read at 50 000 pixels per second, meaning that it takes a little over 20 seconds to read out one full image.

SOHO is in a halo orbit around the L_1 Lagrangian point of the Sun–Earth system, which is located around 1.5×10^6 km from the Earth on the Sun–Earth line. The halo orbit means that SOHO is not situated at the L_1 point, but rather orbits around it. This orbit was chosen because it allows SOHO's instruments a continuous view of the Sun. From its orbit SOHO continuously transmits science data, which is received using NASA's Deep Space Network (DSN). The data is forwarded to NASA's Goddard Space Flight Center (GSFC) in Greenbelt, Maryland, where it is analyzed and made available to the science community.

The SOHO mission was originally designed to be a two-year mission, with sufficient onboard consumables for a total of six years. The mission, however, proved so successful that the satellite continues to observe the Sun and transmit the data to Earth to this day. As of 2020 the SOHO mission has been extended at least until the end of 2022 (ESA 2019). With regard to CME research, LASCO has gone on to provide by far the largest CME dataset to date. From 1996, when SOHO first started to send data, to the end of 2011 the number of CMEs observed by LASCO was around 18 000 (Howard 2014), and the dataset has just been growing since then.

5.2 Observations

In the previous section the sources of the data used in this thesis were described. In this section the radio and EUV data employed in the analysis are discussed. Before that however we summarize what is known about the CME in question based on a number of earlier studies.

5.2.1 The CME of May 22, 2013

The CME that is studied in this thesis erupted on May 22, 2013. It was observed in white light by several coronagraphs, namely LASCO C2 and C3 on board SOHO, and COR1 and COR2 of the *Sun Earth Connection Coronal and Heliospheric Investigation* (SECCHI; Howard et al. 2008) on board the twin *Solar Terrestrial Relations Observatory* (STEREO; Kaiser et al. 2008) spacecraft. LASCO images show the CME from Earth's perspective, while STEREO-A and STEREO-B had longitudinal separations of 137° and −141° from the Earth, respectively (STEREO locations given by the STEREO Science Center's "STEREO Orbit Tool", found at `https://stereo-ssc.nascom.nasa.gov/cgi-bin/make_where_gif`). The positions of the two spacecraft with respect to the Sun and the Earth are shown in Figure 5.2. In addition Figure 5.2 also includes the propagation direction of the CME. According to graduated cylindrical shell (GCS) modeling (Thernisien et al. 2006, 2009) conducted by Ding et al. (2014) and Palmerio et al. (2019), the longitude (the angle with respect to the Sun–Earth line) of the expanding CME was about 70°.

The CME was first observed from Earth's perspective by the LASCO C2 coronagraph at 13:25 UT (see Figure 5.3), though it could be seen in images taken by the inner coronagraph COR1 of STEREO-A even earlier, at 13:00 UT. Cheng et al. (2014), who studied the early kinematics of the CME in question, determined that the impulsive acceleration phase, characterized by an exponential increase of velocity, of the magnetic flux rope associated with the CME started around 12:31 UT. The CME erupted from NOAA[9] active region (AR) 11745, at that time found on the northwestern limb of Sun as seen from Earth. The source region of the eruption was located at $(\theta, \phi) = (13°, 70°)$ in Stonyhurst coordinates.[10] Coronagraph data show that as the CME evolved it appeared as a full halo CME from all three available perspectives (Palmerio et al. 2019).

The CME was a fast one. Palmerio et al. (2019) report that based on the GCS model the speed of the CME was around 1500 km s^{-1}. This fits well both with the SOHO/LASCO CME catalog (Gopalswamy et al. 2009; `https://cdaw.gsfc.nasa.gov/CME_list`), which lists the plane-of-the-sky speed as 1466 km s^{-1}, and the results of the analysis done by Ding et al. (2014), who estimated the CME speed to be 1439 km s^{-1}. Looking at major solar eruptions of solar cycle 24, Gopalswamy et al. (2014) estimate that the CME had a peak speed of 1881 km s^{-1}.

[9] National Oceanic and Atmospheric Administration.

[10] The Stonyhurst coordinate system is one of the heliographic coordinate systems used to identify positions of features on the surface of the Sun, the other major one being the Carrington system. Whereas the Carrington system rotates along with the rotation of the Sun, the Stonyhurst remains fixed with respect to the Earth. The origin of the system is located at the intersection point of the solar equator and the solar central meridian as seen from Earth. Latitude θ increases towards north, and longitude ϕ increases towards the west limb of the Sun (i.e., to the right in solar images). In Stonyhurst coordinates the origin is the same for non-terrestrial observers as well, so that for them too it is determined by the central meridian from Earth's perspective (Thompson 2006).

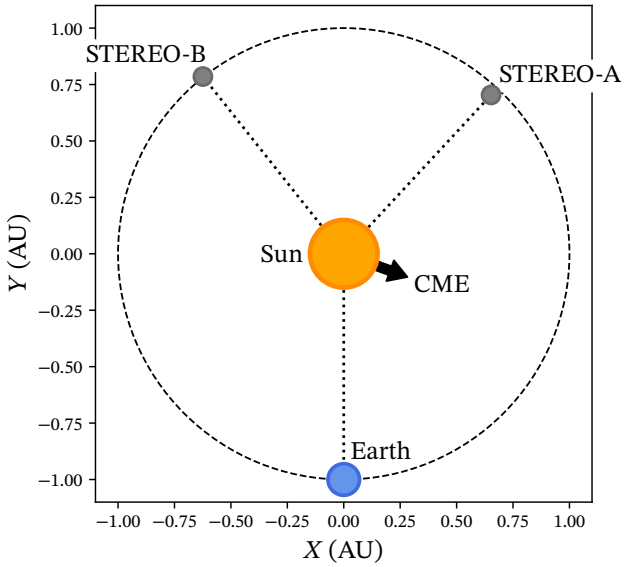

Figure 5.2 The location of the Earth and the two STEREO spacecraft around the Sun on May 22, 2013 at 12:00 UT. The longitudinal separation between the Earth and STEREO-A was 137°. Between the Earth and STEREO-B it was 141°, and between the two spacecraft the separation was 82°. The arrow indicates the propagation direction of the CME, which was around 70° in Stonyhurst longitude, based on modeling done by Ding et al. (2014) and Palmerio et al. (2019).

The CME was associated with an M5.0-class solar flare (as measured by the Geostationary Environmental Satellites; GOES) that originated from the same active region. The flare initiated at 13:08 UT, reached maximum flux at 13:32 UT and declined after that. In total the flare lasted for about an hour.

The fast CME studied in this thesis was preceded by another CME that erupted from the same source region 4.5 hours earlier, at around 07:00 UT (Palmerio et al. 2019). The preceding CME first appeared in coronagraph images at around 08:00 UT, when it was observed by COR1. The first image taken of it by LASCO was at 08:48 UT, when it appeared in C2's field of view (Mäkelä et al. 2016). The LASCO CME catalog lists the speed of this event as 647 $\mathrm{km\,s^{-1}}$, i.e., though faster than average, still much slower than the CME that followed it some hours later. As reported by Palmerio et al. (2019), LASCO/C3 images show that around 15:30 UT the later, fast CME caught up with the slower one preceding it, and they merged at a heliocentric distance of around 20 $R_\odot$. More detailed analysis of the fast CME catching up with the preceding slower one, conducted previously by Ding et al. (2014), confirms this. After that they continued propagating through interplanetary space as one.

Later on, the merged CME arrived at Earth and was the cause of some geomagnetic disturbance. According to Palmerio et al. (2019) the shock driven by the merged CME showed up in the in situ measurements made by the instruments on board the

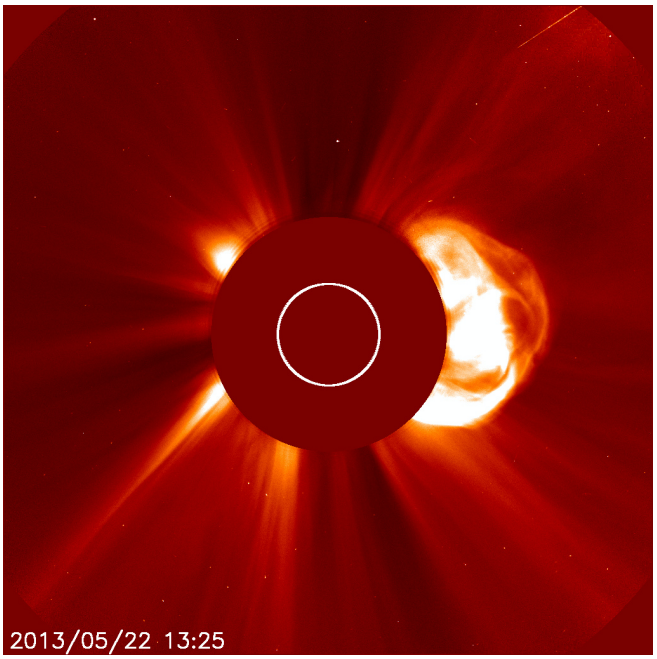

Figure 5.3 The first image (from Earth's perspective) of the May 22, 2013 CME studied in this thesis, taken by the LASCO C2 coronagraph at 13:25 UT (image courtesy of NASA/ESA).

Wind (Ogilvie and Desch 1997) spacecraft at the L_1 Lagrangian point on May 24 at 17:26 UT. In addition, the effects of the shock were also recorded in the in situ measurements made by STEREO-A on May 25 at 06:05 UT. The shock arrived at Earth over the next 12 hours from being detected at Wind. Over that time period the disturbance storm time (Dst) index[11] reached a minimum value of around −60 nT, indicating a moderate geomagnetic storm.

When the CME erupted and propagated through the corona it was accompanied by a host of radio emission. Palmerio et al. (2019) report two separate type II radio

[11]The disturbance storm time (Dst) index (see, e.g., Gonzalez et al. 1994; Kamide and Maltsev 2007) is a geomagnetic index used as a measure of the intensity of geomagnetic activity or a geomagnetic storm. The Dst index measured the change in the Earth's magnetic field due primarily to changes in the *ring current* encircling the Earth. The ring current is a circular band of energetic charged particles lying in the equatorial plane and circulating westward around the Earth. This current produces a magnetic field opposite to that of the Earth's magnetic field. A geomagnetic storm may be caused when energetic particles from the solar wind are injected into the ring current, enhancing it and as a result strengthening its magnetic field. This in turn causes a depression in the horizontal component of the Earth's magnetic field, resulting in the geomagnetic storm, or at least a geomagnetic disturbance. The Dst index is measured in nanoteslas and a negative value indicates a geomagnetic disturbance or storm. A common classification for the intensity of a storm is that a peak Dst of −100 nT or less is an intense storm, between −100 nT and −50 nT is a moderate storm, and between −50 nT and −30 nT is a weak storm. A Dst value of around 0 nT indicates that the ring current is undisturbed, but this is not typical. An enhanced ring current, meaning a Dst value of about −20 nT is normal and does not point to significant geomagnetic activity or storm-level conditions.

bursts, an intense type III radio burst, and a type IV continuum burst. Ding et al. (2014) and Mäkelä et al. (2016) report only the second type II and the type III, but Ding et al. (2014) agree with Palmerio et al. (2019) that the type III is associated with the flare and caused by electron acceleration at the flare site. The reason they do not mention the first type II or the type IV is that they only analyze the dynamic spectra from the *Radio and Plasma Wave Investigation* instruments on board Wind (WAVES; Bougeret et al. 1995) and the twin STEREO spacecraft (S/WAVES; Bougeret et al. 2008), and the type II is obscured by the type III in those data and the type IV is outside their frequency range. Palmerio et al. (2019) also look at the data from the *Nançay Decametric Array* (NDA; Boischot et al. 1980), which shows the start of the first type II burst as well as the type IV continuum. In addition to the type IV seen in the NDA dynamic spectrum a second, shorter duration type IV radio burst can be seen in data captured in a higher frequency range by the ORFEES (Observations Radio pour FEDOME et l'Étude des Éruptions Solaires; `https://www.obs-nancay.fr/orfees`) radio spectrograph.

The first type II burst occurred from 12:55 UT to 13:35 UT starting at around 50 MHz and ending up at 1.2 MHz. The source region for this burst could not be determined, because the burst occurred below the frequency range of NRH and thus comparison with EUV images was not possible. The second type II started around 13:11 UT at about 190 MHz, and comparison of NRH images with EUV images suggested that this type II originated around the source region of the CME. Palmerio et al. (2019) conclude that since the two type IIs had very similar drift rates and only one CME could clearly be seen, it is likely that both bursts were caused by the same shock driven by the CME.

5.2.2 Radio data

The focus of this thesis is radio emission associated with a CME, so the main data source for the analysis conducted is the Nançay Radioheliograph (NRH). Here we are only concerned with the data used in this thesis, the instrument itself is described in Section 5.1.1. The NRH data were obtained from the Solar Radio Data Base website (`https://rsdb.obs-nancay.fr`).

The data are distributed as binary files in a Nançay proprietary format, which contain the visibilities measured by NRH. Visibility is the quantity recorded by an interferometer, and mathematically it is the Fourier transform of the observed sky brightness distribution (for a description of the basic theory of interferometry see, e.g., Condon and Ransom 2016; Wilson et al. 2009). However, in reality getting the radio images from the measured visibilities is not as simple as taking a Fourier transform of the data. This is because interferometers consist of a collection of antennas and as such cannot map the entire *uv*-plane, but only sample part of it. Therefore, the data actually consists of the true visibilities modified by a sampling function,

which contains information regarding the coverage of the *uv*-plane achieved by the array. Fourier transforming the visibility modified by the sampling function gives the so-called *dirty image*, or *dirty map*.

The effects of the incomplete sampling need to be removed in order to get as close to the true sky brightness distribution as possible. The process by which this is done is called *deconvolution*. The name is such because the dirty image is formed by the convolution of the true image with the *dirty beam*, which is the Fourier transform of the sampling function (Clark 1995), and the goal of the process is to remove the effects of this convolution. Deconvolution is done algorithmically, the most popular algorithm being the CLEAN algorithm, first developed by the Swedish radio astronomer Jan Högbom in the early 1970s (Högbom 1974). A variant of this algorithm is used to process the NRH data.

The basic idea of how the CLEAN algorithm works is as follows (see, e.g., Cornwell et al. 1999; Jackson 2008). It is assumed that the radio source can be represented by a finite number of point sources, while the rest of the sky is empty. The highest intensity point in the dirty image is found. At the position of the peak a scaled dirty beam is subtracted off and the position and magnitude of the subtracted point are noted down. This is repeated until the peak is under some threshold. The remaining map is known is as a residual map and it consists only of noise. The points that were removed from the dirty image are then convolved with a CLEAN beam (usually an ideal Gaussian shape). Finally, the residual map is added to the CLEAN image, and the resulting map is the final image.

The processing done on the NRH visibility data, the steps of which are outlined above, is conducted using the SolarSoft system (SSW; Freeland and Bentley 2001; Freeland and Handy 1998). SSW is a programming and data analysis environment used in solar physics, and it includes an NRH software package that has tools for processing NRH data. The processed data are packaged into FITS files.

The data consist of observations at nine frequencies: 150.9, 173.2, 228.0, 270.6, 298.7, 327.0, 408.0, 432.0, and 445.0 MHz. The data for each frequency are contained in their own file. The observation period is between 12:45 UT and 13:45 UT on May 22, 2013. The processed data contain measurements of both the Stokes I (total intensity) and V (circular polarization) components of the radio emission, recorded as brightness temperature T_B and measured in kelvins (for a description of brightness temperature see Section 4.1.2).

When computing the radio images from the NRH binary files, the program allows specification of image parameters like field of view and image size. In this case the field of view was chosen to be $6\,R_\odot$, and the image size the possible maximum of 256×256 pixels. Other options were kept at their default values. The integration time for the images was set at 0.9 seconds. The FITS files contain all of the parameters above, and much more, as keywords in the FITS file headers.

Reading the FITS files and extracting the data from them is done using the Python

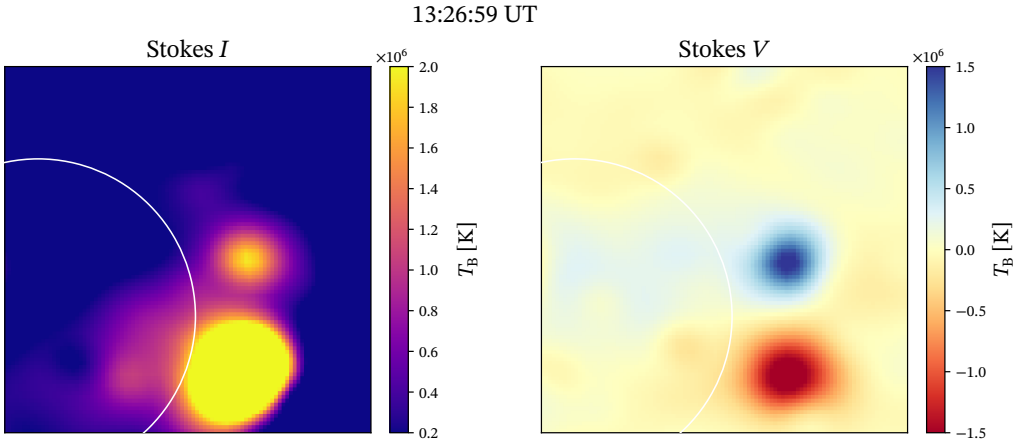

Figure 5.4 An example of processed NRH data visualized. The frequency of the emission here is 150.9 MHz. The left pane shows the total intensity of the radio emission, and the right pane shows the circular polarization of the emission. The circular polarization follows the usual convention of positive V (blue in the figure) indicating left-handed circularly polarized emission, and negative V (red in the figure) indicating right-handed circularly polarized emission. For the left-handed emission the electric field rotates in a counterclockwise manner, and for the right-handed in a clockwise manner. The white circles in the figures indicate the solar limb.

package Astropy (The Astropy Collaboration et al. 2013, 2018), which has extensive FITS file handling capabilities. The solar physics Python package SunPy (The SunPy Community et al. 2020) is used alongside the Python plotting library Matplotlib in visualizing the data. An example of what the processed radio images look like can be seen in Figure 5.4. Both Stokes components are shown in side-by-side images taken at around 13:27 UT at the frequency 150.9 MHz. The example shows two relatively strongly polarized radio bursts that have opposite senses of polarization.

In addition to NRH, data from the ORFEES radio spectrograph is employed in studying the emission associated with the CME. ORFEES consists of a 5 m parabolic dish that is coupled to a spectrograph. It observes the Sun at a temporal resolution of 0.1 s in the frequency range from 144 MHz to 1000 MHz. The data can be visualized in a frequency vs. time dynamic spectrum, which shows the evolution of flux as a function of observation frequency across time (see, e.g., Figure 6.2).

5.2.3 Extreme ultraviolet data

In addition to the main radio emission data, this thesis employs EUV imaging of the solar corona in support of the analysis of the radio data. The data sources for the EUV images are the AIA (described in Section 5.1.2) telescope on board SDO,

and the SWAP (described in Section 5.1.3) telescope on board PROBA2. The SWAP images were obtained from the PROBA2 Science Center website (P2SC; https://proba2.sidc.be/data/SWAP), and the AIA images were acquired via the Virtual Solar Observatory website (VSO; https://sdac.virtualsolar.org/cgi/search).

For AIA images the wavelengths that were chosen were 131 Å, 171 Å, and 211 Å. SWAP observes the Sun at just one wavelength, 174 Å, so those images were used. Here too the FITS files were processed using Astropy and visualization was done using Matplotlib and SunPy. Example images of all of the wavelengths are shown in Figure 5.5.

Even though the AIA images that were used were calibrated and corrected, it turned out that the sets for all wavelengths contained numerous images that had significantly shorter exposure times than normal. The normal exposure time for the AIA telescopes is 2.9 seconds (Lemen et al. 2012), whereas for some images the exposure time was found to be as low as 0.6 seconds. This of course causes the image to be much darker than normal. This in turn would cause problems when looking at running difference images, where the previous image array is subtracted from the current array. If a low-exposure image is subtracted from a normal-exposure one, the resulting difference image is very bright, seeming to be "overexposed". Similarly, if a normal-exposure image is subtracted from a low-exposure one, the difference image appears very dark, or "underexposed". Because of this all images with an exposure time much less than 2.9 seconds were taken out of the dataset. An exposure time of 1.6 seconds was used as the threshold for discarding the image.

The main application of EUV data is in difference images. Difference imaging is a technique in which a preceding image is subtracted from the current one, thus aiding in visualizing transient events such as CMEs. There are two "versions" of difference imaging, *base* and *running* difference imaging. In principle the two techniques are similar, since in both a preceding image is subtracted. They, however, differ in that in base difference imaging all images that are analyzed have the same fixed image that is subtracted from them, whereas in running difference imaging the previous image is subtracted (Pérez-Suárez et al. 2011).

When making difference images from AIA data, it is necessary to smooth out the images or the difference image will end up looking noisy. The smoothing, or noise reduction, can be done by applying an averaging filter such as a uniform filter to the image. A uniform filter replaces each pixel value by the average value of an area centered at that pixel. The larger the area, the more the image is filtered, which in general means that the image gets blurrier. The uniform filter can be applied by using the image processing capabilities of Python's SciPy library (Virtanen et al. 2020). Figure 5.6 shows the effect that applying a uniform filter has on AIA running difference images. Figure 5.6a with no filter applied to it is clearly more grainy than Figure 5.6b, which has a 4×4 uniform filter applied to the images prior to subtraction. Filtering can make features such as the one seen around $(500, 200)$ easier to

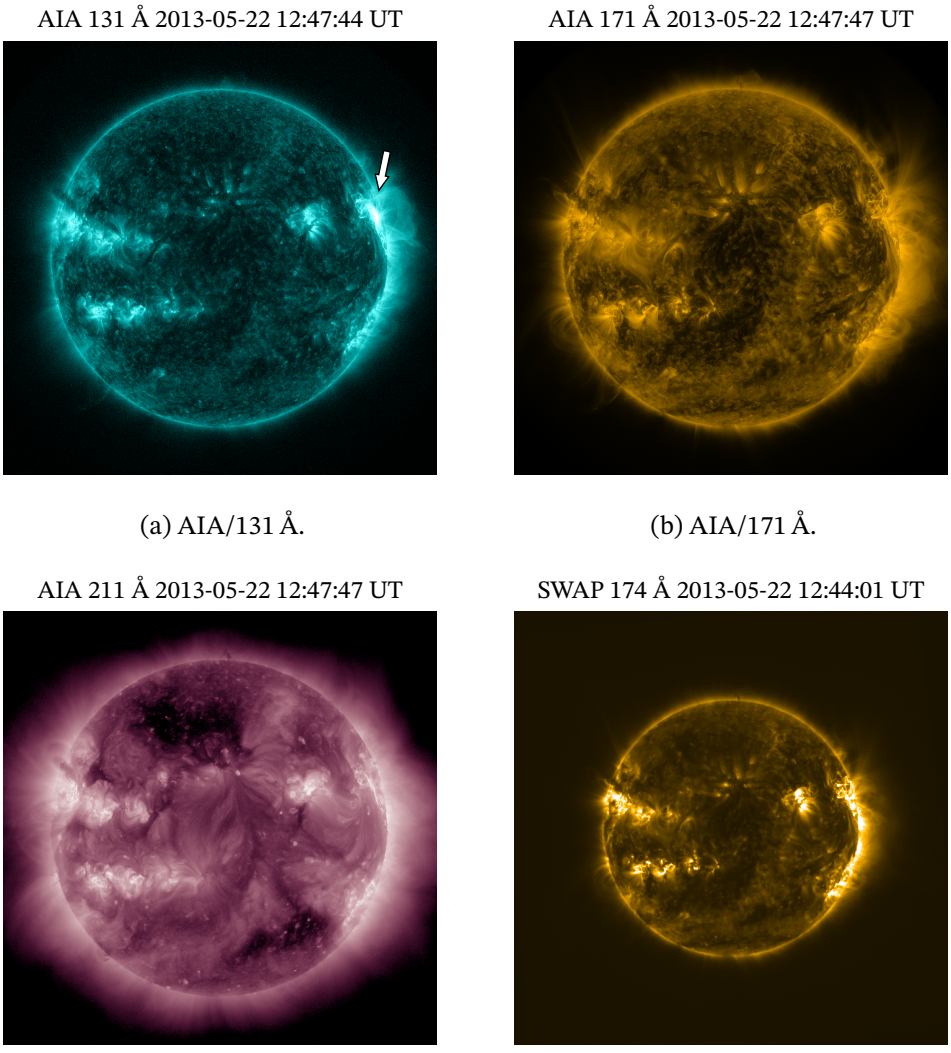

(a) AIA/131 Å.

(b) AIA/171 Å.

(c) AIA/211 Å.

(d) SWAP/174 Å.

Figure 5.5 Examples of images taken by AIA and SWAP at the wavelengths used in this thesis. The CME erupted from the northwestern limb of the Sun. The site of eruption is indicated by the arrow in the 131 Å image. The image also shows the CME itself clearly as it is starting to propagate outwards.

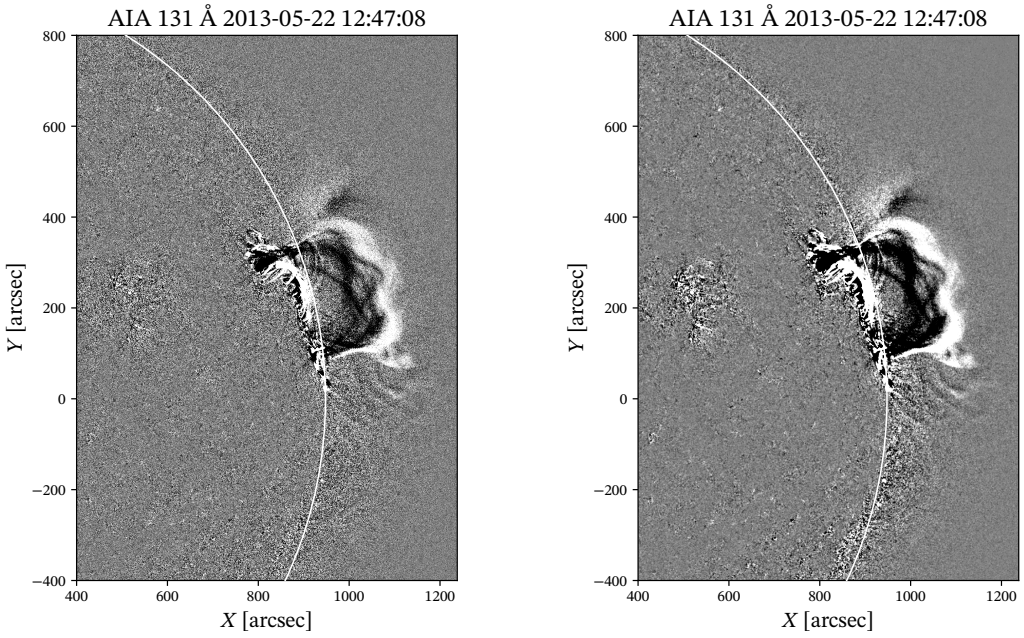

(a) (b)

Figure 5.6 The effect on running difference images of applying a uniform filter to the images before subtracting one from another. Both are the same ten frame AIA running difference image, the one on the left with no filtering and the one on the right with a 4×4 uniform filter applied to it.

distinguish from the background, as is the case here. In this thesis all difference images were filtered prior to subtraction.

5.3 Identifying moving radio bursts

Since NRH produces two-dimensional radio maps of the Sun and its corona, the images can be used in conjunction with white-light and EUV observations of CMEs and flares to identify radio emission associated them. In addition, this also allows for the identification of the source region of the radio emission relative to the solar eruption being studied (see, e.g., Maia et al. 1999a,b; Morosan et al. 2019b; Vasanth et al. 2019).

The starting point of this study was to identify any significant radio bursts that occurred around the time that the CME in question erupted and propagated through the corona. The focus was on seeing if there were any radio bursts that appeared to be moving along with the CME. Using video to search for radio bursts, be they stationary or moving, instead of looking at individual frames makes it easier to distinguish between actual radio bursts and other transient events, which might be caused for

example by instrumental noise. It also makes it easier to identify whether a radio burst is stationary or if it appears to move across the field of view.

In order for a structure seen in the radio images to be identified as a moving radio burst, it should satisfy three criteria. The first criterion is that the source of the radio emission should have a clear structure, and that it should more or less retain that structure throughout its lifetime. If the structure does change, it should change continuously or smoothly and not abruptly. The second criterion is that the burst should be visible in the images over a period of time, on the order of at least tens of seconds to minutes. The burst, in order to be identified as a single burst, should be visible throughout its lifetime and not disappear and reappear in between. If something like this were observed, it may indicate the presence of two separate bursts that happen to appear in the same region. Naturally, the third criterion is that the burst propagates along a path through the corona. It is expected that the path should be more or less continuous and it should have no sudden jumps from one location to another. These sudden jumps may be indicative of other, separate bursts that should be treated as their own events.

Once a moving radio burst has been identified, its start and end times are noted down and the other frequencies are checked to see if the burst is seen in those images. The images that are compiled to video have both Stokes components, I and V, side by side, so the possible polarization properties of the identified bursts can be checked at the same time.

5.4 Tracking the movement of radio bursts

Once a moving radio burst has been identified in the NRH radio images, its movement across the field of view can be tracked. The movement can be tracked by calculating the centroid of the burst as it appears in the image. The centroid of a radio burst can be thought of as the "center of intensity" of the burst, similar to the center of mass of a physical body. This means that the x and y coordinates of the centroid are calculated as weighted averages, where the weights used for the coordinates are given by the measured intensity of the radiation. In general, the weighted average $\bar{x}$ of a dataset $\{x_1, x_2, \ldots, x_n\}$ is calculated as

$$\bar{x} = \frac{\sum_{i=1}^{n} w_i x_i}{\sum_{i=1}^{n} w_i} = \frac{w_1 x_1 + w_2 x_2 + \cdots + w_n x_n}{w_1 + w_2 + \cdots + w_n}, \tag{5.1}$$

where w_i is the weight assigned to the data point x_i.

A function is used to calculate the centroid of a given radio burst. The function is given the array containing the brightness data as an input. As there may be some transient bursts occurring somewhere else in the field of view, the full data array is

not given to the function. Rather, a subarray that contains the radio burst should be given. The subarray is chosen such that the radio burst is contained within it for its entire trajectory. Figure 5.7 shows what this means.

Since the radio images are superimposed onto a helioprojective coordinate system[12], the coordinates of the edges of the bounding box can be read graphically. This gives the coordinates in arcseconds, so it is necessary to convert them to pixels with respect to the lower left corner of the full image. These coordinates correspond to indices of the data array. The NRH FITS file header contains the keyword `SOLAR_R`, which is the solar radius in pixels on the radio images. In arcseconds the solar radius, as seen from Earth, is 959.61 arcsec (Emilio and Leister 2005). From these numbers we get how many arcseconds one pixel corresponds to in the radio images, and this in turn can be used to convert the coordinates of the edges of the bounding box from arcseconds to pixels. In this way it is possible to pick out the desired subarray from the full radio data array.

To minimize the effect of background radiation on the centroid calculation, everything below 50 % of the maximum brightness is set to zero. In Figure 5.7 this threshold is indicated by the contour. We see that this level outlines the brightest part of the burst well. Then, the x- and y-coordinates of the centroid are calculated using Equation (5.1), where now the weights w_i are given by the brightness data, and the points x_i are just the x- or y-coordinates in the subarray (in pixels).

The function returns the coordinates of the centroid in pixels with respect to the lower left corner of the subarray, so that they need to be converted back to the helioprojective coordinates of the full image. The coordinates of the point can be converted from pixels to arcseconds similarly as was done earlier from arcseconds to pixels, by using the scaling factor of how many arcseconds equals one pixel. Then, since the coordinates are given with respect to the lower left corner of the subarray, adding the helioprojective coordinates of the lower left corner to the coordinates of the centroid gives the helioprojective latitude and longitude of the centroid, which can then be plotted into the full image, as seen in Figure 5.7.

Because the bounding box for the moving burst is chosen such that the burst remains inside it for its whole trajectory, the method outlined above can easily be

[12]Helioprojective coordinates express positions of features as projections in the plane of the sky. Helioprojective coordinates are similar to heliocentric coordinates, which describe the actual positions of features, measured in physical units from the center of the Sun. Where the two systems differ is that helioprojective coordinates take into account the fact that a view from a single perspective can only ever be a projection into the plane of the sky, and whereas coordinates are measured in physical units in heliocentric coordinate systems, in helioprojective coordinate systems this is done using angles. Both of these coordinate systems differ from the Stonyhurst coordinates (and heliographic coordinate systems in general) described earlier, in that these systems define the origin as seen by the observer, so that non-terrestrial observers will measure different coordinates from terrestrial observers, whereas observers using heliographic coordinate systems all share the same origin (Thompson 2006). Therefore, as seen from the Earth, the x and y coordinates of a feature are usually measured in arcseconds from the center of the Sun, as is done for example in Figure 5.7.

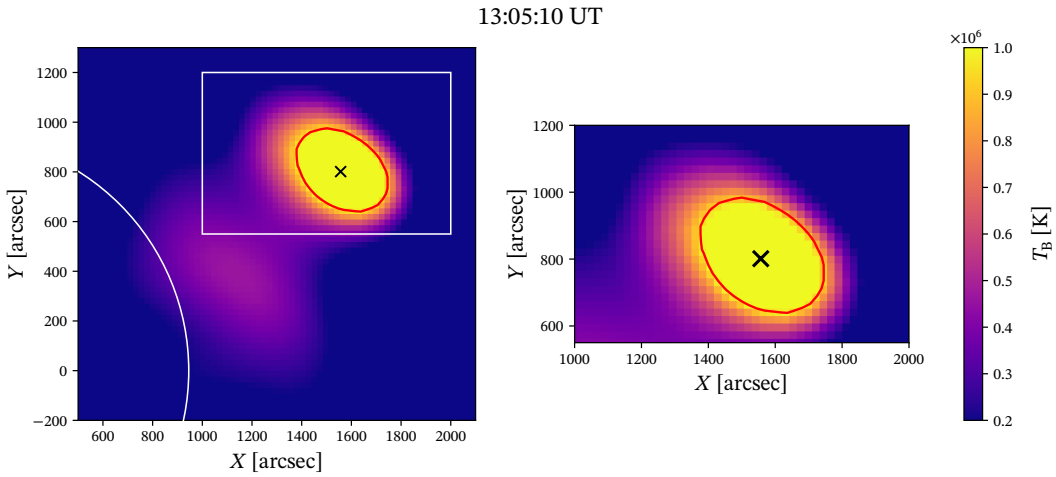

Figure 5.7 The method used to calculate the centroid of a moving radio burst illustrated on a sample image. The radio burst is "boxed off", and the bounding box is chosen so that it contains the full trajectory of the burst. Here, for example, the radio burst propagates roughly from the upper left corner to the lower right corner. The contour indicates the line of 50 % of the maximum brightness. This level is used as the threshold for removing the background, i.e., everything outside the contour is set to zero. The centroid of the radio burst is indicated by the cross.

iterated over all images of the burst and thus used to calculate all the centroids for the burst. Once all of the centroids have been calculated, they are saved to a text file and plotted against AIA running difference images to show the full trajectory that the radio burst traverses in the corona. The times of the images are saved along with the centroid coordinates, and this allows the centroids to be used to estimate the speed of the moving radio burst.

If a burst moves more or less along a clear path, a line can be fitted to the data. In this thesis this was done using Python's NumPy library (Harris et al. 2020). Once the fit is done, the distance propagated by the burst can be estimated from the x- and y-coordinates of the fitted line by

$$\Delta r = \sqrt{(\Delta x)^2 + (\Delta y)^2},$$

which is just the Euclidean distance between the end points of the line.

To estimate the speed of the radio burst the time it takes the burst to propagate from its starting point to its end point is needed. This can be determined for example with Python's `datetime` module (`https://docs.python.org/3/library/datetime.html`), which provides the ability to perform time arithmetic. Then, once both the distance Δr and the time Δt are known, the speed of the moving radio burst

is estimated by

$$v = \frac{\Delta r}{\Delta t}.$$

5.5 Estimating the flux density of a radio burst

From the brightness data provided by NRH it is possible to estimate the flux density S_ν (see Section 4.1) of a radio source. Estimating the flux density of a source at all the frequencies it is visible at may make it possible to estimate the spectral index of the emission. This in turn may give some hint as to what the emission mechanism of the source is.

A solar radio burst has some extent in pixels in the radio image. The flux density of the burst can be estimated by estimating the flux density of each pixel and summing them together. From (4.6) we see that the flux density coming from an individual pixel can be estimated by

$$S_\nu = \frac{2k\nu^2\Omega_{\text{px}}}{c^2} T_{\text{B}}, \tag{5.2}$$

where Ω_{px} is the solid angle one pixel in the image corresponds to. In the code used in this thesis this is given by

$$\Omega_{\text{px}} = \left(\frac{16 \cdot 3 \times 10^{-4}}{R_{\odot,\text{px}}} \right)^2, \tag{5.3}$$

where in the numerator 16 is the angular radius (i.e., half of the angular diameter) of the Sun in arcminutes, and 3×10^{-4} is approximately 1 arcmin in radians ($1\,\text{arcmin} = \pi/10\,800\,\text{rad} = 0.000290888\ldots\text{rad} \approx 3 \times 10^{-4}\,\text{rad}$), so that the numerator is the approximate angular radius of the Sun in radians. In the denominator $R_{\odot,\text{px}}$ is the radius of the Sun in pixels in the radio image. It can be shown that small solid angles can be approximated by $\Omega \approx \pi\theta^2$, where $\theta \ll 1$ is the angular radius of the object whose solid angle is approximated. The solid angle corresponding to one pixel is calculated by dividing the solid angle subtended by the Sun by the area of the Sun in pixels, given by $A_{\odot,\text{px}} = \pi R_{\odot,\text{px}}^2$. Thus in the expression for Ω_{px} given above the factors of π cancel out.

Similarly, as with the centroid calculation, only a subarray containing the observed radio burst is considered (as is shown in Figure 5.7). Also, as with the centroids, to remove the contribution of possible background emission to the flux density, everything below 20 % of the maximum brightness is set to zero in the data array. A lower threshold is chosen for the flux estimation because the edges as well as the bright core of the burst contribute to the flux density, whereas in the centroid calculation the edges do not necessarily need to be included in order to accurately locate the centroid.

Once this is done, the data array containing the radio burst can be iterated over and the contributions of individual pixels to the flux density of the burst are summed to give an estimate of the total flux density of the radio burst. Equation (5.2) gives the flux density in $\mathrm{W\,m^{-2}\,Hz^{-1}}$. In these units the flux density of the burst is very small, so that it is convenient to express it in solar flux units (see Section 4.1.1). Once the flux density is in solar flux units, the above is repeated for all frequencies. Flux density estimates at multiple frequencies can be used to estimate the spectral index of the emission.

5.6 Estimating the spectral index

If a power-law relationship between flux density and frequency is assumed, the spectral index (see Section 4.2) of the emission can be estimated. A power-law relationship between two variables implies a linear relationship between their logarithms.

A general power-law relationship between flux density S_ν and frequency ν can be written as

$$S_\nu(\nu) = C\nu^\alpha, \tag{5.4}$$

where C is some constant and α is the spectral index. Taking a base-10 logarithm of this on both sides and using the properties of logarithms we can write

$$\log S_\nu = \log(C\nu^\alpha) = \log C + \alpha \log \nu = C' + \alpha \log \nu, \tag{5.5}$$

where in the last step we renamed the constant, since the logarithm of a constant is just another constant. We see that there is a linear relationship between $\log S_\nu$ and $\log \nu$, which means that a simple line fit can be used to estimate α.

Once the fit is done, the spectral index is the slope of the resulting line. The results of the flux estimation and line fit can then be plotted together in a log–log plot. The spectral index can be used along with other features of a radio burst to try to determine the emission mechanism behind the observed radiation.

6 | Results

The methods presented in the previous chapter were used to analyze the radio emission associated with the fast CME of May 22, 2013. In this chapter the results of that analysis are presented, starting with the moving radio bursts that were identified. Following this the results of the analysis of the radio bursts' kinematics and spectral properties are described.

6.1 Moving radio bursts

The method described in Section 5.3 was used to study the radio emission at all nine available frequencies, and both the Stokes components, I and V, were analyzed. The time period over which the search for radio bursts was conducted was chosen to be from 12:45 UT to 13:45 UT. The CME started to accelerate in the low corona around 12:31 UT (Cheng et al. 2014), so the start of the observation period corresponds to the CME not being very high yet, at a height of under $2\,R_\odot$ (measured from the center of the Sun). At the end of the observation period the CME had propagated into the field of view of LASCO C3, with the leading edge being at a height of around $6\,R_\odot$. Thus, the observation period corresponds well to the early evolution phase of the CME.

Three moving radio bursts were identified in the NRH radio images. These bursts were labelled Source 1, Source 2, and Source 3, in chronological order. Figure 6.1 shows these radio bursts as contour maps, each at three different times in their evolution, overlaid on top of AIA 211 Å running difference images. The difference images, especially those of Source 1 (top row), clearly show the CME as it propagated through the solar corona. The orange contours show the radio burst at 150.9 MHz, and the green contours at 173.2 MHz. All three bursts were most distinct at 150.9 MHz. They were also visible at 173.2 MHz, but not at any of the higher frequencies from 228.0 MHz to 445.0 MHz observed by NRH. None of the three bursts showed any degree of circular polarization at either of the frequencies.

The first moving source was preceded by a stationary one, which first appeared in the 150.9 MHz images at the very start of the observation period, i.e., around 12:45

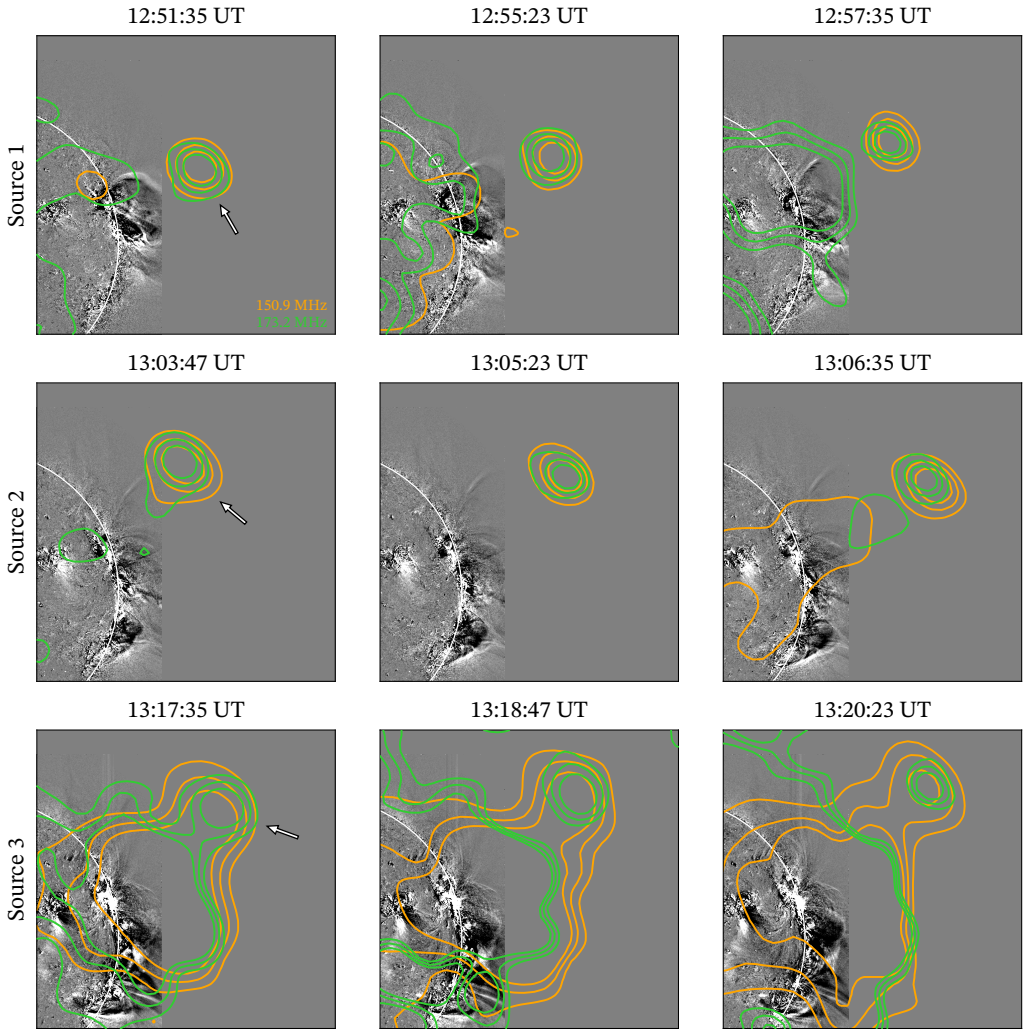

Figure 6.1 Three moving radio bursts, labelled Source 1 (top panels), Source 2 (middle panels), and Source 3 (bottom panels), associated with the May 22, 2013 CME. Each radio burst is indicated by the arrow in the first panel of each row. The contours indicate the lines of 30 %, 50 %, and 70 % of the maximum brightness of the moving radio bursts as seen by NRH at 150.9 MHz (orange) and 173.2 MHz (green). The contours are overlaid on top of AIA 211 Å running difference images, which show the CME as it evolved in the solar corona. The difference images show a difference of 10 images, which corresponds to a temporal difference of two minutes between the subtracted images.

UT. The burst remained stationary for around five minutes, after which it started moving in a northwesterly direction at around 12:50 UT. The radio burst then propagated northwest for about seven minutes before it stopped again. Once it came to a stop, the burst remained visible and stationary for a couple of minutes before disappearing altogether at around 12:59:30 UT.

The second moving radio burst appeared for a shorter period of time than the first one. It first showed up at around 13:03:30 UT, and was not preceded by a stationary burst, so it started moving immediately. The burst moved in a westerly direction, though it did have a small southward component to its movement. After propagating for over three minutes, the burst came to a stop a little before 13:07 UT. After that a stationary burst was visible until around 13:08:30 UT at 150.9 MHz in the region where Source 2 stopped.

A large and bright stationary radio burst appeared above the western limb of the Sun just before 13:10 UT. This burst most likely corresponds to the broadband continuum emission starting around 13:10 UT, which can be seen in the ORFEES dynamic spectrum (Figure 6.2). The broadband continuum nature of the burst suggests that it is a type IV radio burst, and the fact that it shows no significant frequency drift suggests that it may be a stationary type IV radio burst (Liu et al. 2018). The dynamic spectrum shows that the type IV spanned the entire frequency spectrum covered by NRH. Indeed, the burst did appear at all nine frequencies observed by NRH. At and

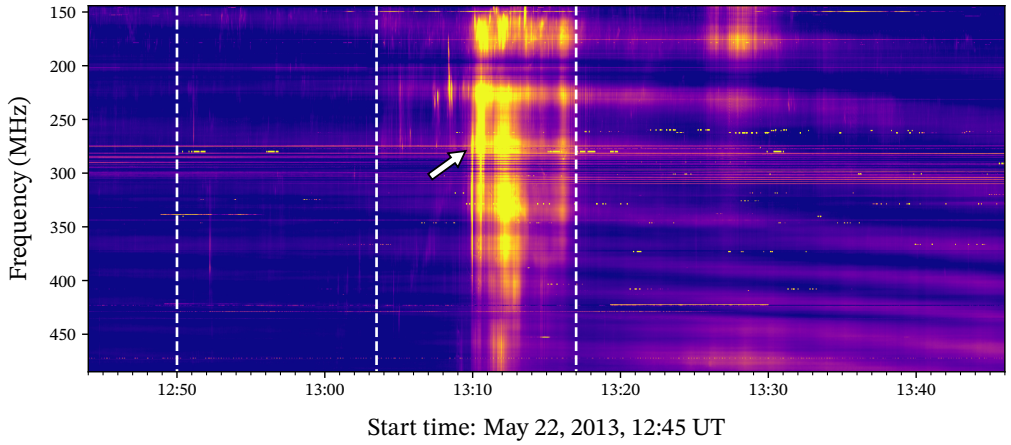

Figure 6.2 ORFEES dynamic spectrum of the observation period from 12:45 UT to 13:45 UT. The broadband continuum emission, indicated by the arrow, started around 13:10 UT. The emission is a type IV radio burst, most likely a stationary one. The source region for this burst is above the western limb of the Sun. The three dashed vertical lines indicate the moving radio bursts, marking the times when they started moving. The locations of the lines show that the moving bursts were not associated with the type IV burst.

above 228.0 MHz the burst appears to have been fairly highly circularly polarized. At first when the burst appears, this polarization was not seen at the lower frequencies.

Initially the bursts at 150.9 MHz and 173.2 MHz had slightly different source regions compared to the bursts at the higher frequencies, which clearly had the same source region. Around 13:15 UT, however, the bursts at all of the nine frequencies lined up nicely, with higher frequency emission coming from closer to the limb and lower frequency emission from higher up. This is a characteristic feature of plasma emission, whose frequency is proportional to the plasma density (Eq. 3.3), and as plasma density generally decreases with increasing distance from the Sun, it is expected that the frequency of radio bursts from plasma emission also decreases when moving higher up in the corona. Therefore, the emission mechanism that caused the type IV radio burst is likely plasma emission. The high degree of circular polarization seen earlier at the higher frequencies was then seen at 150.9 MHz and 173.2 MHz.

A little after this, at around 13:17 UT, the third moving radio source appeared in the 150.9 MHz and 173.2 MHz images. As can be seen from the bottom panels of Figure 6.1, Source 3 was located fairly high up in the corona, to the northwest of the type IV (which is indicated by the contours that cover a large part of the field of view in the bottom panels of Figure 6.1). Source 3 propagated northwest, meaning its direction was similar to that of Source 1. It continued moving northwest until a little after 13:22:30 UT, when it disappeared from view.

The dashed vertical lines in the dynamic spectrum shown in Figure 6.2 indicate the times when each of the three radio bursts started to move in the radio images. We see that all of the three bursts occurred at times different to the type IV. The first one appeared around 20 minutes before the onset of the type IV, the second one about seven minutes before the type IV, and the third one was first seen after the onset of the type IV. These observations indicate that the moving radio bursts were not associated with the type IV. This in turn supports the idea that the stationary burst seen above the western limb in the radio images is the type IV seen in the ORFEES dynamic spectrum.

Figure 6.2 also shows that these three moving radio bursts do not fit the typical classifications, or types, of solar radio bursts. In the dynamic spectrum there are no clearly visible bursts resembling either a type II or a type IV radio bursts that occur around the time when moving bursts were observed. As mentioned above, the moving bursts are not associated with the type IV that is visible in the spectrum. Clearly they are also not associated with the type II bursts that were observed in conjunction with the CME. Type III radio bursts can also be associated with a CME, but there are no type III-like structures visible near any of the dashed lines, so the moving bursts are no type IIIs either. Thus it can be concluded that the observed moving radio bursts are some atypical type of radio emission.

6.2 Radio burst kinematics

The methods described in Section 5.4 were used to first calculate the centroids of the three identified moving radio bursts, and based on the results estimate the speeds of the bursts. All of the bursts were seen most clearly at 150.9 MHz, so that brightness data was used when calculating the centroids of all three bursts. The centroids were overlaid on top of AIA running difference images (see Figure 6.3), showing the full trajectories of the bursts through the corona.

The centroids overlaid on top of the AIA running difference images show the trajectories of the moving bursts more clearly than the contour maps of Figure 6.3. We see that Source 1 is well in front of the CME, whose leading edge can be seen in the

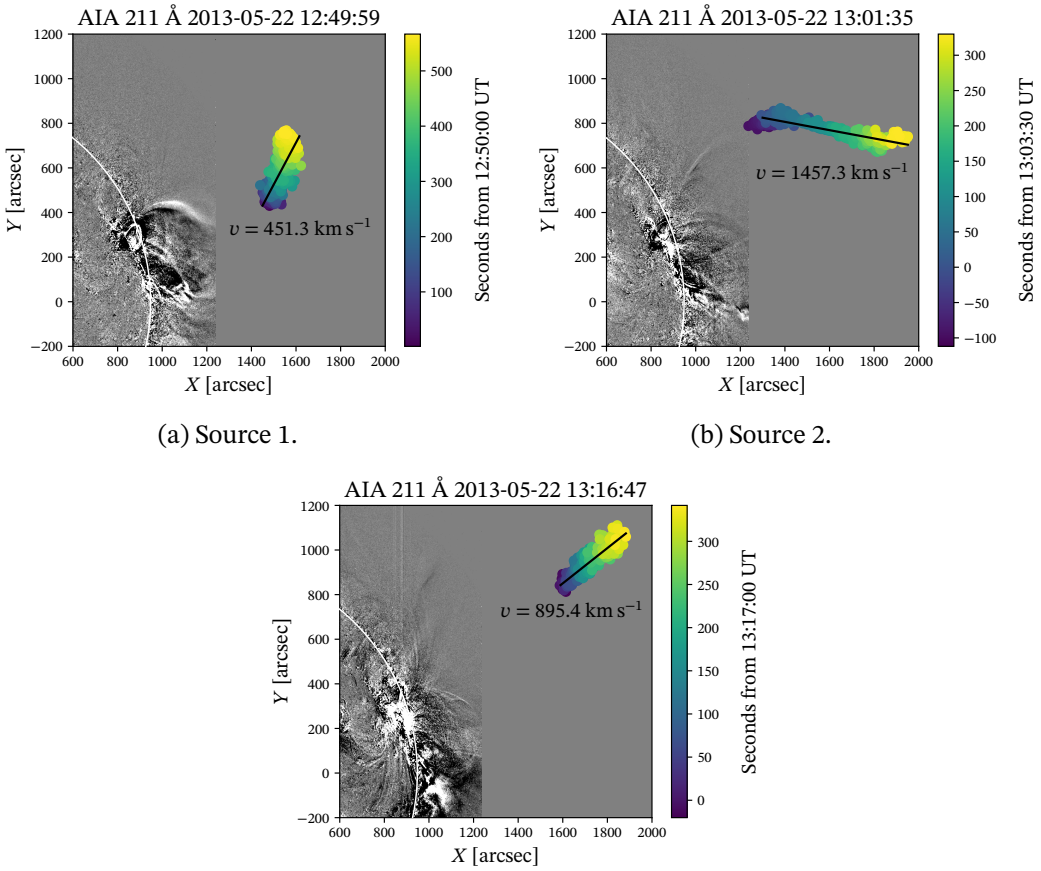

(a) Source 1.

(b) Source 2.

(c) Source 3.

Figure 6.3 Centroids of the three moving radio bursts overlaid on top of AIA ten frame running difference images. For each burst the color of the centroids indicates time in seconds since the start of the burst. Plotted on top of the centroids are the line fits that were used to estimate the speed of each moving burst. The resulting estimated speeds are also included in the plots.

difference image, extending just beyond the field of view of AIA. The centroids show that the burst propagated almost straight north, having just a small westerly component to its movement. In contrast, Source 2 moved almost straight west, having a small southward component to its direction. Finally, Source 3 is between these two, since it moved in almost a straight northwestern direction.

The relationship between the CME and Sources 2 and 3 is not as clear from Figures 6.3b and 6.3c as it is for Source 1 in Figure 6.3a. This is because the CME structure is not as clearly visible in the later running difference images as it is at the start of the CME's evolution. The northern and southern flanks the of the CME can be distinguished in Figure 6.3b The northern flank is indicated by the streak that extends northwest from around the point (1000, 600). The streak appears to be curving to the west, which indicates that Source 2 originated near the northern flank of the CME, though it propagated in the direction of the CME front. The location of Source 3 relatively high up to the north suggests that it too originated near the northern flank of the CME.

From the centroids the estimated speeds of the three radio bursts were found to be ~450 km s^{-1}, ~1500 km s^{-1}, and ~900 km s^{-1}, respectively. We see that the speed of Source 2 matches the speed of the CME fairly closely, though at the time when Source 2 is observed the CME is still relatively early in its evolution, so that it may not have accelerated to its peak speed yet. Source 1 seems to be significantly slower than the CME, and Source 3 too is somewhat slower than the CME. Here again it may be that the speed of the CME is closer to that of Source 1, when the CME has just erupted. With regards to the speeds, it is important to note that they are only plane of the sky estimates of the true speeds of the radio bursts. This is because, just as with any coronal features, the radio bursts recorded by a radioheliograph are projected on to the plane of the sky, and as such are subject to projection effects. It is more likely that the moving bursts propagated at least to some degree outside the plane of the sky than exactly along it. In such a case the estimated speed is a lower limit of the true speed of the burst.

The centroids were also used to study how the heights of the radio bursts evolved in time. Since in this case height is just the heliocentric distance, i.e., radial distance from the center of the Sun, the height h of a radio burst can be estimated from the coordinates of its centroids by $h = \sqrt{x^2 + y^2}$. Figure 6.4 shows the moving radio bursts in blue (Source 1), orange (Source 2), and red (Source 3), along with the kinematic evolution of the CME and the two associated type II radio bursts studied by Palmerio et al. (2019). We see that the height evolution of Source 1 matches well with the early evolution of the CME as determined from EUV images (indicated by the plus symbols), and also of the evolution of the northern flank of the CME, which was seen in white-light images (indicated by the asterisks). The height evolution of Source 2 matches up with that of the shock nose, or even the southern flank. Though this appears curious, as the centroids and the EUV images suggest that Source 2 originated

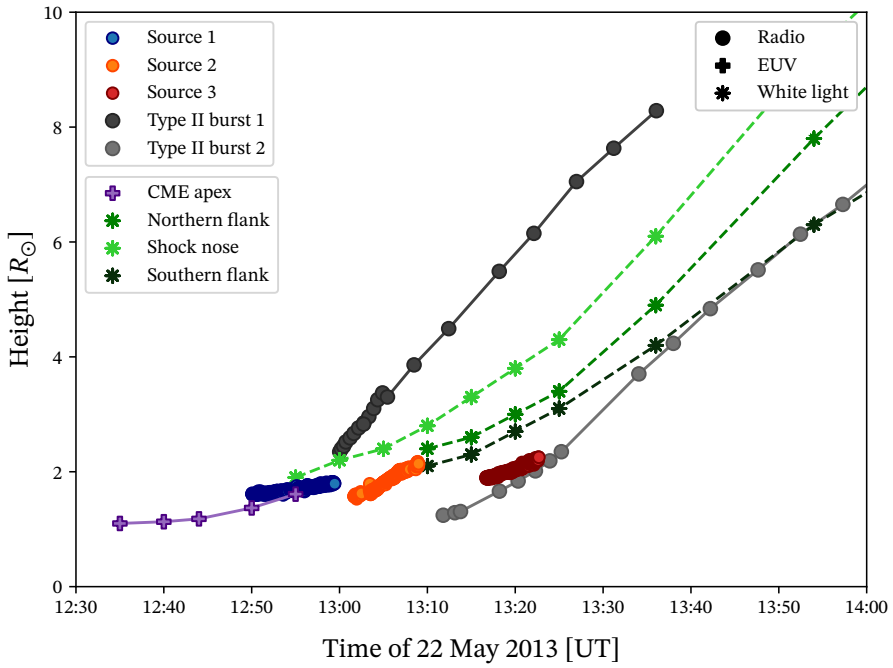

Figure 6.4 Time evolution of the heights of the three moving radio bursts in relation to the kinematic evolution of the CME and two type II radio bursts associated with it, seen in EUV, white light, and radio, and studied by Palmerio et al. (2019). The early evolution of the CME was determined from EUV images taken by PROBA2/SWAP and STEREO/EUVI-A, the later evolution from white-light images taken by SOHO/LASCO and STEREO/COR-A. The type II kinematics were determined from data captured by NDA and Wind/WAVES. The figure is adapted from Palmerio et al. (2019).

from the northern flank of the CME, this height evolution can be explained by noting that Source 2 propagated west, in the same direction as the CME nose. Finally, Source 3 seems to evolve behind the white-light structures of the CME, though its height evolution does match up with the evolution of the second type II radio burst.

The centroids plotted on top of the AIA difference images show that all three radio bursts originated near the northern flank of the CME, relatively high up in the corona. The height profiles show that Source 1 first appeared at a height of about $1.6\,R_\odot$ and propagated to a height of around $1.8\,R_\odot$. During its evolution Source 2 went from a height of $1.6\,R_\odot$ to a height of about $2.1\,R_\odot$. Finally, Source 3 originated from a height of $1.9\,R_\odot$ and moved outwards to a height of about $2.3\,R_\odot$. All the main properties of the three moving radio bursts are summarized in Table 6.1.

Coronagraph images show that the CME that preceded the one studied here (see Section 5.2.1) may have a role in explaining why all of the moving radio bursts were

Table 6.1 The key properties of the three moving radio bursts.

Source	Start time [UT]	End time [UT]	Height range [$R_\odot$]	Speed [km s^{-1}]	Location wrt CME
1	12:50:00	12:59:30	1.6 – 1.8	451	northern flank
2	13:03:30	13:07:00	1.6 – 2.1	1457	northern flank
3	13:17:00	13:22:30	1.9 – 2.3	895	northern flank

observed to be coming from the northern flank of the main CME. The conditions left behind by the preceding CME may also have affected the height at which these radio bursts originated from. Figure 6.5a shows the preceding CME from the point of view of STEREO-A. Figure 6.5b shows the main CME propagating behind the previous ejection. The arrow in the figure indicates the southern flank of the preceding CME (as seen in Figure 6.5a), showing that the main CME expanded partly into the same region, and partly outside of it.

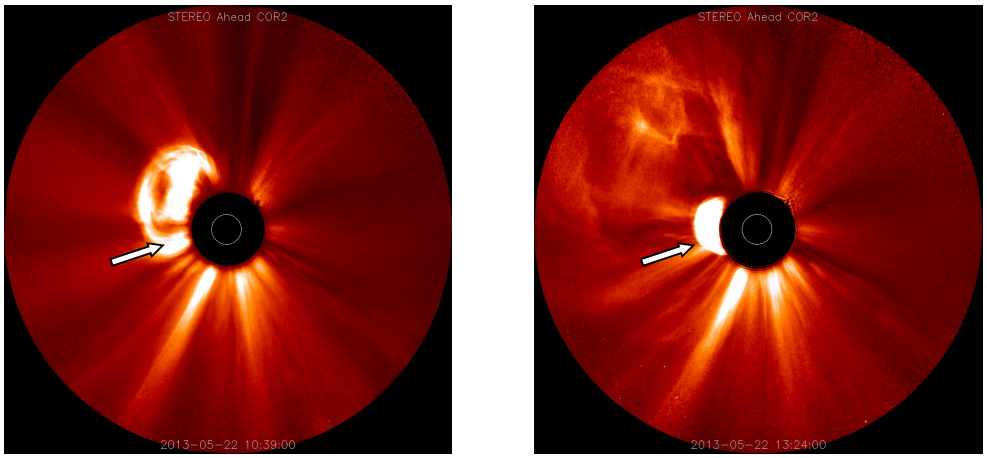

(a) (b)

Figure 6.5 (a) The CME preceding the one studied in this thesis, as seen by STEREO-A/COR2. The arrow indicates the southern flank of the CME. (b) The CME studied in this work as it first appeared in the field of view of STEREO-A/COR2. The preceding CME is clearly visible, covering the upper left quadrant of the image and extending out to the edge of the field of view of COR2. Here too the arrow indicates the southern flank of the preceding CME, showing that the main CME expanded mostly into the same region as the one that came before it. However, the southern flank of the CME expanded outside the region of the preceding CME. Images courtesy of NASA.

The slope of the height-time curve gives an estimate of the radial speed of the propagating feature, though it should be noted that this estimate may be subject to the same projection effects as the speeds estimated from the centroids were. Comparing the heights of the moving radio bursts to those of the CME and the type II radio bursts, we see that Source 1 appeared to be somewhat slower than the CME, even though the speed of the CME itself was low at this point, since Source 1 occurred early in its evolution. The difference in the radial speeds of the features is not large, and it may be that Source 1 propagated either towards the Earth or away from it so that its actual speed was higher than the speed indicated by the observations, more closely matching the speed of the CME at that point of its evolution. The radial speed of Source 2 seems to be higher than the radial speed of the CME, though this is not surprising, as the CME is in a relatively early stage of its evolution and has therefore not yet reached its peak speed, which was around 1500 km s^{-1}. The radial speed of Source 3 appears to be about the same as that of the second type II burst, though the type II is slightly faster. Palmerio et al. (2019) estimated the speed of the second type II to be around 1300 km s^{-1}.

6.3 Radio burst spectral properties

The methods outlined in Sections 5.5 and 5.6 were used to first estimate the flux density of the three moving radio bursts, and based on those results estimate the spectral indices of the bursts. The three plots of Figure 6.6 summarize the results of the analysis. For each radio burst the flux densities at the observed frequencies as well as the estimated spectral indices are shown at one moment in their evolution. As was noted in Section 6.1, all three radio bursts were visible only at 150.9 MHz and 173.2 MHz and not at any of the higher frequencies. Therefore only the flux densities at those two frequencies were used in the power-law fit, from which the spectral index was estimated. It should be noted that the spectral indices can only be taken to be fairly rough estimates, as they were obtained based on a fit done on just two data points. The flux densities for the higher frequencies are the flux densities calculated inside the bounding box chosen for the calculation. As can be seen Figure 6.7, the flux density at the higher frequency comes from random noise, and thus the orange data points in the plots of Figure 6.6 were not used in the power-law fits.

For all three moving bursts the flux density was found to be lower at 173.2 MHz compared to 150.9 MHz, which means that the spectral index of the emission was negative. The spectral index of the first burst was estimated to be $\alpha_1 \approx -4$, while the second and third bursts had spectral indices $\alpha_2 \approx -8$ and $\alpha_3 \approx -8$, respectively. The flux density estimates show that the second radio burst was the strongest of the three, and the first and third bursts were weaker. This observation was also evident in the radio images when viewed over the full evolution of the radio bursts.

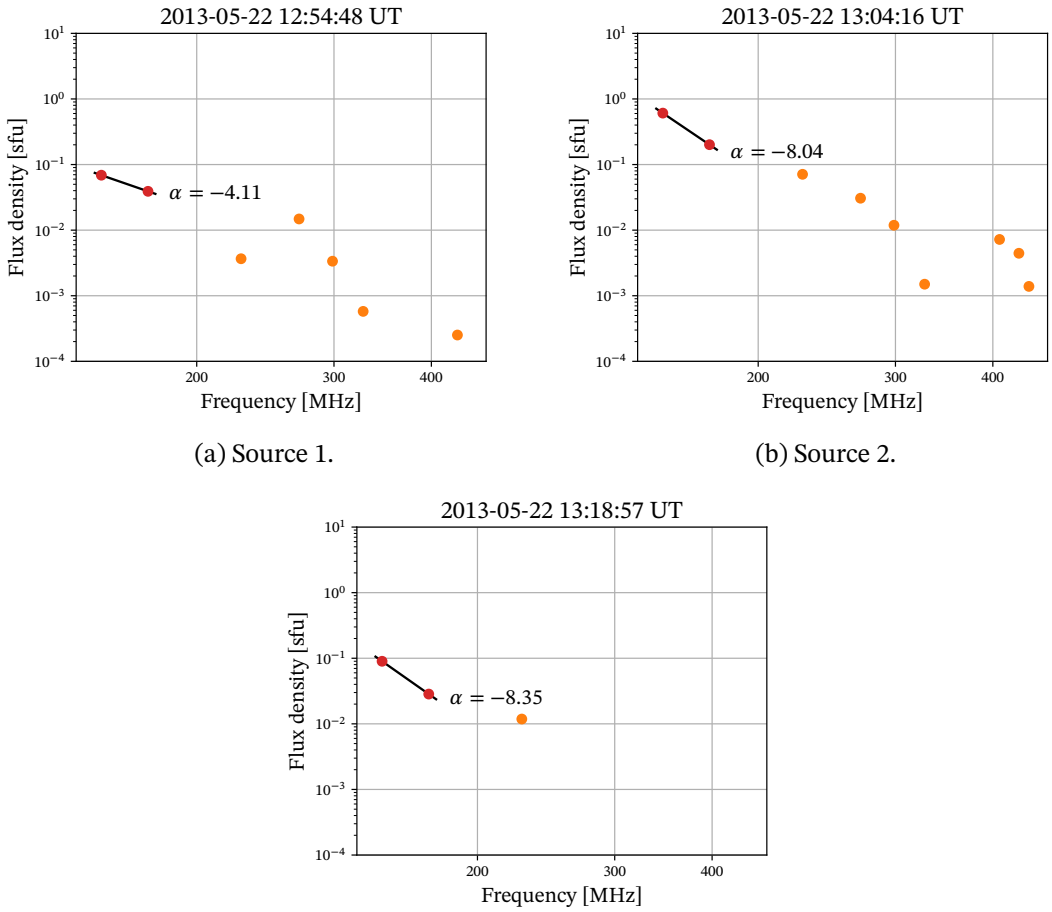

(a) Source 1.

(b) Source 2.

(c) Source 3.

Figure 6.6 The estimated flux densities of the three moving radio bursts at the observed frequencies, along with the spectral indices calculated from the flux density data. The calculation could only be done based on the flux density of the radiation at 150.9 MHz and 173.2 MHz, as the radio bursts were not visible at any of the higher frequencies. For the higher frequencies, which are colored orange, the flux density is from random noise that was present in the same area where the moving radio burst was located.

The steeply negative spectral index exhibited by all three radio bursts indicates that the mechanism by which they were emitted was plasma emission. As noted in Section 4.2, a negative spectral index is indicative of optically thin non-thermal emission. The spectrum of optically thin thermal emission is almost flat, so that the spectral index, while it can be slightly negative, is close to zero. This is not the case here, as the spectral index of Source 1 is around −4, and for Sources 2 and 3 it is closer to −10. Also, the relationship between flux density and frequency resembles the low-frequency part of the flux density spectrum presented for example by Carley et al.

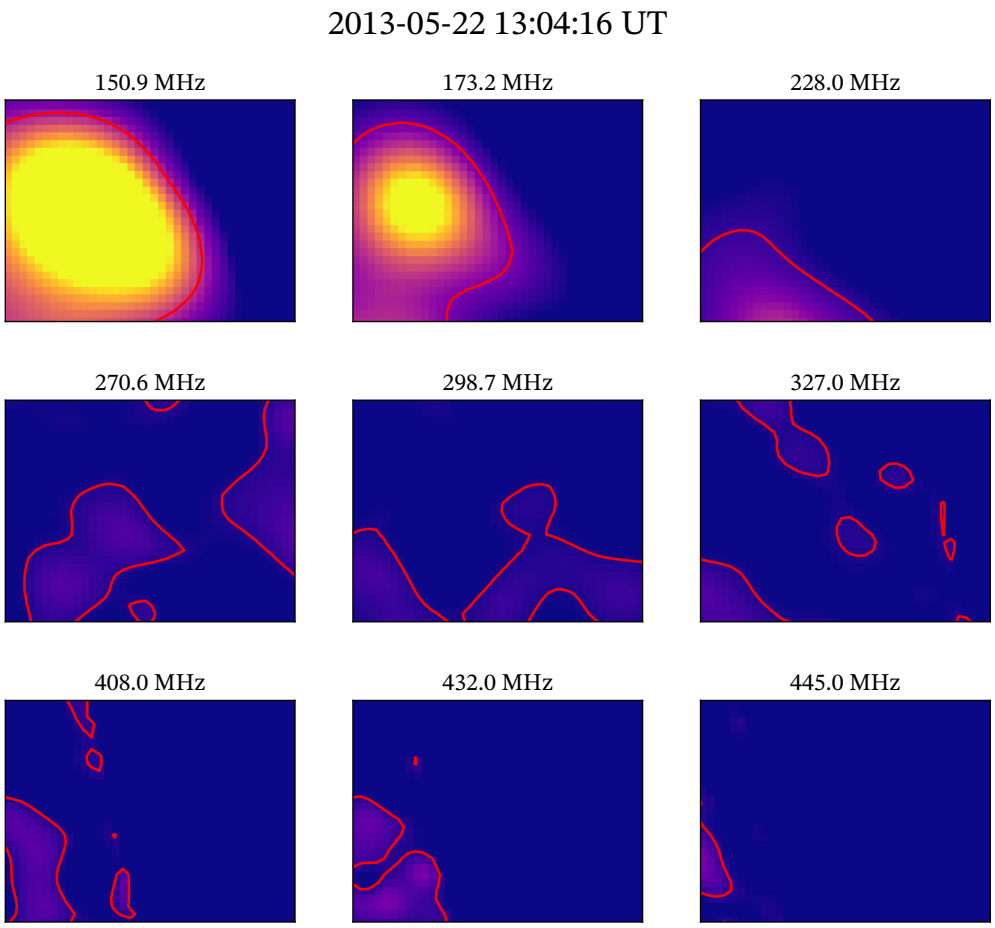

Figure 6.7 The zoomed-in NRH radio images corresponding to Figure 6.6b. The moving radio burst can only be seen at the two lowest frequencies, while the higher frequencies show mostly random noise (at 228 MHz an unrelated transient can be seen in the lower left corner of the frame). The contours indicate 20 % of the maximum intensity inside the frame. When estimating the flux density everything below that threshold was set to zero.

(2017). They conclude that the spectrum is likely dominated by plasma emission. Finally, as noted in Section 3.2.3, at frequencies below the hundreds of MHz range emission from solar radio bursts is mainly due to plasma emission.

7 | Summary and discussion

Analysis of the NRH radio data, the results of which were presented in the previous chapter, revealed three radio bursts that appeared to propagate through the corona along with a fast CME that erupted from close to the western limb of the Sun. None of the three bursts fit the description of any of the five commonly identified radio bursts, most notably types II or IV, both of which were also observed in conjunction with the CME. As Figure 6.2 shows, no radio burst reminiscent of type II or type IV bursts could be seen in the dynamic spectrum around the onset of any of the three moving bursts.

All three radio bursts originated near the northern flank of the CME, relatively high up in the corona. Their heights ranged from 1.6 $R_\odot$, where Sources 1 and 2 first appeared, to 2.3 $R_\odot$, where Source 3 was last observed. There are many models that have been developed for estimating plasma density in the corona and in interplanetary space. These models can be used to estimate the coronal height from which radio emission at a certain frequency may be expected to originate from. Depending on the model used, a fundamental plasma frequency of 150 MHz corresponds to a coronal height of 1.2 $R_\odot$ to 1.4 $R_\odot$ (Pohjolainen et al. 2007). This means that all three radio bursts originated from unusually high up in the corona.

The corona of course is not static, and its prevailing conditions can affect the plasma density. The corona into which the CME erupted was not undisturbed, since the CME was preceded by another ejection some hours earlier (see Section 5.2.1). Coronagraph images and GCS modeling show that the preceding CME expanded in a more northerly direction than the one that followed it (see Figure 6.5 and Palmerio et al. 2019). Therefore, the coronal environment was disturbed mainly at the northern flank and the nose of the main CME, while the southern flank likely expanded into a relatively undisturbed corona.

This suggests that one possible explanation for the atypical height at which the radio bursts were observed may be that the preceding CME perturbed the corona, resulting in an enhanced plasma density at greater than usual heights, which then facilitated the emission of the observed radio bursts. The magnetic and plasma environment were likely significantly disturbed on the northern side of the CME but

not on the southern side. This is also a likely explanation for why the moving radio bursts were only observed on the northern flank of the CME, with none coming from the southern flank.

For all three moving radio bursts the emission mechanism is likely to be plasma emission. One strong indicator of the bursts being emitted via plasma emission is the steeply negative spectral index that each burst was found to have. Another factor indicating plasma emission is that the emissions from the radio bursts had high brightness temperatures. High brightness temperature is characteristic of coherent emission (see Section 3.1.1), which in this case means plasma emission.

The observations of type II radio bursts indicate the presence of a CME-driven shock wave. There are several factors that suggest that the moving radio bursts were emitted by electrons accelerated at this shock. First is the fact that all three radio bursts propagated outwards, following the expansion of the CME through the corona. Second, based on the kinematic evolution of the CME and the radio bursts (see Figure 6.4) Source 2 appeared to be faster than the CME features that were seen in white light around the same time. Shocks driven by CMEs can be faster than the CMEs themselves (e.g., Manuel-Hernandez et al. 2013), which suggests that the emitting electrons of Source 2 may be moving with the shock. The first type II, which was observed around the same time as Source 2, is also faster than the CME, and type IIs are emitted by electrons accelerated at the shock. This could mean that the type II and Source 2 had the same source, namely the shock driven by the CME. Then, since the three moving radio bursts were closely connected not only temporally but also in their positions relative to the CME/shock, it stands to reason that all three bursts were emitted at the shock. This also supports the moving radio bursts having been emitted by plasma emission rather than for example gyrosynchrotron emission.

If the moving bursts were emitted by electrons accelerated at the shock, the acceleration mechanism is likely to be shock drift acceleration. However, most likely there are differences between the acceleration regions of the type II bursts and those of the moving radio sources. This is because the type II bursts are brighter and much longer-lasting than the three moving bursts studied in this thesis. This suggests that the electron acceleration that resulted in the type II emission was much more efficient and sustained than the acceleration that caused the observed moving radio sources. It may be that the type II emission and the moving radio bursts originated from different regions of the shock so that the orientation between the upstream magnetic field and the shock front was different for the different bursts. As was seen in Section 2.5, this orientation can greatly affect the efficiency of particle acceleration at the shock, and hence the strength and duration of resulting radio emission.

It could also be that the upstream magnetic field underwent rapid changes due to turbulence caused by the preceding CME, and the changes in the magnetic field caused the efficiency of particle acceleration to change on a short timescale, leading to the observed emission. Some geometries of the magnetic field and shock front,

e.g., one in which the magnetic field lines intersect the shock at two points, can lead to small energy gains (see, e.g., Sandroos and Vainio 2006), which could in turn cause short-lived radio bursts such as the ones studied in this thesis.

7.1 Limitations

There are some factors in the analysis done for this thesis that are sources of uncertainty. One is that there is a degree of subjectivity in determining for example when exactly a burst first appeared and when it vanished. It may be for example that there is a stationary transient that flickers in and out around the location where a moving burst eventually appears and starts its movement, and someone might consider the stationary and moving bursts as the same burst while someone may consider them as separate events. This of course does not necessarily have any effect on the analysis when looking at kinematics, if one only takes into account the movement of the bursts, disregarding any stationary stages at the start or the end of their evolution.

When calculating the centroids or estimating the flux density of the radio bursts some random error may be introduced to the results of the analysis. The error comes about if there is at some point some short-lived, relatively strong emission, for example at the edge of the bounding box of the moving burst that is not filtered out when removing the background emission. An example of this can be seen in Figure 6.7, where at 173.2 MHz the contour, which indicates the threshold outside of which everything is set to zero, does not loop around the burst but rather curves out to the edge of the zoomed-in view. This means that the emission seen at the lower left corner of the view contributes to the estimated flux density of the burst, even though it clearly is not part of the moving burst being studied.

This error can be minimized if in the calculation the bounding box is chosen to be so small that it only contains the burst and not its entire trajectory. Then, as the burst propagates out of the bounding box the box is shifted so that it again contains the burst. This procedure is then repeated for the whole time that the burst moves. This way of calculating the centroids or the flux density can become quite cumbersome depending on the number of times the box is shifted, but it does reduce error.

There is some systematic error present in the estimated flux densities of the radio bursts. This error comes about from using the small-solid angle approximation for the solid angle subtended by the Sun when calculating the solid angle one pixel in the NRH images corresponds to. A more accurate number would have been reached if the solid angle subtended by the Sun, $\Omega_\odot$, would have been calculated from the definition of solid angle, $\Omega_\odot = A_\odot/d^2$, where $A_\odot$ is the area of the solar disk and d is the average distance from the Earth to the Sun. Comparing the solid angle corresponding to one pixel given by this method to the one used in the analysis shows that there is a little over 6 % difference between the numbers, with the one used be-

ing higher. The error introduced by the approximation is therefore not high. And when estimating flux density, this error affects the flux density at every frequency the same way, and what was of interest in the analysis was not what the actual flux density at any given frequency is. Rather how the flux density behaves as a function of frequency was of interest, and this behavior is not changed by the systematic error outlined above. The error caused by the small-solid angle approximation only serves to shift the flux density estimates up or down, with the shift being the same for all data points. Thus, this systematic error does not affect the spectral index and therefore the results of the analysis, at least when it comes to this source of error, can be considered as accurate. There is, however, some uncertainty that is introduced by the fact that only two data points could be used for estimating the spectral index of each radio burst. Still, the general relationship between frequency and flux density is evident in the results, so that the spectral indices can be used to support the conclusion that the bursts were a result of plasma emission.

7.2 Outlook

In this thesis moving radio bursts associated with a coronal mass ejection were analyzed. The study of radio bursts such as the ones that were identified in this work is of particular interest, as their characteristics clearly depart from those of the commonly known and widely studied solar radio bursts. Another factor that made the bursts studied in this thesis atypical was that they originated from higher up in the corona than would be expected from radiation of a similar frequency that resulted from plasma emission.

The work presented in this thesis shows that relatively straightforward data analysis techniques can effectively be employed to yield information on atypical radio emission observed in conjunction with CMEs. The aim of this thesis was to investigate the nature and the origin of these types of radio bursts, meaning what is the emitting structure and by what mechanism is the radio emission produced. It was found that the moving bursts were related to electrons that were accelerated by a shock driven by the CME, resulting in radiation produced via the plasma emission mechanism. The emission was also identified as likely having originated from the northern flank of the CME. With these conclusions, the aim of the thesis was met.

The results of the analysis relied on earlier work done on the CME in question, as what allowed many of the properties to be identified was relating the features of the moving bursts to those of other radio bursts that were studied in earlier works. When it comes to studying the radio emission associated with the CME, those earlier works mostly focused on the spectra of the emission. They did not take advantage of radio imaging and the unique perspective it provides on plasma processes occurring due to the CME.

Further analysis of the moving radio bursts and the CME, and how the interaction between this CME and the one that preceded it contributed to the observed radio emission, has been conducted in a recent article by Morosan et al. (2020). The author of this thesis contributed to the identification of the moving radio bursts and the analysis of the kinematics of the bursts, as presented in the above work.

There are a number of avenues for further research. Regarding the event studied in this thesis, it may be interesting to take a closer look at the stationary type IV radio burst that was seen in the ORFEES dynamic spectrum (Figure 6.2). The type IV extended over all of the frequencies monitored by NRH, and its source region was visible at all the frequencies in the radio images. Therefore the methods from Sections 5.5 and 5.6 could be used to study the spectral properties of the burst. Calculating the flux density of the burst at all of the nine frequencies would most likely enable the spectral index of the burst to be estimated fairly accurately. Visual inspection of the burst also shows that it appears to be a pulsating continuum, and this can have many implications on the acceleration mechanism that produced the observed emission.

Another way the research on this particular CME could be extended to is to study the properties of the shock driven by the ejection more closely. One important parameter of a shock wave is the *Alfvén Mach number* M_{A}, which is the ratio of the speed of the shock's driver to the local Alfvén speed (Priest 2014). The Alfvén Mach number can be used as a measure of the compression of plasma and magnetic field at the shock front, a higher M_{A} implying more compression. There are a number of techniques that can be used to calculate the Alfvén Mach number of the CME-driven shock. Maguire et al. (2020) have compared three techniques, one using the shock's standoff distance (distance from the leading edge of the CME to the shock front), one which determines it from the ratio $v_{\mathrm{CME}}/v_{\mathrm{A}}$, and one using the relative bandwidth of a band-split type II radio burst. At least the first one of these could be applied to the CME studied in this thesis, and if a reliable estimate of the Alfvén speed could be determined, the second technique could also be used.

Regarding this CME and other events like it, what the analysis in this thesis showed is that preconditioning of the corona by a preceding CME may have important implications for the production of atypical radio bursts. Therefore, it would be interesting to study the radio emission associated with other similar events, in which a CME erupts behind another CME, in detail. Such studies may provide more information on how a preceding CME affects the nature of observed radio emission, if it indeed is the case for example that the conditions left behind by the CME facilitate the production of radio bursts at greater than expected heights in the corona.

Other radio events similar to the ones described here could also be studied using more modern and accurate instruments. For example, with the LOw-Frequency ARray (LOFAR; van Haarlem et al. 2013), radio images of the Sun with much better resolution are achievable compared to NRH. This means that for example the source

regions of radio bursts such as the ones studied in this thesis could be located more accurately. Also, the frequency coverage is much better with LOFAR than it is with NRH. Whereas NRH observes the Sun at nine frequencies, LOFAR observes the Sun at two frequency ranges, 30 – 80 MHz and 110 – 240 MHz, and with a nearly continuous coverage of those ranges. This enables the spectral properties of radio bursts to be studied in more detail, and the spectral indices to be determined more accurately.

In addition to high-resolution imaging of radio bursts, in situ observations of the plasma conditions responsible for producing the bursts are possible with for example the instruments on board the Parker Solar Probe (PSP; Fox et al. 2016), which is the first spacecraft that will fly into the low solar corona. On board, PSP has instruments that can measure the coronal electric and magnetic fields, as well as investigate energetic electrons and other charged particles as they are being accelerated for example by shocks in the corona. As was seen earlier, the orientation of the magnetic field relative to the shock is an important factor in determining the efficiency of particle acceleration, so direct measurements of the shock properties and magnetic field will provide valuable insights into the kinds of solar radio bursts studied in this thesis.

Bibliography

Alissandrakis, C. E., Lantos, P., and Nicolaidis, E. (1985), "Coronal structures observed at metric wavelengths with the Nançay Radioheliograph," *Solar Phys.* **97**, 267–282, doi:10.1007/BF00165990.

Argiroffi, C., Reale, F., Drake, J. J., Ciaravella, A., Testa, P., Bonito, R., Miceli, M., Orlando, S., and Peres, G. (2019), "A stellar flare–coronal mass ejection event revealed by X-ray plasma motions," *Nat. Astron.* **3**, 742–748, doi:10.1038/s41550-019-0781-4.

Aschwanden, M. J. (2006), *Physics of the Solar Corona* (Springer, Berlin), doi:10.1007/3-540-30766-4.

The Astropy Collaboration, Robitaille, T. B., Tollerud, E. J., Greenfield, P., Droettboom, M., Bray, E., Aldcroft, T., Davis, M., Ginsburg, A., Price-Wheelan, A. M., Kerzendorf, W. E., Conley, A., Crighton, N., Barbary, K., Muna, D., Ferguson, H., Grollier, F., Parikh, M. M., Nair, P. H., Günther, H. M., Deil, C., Woillez, J., Conseil, S., Kramer, R., Turner, J. E. H., Singer, L., Fox, R., Weaver, B. A., Zabalza, V., Edwards, Z. I., Bostroem, K. A., Burke, D. J., Casey, A. R., Crawford, S. M., Dencheva, N., Ely, J., Jenness, T., Labrie, K., Lim, P. L., Pierfederici, F., Pontzen, A., Ptak, A., Refsdal, B., Servillat, M., and Streicher, O. (2013), "Astropy: A community Python package for astronomy," *Astron. Astrophys.* **558**, A33, doi:10.1051/0004-6361/201322068.

The Astropy Collaboration, Price-Wheelan, A. M., Sipőcz, B. M., Günther, H. M., Lim, P. L., Crawford, S. M., Conseil, S., Shupe, D. L., Craig, M. W., Dencheva, N., Ginsburg, A., VanderPlas, J. T., Bradley, L. D., Pérez-Suárez, D., de Val-Borro, M., Aldcroft, T. L., Cruz, K. L., Robitaille, T. B., Tollerud, E. J., et al. (2018), "The Astropy project: Building an open-science project and status of the v2.0 core package," *Astrophys. J.* **156**, 123, doi:10.3847/1538-3881/aabc4f.

Bain, H. M., Krucker, S., Saint-Hilaire, P., and Raftery, C. L. (2014), "Radio imaging of a type IVm radio burst on the 14th of August 2010," *Astrophys. J.* **782**, 43, doi:10.1088/0004-637X/782/1/43.

Ball, L. and Melrose, D. B. (2001), "Shock drift acceleration of electrons," *Publ. Astron. Soc. Aust.* **18**, 361–373, doi:10.1071/AS01047.

Bastian, T. S. (2004), "The Frequenvy Agile Solar Radiotelescope," in *Solar and Space Weather Radiophysics: Current Status and Future Developments* (Kluwer Academic Publishers, Dordrecht), 47–69, doi:10.1007/1-4020-2814-8_3.

Bastian, T. S., Benz, A. O., and Gary, D. E. (1998), "Radio emission from solar flares," *Annu. Rev. Astron. Astrophys.* **36**, 131–188, doi:10.1146/annurev.astro.36.1.131.

Bastian, T. S., Pick, M., Kerdraon, A., Maia, D., and Vourlidas, A. (2001), "The coronal mass ejection of 1998 April 20: Direct imaging at radio wavelengths," *Astrophys. J.* **558**, L65–L69, doi:10.1086/323421.

Beiser, A. (2003), *Concepts of Modern Physics* (McGraw-Hill, New York, NY).

Benz, A. O. (2004), "Decimeter burst emission and particle acceleration," in *Solar and Space Weather Radiophysics: Current Status and Future Developments* (Kluwer Academic Publishers, Dordrecht), 203–221, doi:10.1007/1-4020-2814-8_10.

Benz, A. O., Csillaghy, A., and Aschwanden, M. J. (1996), "Metric spikes and electron acceleration in the solar corona," *Astron. Astrophys.* **309**, 291–300.

Benz, A. O. and Thejappa, G. (1988), "Radio emission from coronal shock waves," *Astron. Astrophys.* **202**, 267–274.

Boischot, A., Rosolen, C., Aubier, M. G., Daigne, G., Genova, F., Leblanc, Y., Lecacheux, A., De La Noë, J., and Møller-Pedersen, B. (1980), "A new high-gain, broadband, steerable array to study Jovian decametric emission," *Icarus* **43**, 399–407, doi:10.1016/0019-1035(80)90185-2.

Bougeret, J.-L., Goetz, K., Kaiser, M. L., Bale, S. D., Kellogg, P. J., Maksimovic, M., Monge, N., Monson, S. J., Astier, P. L., Davy, S., Dekkali, M., Hinze, J. J., Manning, R. E., Aguilar-Rodriguez, E., Bonnin, X., Briand, C., Cairns, I. H., Cattell, C. A., Cecconi, B., Eastwood, J., Ergun, R. E., Fainberg, J., Hoang, S., Huttunen, K. E. J., Krucker, S., Lecacheux, A., MacDowall, R. J., Macher, W., Mangeney, A., Meetre, C. A., Moussas, X., Nguyen, Q. N., Oswald, T. H., Pulupa, M., Reiner, M. J., Rovinson, P. A., Rucker, H., Salem, C., Santolik, O., Silvis, J. M., Ullrich, R., Zarka, P., and Zouganelis, I. (2008), "S/WAVES: The Radio and Plasma Wave Investigation on the STEREO mission," *Space Sci. Rev.* **136**, 487–528, doi:10.1007/s11214-007-9298-8.

Bougeret, J.-L., Kaiser, M. L., Kellogg, P. J., Manning, R., Monge, N., Goetz, K., Monson, S. J., Monge, N., Friel, L., Meetre, C. A., Perche, C., Sitruk, L., and Hoang, S. (1995), "WAVES: The Radio and Plasma Wave Investigation on the *Wind* spacecraft," *Space Sci. Rev.* **71**, 231–263, doi:10.1007/BF00751331.

Bougeret, J.-L. and Pick, M. (2007), "Solar radio emissions," in *Handbook of the Solar-Terrestrial Environment* (Springer, Berlin), 133–151, doi:10.1007/978-3-540-46315-3_6.

Boyd, T. J. M. and Sanderson, J. J. (2003), *The Physics of Plasmas* (Cambridge University Press, Cambridge), doi:10.1017/CBO9780511755750.

Brueckner, G. E., Howard, R. A., Koomen, M. J., Korendyke, C. M., Michels, D. J., Moses, J. D., Socker, D. G., Dere, K. P., Lamy, P. L., Llebaria, A., Bout, M. V.,

Schwenn, R., Simnett, G. M., Bedford, D. K., and Eyles, C. J. (1995), "The Large Angle Spectroscopic Coronagraph (LASCO): Visible light coronal imaging and spectroscopy," *Solar Phys.* **162**, 357–402, doi:10.1007/BF00733434.

Burke, B. F., Graham-Smith, F., and Wilkinson, P. N. (2019), *An Introduction to Radio Astronomy* (Cambridge University Press, Cambridge), doi:10.1017/9781316987506.

Cairns, I. H. and Robinson, R. D. (1987), "Herringbone bursts associated with type II solar radio emission," *Solar Phys.* **111**, 365–383, doi:10.1007/BF00148526.

Cane, H. V. and Reames, D. V. (1988a), "Soft X-ray emissions, meter-wavelength radio bursts, and particle acceleration in solar flares," *Astrophys. J.* **325**, 895–900, doi:10.1086/166060.

Cane, H. V. and Reames, D. V. (1988b), "Some statistics of solar radio bursts of spectral types II and IV," *Astrophys. J.* **325**, 901–904, doi:10.1086/166061.

Cargill, P. J. and Harra, L. K. (2007), "Coronal mass ejection," in *Handbook of the Solar-Terrestrial Environment* (Springer, Berlin), 117–132, doi:10.1007/978-3-540-46315-3_5.

Carley, E. P., Vilmer, N., Simões, P. J. A., and Ó Fearraigh, B. (2017), "Estimation of a coronal mass ejection magnetic field strength using radio observations of gyrosynchrotron radiation," *Astron. Astrophys.* **608**, A137, doi:10.1051/0004-6361/201731368.

Carley, E. P., Vilmer, N., and Vourlidas, A. (2020), "Radio observations of coronal mass ejection initiation and development in the low solar corona," *Front. Astron. Space Sci.* **7**, 551558, doi:10.3389/fspas.2020.551558.

Chen, P. F. (2011), "Coronal mass ejections: Models and their observational basis," *Living Rev. Solar Phys.* **8**, 1, doi:10.12942/lrsp-2011-1.

Cheng, X., Ding, M. D., Guo, Y., Zhang, J., Vourlidas, A., Liu, Y. D., Olmedo, O., Sun, J. Q., and Li, C. (2014), "Tracking the evolution of a coherent magnetic flux rope continuously from the inner to the outer corona," *Astrophys. J.* **780**, 28, doi:10.1088/0004-637X/780/1/28.

Clark, B. G. (1995), "Interferometers and coherence theory," in *Very Long Baseline Interferometry and the VLBA*, ASP Conference Series, vol. 82, 3–16.

Clarke, B. P., Morosan, D. E., Gallagher, P. T., Dorovskyy, V. V., Konovalenko, A. A., and Carley, E. P. (2019), "Properties and magnetic origins of solar S-bursts," *Astron. Astrophys.* **622**, A204, doi:10.1051/0004-6361/201833939.

Cliver, E. (2001), "Solar flare classification," in *Encyclopedia of Astronomy and Astrophysics*.

Condon, J. J. and Ransom, S. M. (2016), *Essential Radio Astronomy* (Princeton University Press, Princeton, NJ).

Cornwell, T., Braun, R., and Briggs, D. S. (1999), "Deconvolution," in *Synthesis Imaging in Radio Astronomy II*, ASP Conference Series, vol. 180, 151–170.

Ding, L.-G., Li, G., Jiang, Y., Le, G.-M., Shen, C.-L., Wang, Y.-M., Chen, Y., Xu, F., Gu, B., and Zhang, Y.-N. (2014), "Interaction between two coronal mass ejections in the 2013 May 22 large solar energetic particle event," *Astrophys. J. Lett.* **793**, L35, doi:10.1088/2041-8205/793/2/L35.

Domingo, V., Fleck, B., and Poland, A. I. (1995a), "SOHO: The Solar and Heliospheric Observatory," *Space Sci. Rev.* **72**, 81–84, doi:10.1007/bf00768758.

Domingo, V., Fleck, B., and Poland, A. I. (1995b), "The SOHO mission: An overview," *Solar Phys.* **162**, 1–37, doi:10.1007/bf00733425.

Dulk, G. A. (1985), "Radio emission from the Sun and stars," *Annu. Rev. Astron. Astrophys.* **23**, 169–224, doi:10.1146/annurev.aa.23.090185.001125.

ESA (2019), SOHO: Fact sheet, `https://sci.esa.int/web/soho/-/47368-fact-sheet` [accessed 29 September 2020].

Emilio, M. and Leister, N. V. (2005), "Solar diameter measurements at São Paulo Observatory," *Mon. Not. R. Astron. Soc.* **361**, 1005–1011, doi:10.1111/j.1365-2966.2005.09236.x.

Fox, N. J., Velli, M. C., Bale, S. D., Decker, R., Driesman, A., Howard, R. A., Kasper, J. C., Kinnison, J., Kusterer, M., Lario, D., Lockwood, M. K., McComas, D. J., Raouafi, N. E., and Szabo, A. (2016), "The Solar Probe Plus mission: Humanity's first visit to our star," *Space Sci. Rev.* **204**, 7–48, doi:10.1007/s11214-015-0211-6.

Freeland, S. L. and Bentley, R. D. (2001), "SolarSoft," in *Encyclopedia of Astronomy and Astrophysics*.

Freeland, S. L. and Handy, B. N. (1998), "Data analysis with the SolarSoft system," *Solar Phys.* **182**, 497–500, doi:10.1023/A:1005038224881.

Gary, D. E., Dulk, G. A., House, L. L., Illing, R., Wagner, W. J., and McLean, D. J. (1985), "The type IV burst of 1980 June 29, 0233 UT: Harmonic plasma emission?" *Astron. Astrophys.* **152**, 42–50.

Gary, D. E. and Hurford, G. J. (2004), "Radio spectral diagnostics," in *Solar and Space Weather Radiophysics: Current Status and Future Developments* (Kluwer Academic Publishers, Dordrecht), 71–87, doi:10.1007/1-4020-2814-8_4.

Gelfreikh, G. B. (2004), "Coronal magnetic field measurements through bremsstrahlung emission," in *Solar and Space Weather Radiophysics: Current Status and Future Developments* (Kluwer Academic Publishers, Dordrecht), 115–133, doi:10.1007/1-4020-2814-8_6.

Gonzalez, W. D., Joselyn, J. A., Kamide, Y., Kroehl, H. W., Rostoker, G., Tsurutani, B. T., and Vasyliunas, V. M. (1994), "What is a geomagnetic storm?" *J. Geophys. Res.* **99**, 5771–5792, doi:10.1029/93JA02867.

Gopalswamy, N. (2006), "Coronal mass ejections and type II radio bursts," in *Solar eruptions and energetic particles* (American Geophysical Union, Washington, D.C.), 207–220, doi:10.1029/165GM20.

Gopalswamy, N. (2011), "Coronal mass ejections and solar radio emissions," in *Proceedings of the 7th International Workshop on Planetary, Solar and Heliospheric Radio Emissions*, 325–342.

Gopalswamy, N., Xie, H., Akiyama, S., Mäkelä, P. A., and Yashiro, S. (2014), "Major solar eruptions and high-energy particle events during solar cycle 24," *Earth Planets Space* **66**, 104, doi:10.1186/1880-5981-66-104.

Gopalswamy, N., Yashiro, S., and Akiyama, S. (2007), "Geoeffectiveness of halo coronal mass ejections," *J. Geophys. Res.* **112**, A06112, doi:10.1029/2006JA012149.

Gopalswamy, N., Yashiro, S., Michalek, G., Stenborg, G., Vourlidas, A., Freeland, S., and Howard, R. (2009), "The SOHO/LASCO CME Catalog," *Earth Moon Planets* **104**, 295–313, doi:10.1007/s11038-008-9282-7.

Halain, J.-P., Berghmans, D., Seaton, D. B., Nicula, B., De Groof, A., Mierla, M., Mazzoli, A., Defise, J.-M., and Rochus, P. (2013), "The SWAP EUV Imaging Telescope part II: In-flight performance and calibration," *Solar Phys.* **286**, 67–91, doi:10.1007/s11207-012-0183-6.

Harris, C. R., Millman, K. J., van der Walt, S. J., Gommers, R., Virtanen, P., Cournapeau, D., Wieser, E., Taylor, J., Berg, S., Smith, N. J., Kern, R., Picus, M., Hoyer, S., van Kerkwijk, M. H., Brett, M., Haldane, A., Fernández del Río, J., Wiebe, M., Peterson, P., Gérard-Marchant, P., Sheppard, K., Reddy, T., Weckesser, W., Abbasi, H., Gohlke, C., and Oliphant, T. E. (2020), "Array programming with NumPy," *Nature* **585**, 357–362, doi:10.1038/s41586-020-2649-2.

Holman, G. D. and Pesses, M. E. (1983), "Solar type II radio emission and the shock drift acceleration of electrons," *Astrophys. J.* **267**, 837–843, doi:10.1086/160918.

Howard, R. A. (2006), "A historical perspective on coronal mass ejections," in *Solar eruptions and energetic particles* (American Geophysical Union, Washington, D.C.), 7–13, doi:10.1029/165GM03.

Howard, R. A., Moses, J. D., Vourlidas, A., Newmark, J. S., Socker, D. G., Plunkett, S. P., Korendyke, C. M., Cook, J. W., Hurley, A., Davila, J. M., Thompson, W. T., St Cyr, O. C., Mentzell, E., Mehalick, K., Lemen, J. R., Wuelser, J. P., Duncan, D. W., Tarbell, T. D., Wolfson, C. J., Moore, A., Harrison, R. A., Waltham, N. R., Lang, J., Davis, C. J., Eyles, C. J., Mapson-Menard, H., Simnett, G. M., Halain, J. P., Defise, J. M., Mazy, E., Rochus, P., Mercier, R., Ravet, M. F., Delmotte, F., Auchere, F., Delaboudiniere, J. P., Bothmer, V., Deutsch, W., Wang, D., Rich, N., Cooper, S., Stephens, V., Maahs, G., Baugh, R., McMullin, D., and Carter, T. (2008), "Sun Earth Connection Coronal and Heliospheric Investigation (SECCHI)," *Space Sci. Rev.* **136**, 67–115, doi:10.1007/s11214-008-9341-4.

Howard, T. (2011), *Coronal Mass Ejections: An Introduction* (Springer, New York, NY), doi:10.1007/978-1-4419-8789-1.

Howard, T. (2014), *Space Weather and Coronal Mass Ejections* (Springer, New York, NY), doi:10.1007/978-1-4614-7975-8.

Hundhausen, A. J., Burkepile, J. T., and St. Cyr, O. C. (1994), "Speeds of coronal mass ejections: SMM observations from 1980 and 1984–1989," *J. Geophys. Res.* **99**, 6543–6552, doi:10.1029/93JA03586.

Högbom, J. A. (1974), "Aperture synthesis with a non-regular distribution of interferometer baselines," *Astron. Astrophys. Suppl.* **15**, 417–426.

Illing, R. M. E. and Hundhausen, A. J. (1983), "Possible observation of a disconnected magnetic structure in a coronal transient," *J. Geophys. Res.* **88**, 10 210–10 214, doi:10.1029/JA088iA12p10210.

Illing, R. M. E. and Hundhausen, A. J. (1985), "Observation of a coronal transient from 1.2 to 6 solar radii," *J. Geophys. Res.* **90**, 275–282, doi:10.1029/JA090iA01p00275.

Jackson, N. (2008), "Principles of interferometry," in *Jets from Young Stars II,* Lecture Notes in Physics, vol. 742 (Springer, Berlin), 193–218, doi:10.1007/978-3-540-68032-1_9.

Johnson-Groh, M. (2020), "Ten Things We've Learned About the Sun From NASA's SDO This Decade", https://www.nasa.gov/feature/goddard/2020/ten-things-we-ve-learned-about-the-sun-from-nasa-s-sdo-this-decade [accessed 10 September 2020].

Kaiser, M. L., Kucera, T. A., Davila, J. M., St. Cyr, O. C., Guhathakurta, M., and Christian, E. (2008), "The STEREO mission: An introduction," *Space Sci. Rev.* **136**, 5–16, doi:10.1007/978-0-387-09649-0_2.

Kamide, Y. and Maltsev, Y. P. (2007), "Geomagnetic storms," in *Handbook of the Solar-Terrestrial Environment* (Springer, Berlin), 117–132, doi:10.1007/978-3-540-46315-3_14.

Kerdraon, A. and Delouis, J. M. (1997), "The Nançay Radioheliograph," in *Coronal physics from radio and space observations: Proceedings of the CESRA workshop held in Nouan le Fuzelier, France, 3–7 June 1996* (Springer, Berlin), 192–201, doi:10.1007/BFb0106458.

Kilpua, E. K. J., Lugaz, N., Mays, M. L., and Temmer, M. (2019), "Forecasting the structure and orientation of earthbound coronal mass ejections," *Space Weather* **17**, 498–526, doi:10.1029/2018SW001944.

Kivelson, M. G. and Russell, C. T. (1995), *Introduction to Space Physics* (Cambridge University Press, Cambridge), doi:10.1017/9781139878296.

Koskinen, H. E. J. (2011), *Physics of Space Storms: From the Solar Surface to the Earth* (Springer, Berlin), doi:10.1007/978-3-642-00319-6.

Krall, N. A. and Trivelpiece, A. W. (1973), *Principles of Plasma Physics* (McGraw-Hill, New York, NY).

Kumari, A., Morosan, D. E., and Kilpua, E. K. J. (2021), "On the occurrence of type IV solar radio bursts in solar cycle 24 and their association with coronal mass ejections," *Astrophys. J.* **906**, 79, doi:10.3847/1538-4357/abc878.

Lemen, J. R., Title, A. M., Akin, D. J., Boerner, P. F., Chou, C., Drake, J. F., Duncan, D. W., Edwards, C. G., Frielaender, F. M., Heyman, G. F., Hurlburt, N. E., Katz, N. L., Kushner, G. D., Levay, M., Lindgren, R. W., Mathur, D. P., McFeaters, E. L., Mitchell, S., Rehse, R. A., Schrijver, C. J., Springer, L. A., Stern, R. A., Tarbell, T. D., Wuelser, J.-P., Wolfson, C. J., Yannari, C., Bookbinder, J. A., Cheimets, P. N., Caldwell, D., Deluca, E. E., Gates, R., Golub, L., Park, S., Podgorski, W. A., Bush, R. I., Scherrer, P. H., Gummin, M. A., Smith, P., Auker, G., Jerram, P., Pool, P., Soufli, R., Windt, D. L., Beardsley, S., Clapp, M., Lang, J., and Waltham, N. (2012), "The Atmospheric Imaging Assembly (AIA) on the Solar Dynamics Observatory (SDO)," *Solar Phys.* **275**, 17–40, doi:10.1007/s11207-011-9776-8.

Liu, H., Chen, Y., Cho, K., Feng, S., Vasanth, V., Koval, A., Du, G., Wu, Z., and Li, C. (2018), "A solar stationary type IV radio burst and its radiation mechanism," *Solar Phys.* **293**, 58, doi:10.1007/s11207-018-1280-y.

Magdalenić, J., Marqué, C., Zhukov, A. N., Vršnak, B., and Žic, T. (2010), "Origin of coronal shock waves associated with slow coronal mass ejections," *Astrophys. J.* **718**, 266–278, doi:10.1088/0004-637X/718/1/266.

Magdalenić, J., Vršnak, B., Zlobec, P., Hillaris, A., and Messerotti, M. (2006), "Classification and properties of supershort solar radio bursts," *Astrophys. J.* **642**, L77–L80, doi:10.1086/504521.

Maguire, C. A., Carley, E. P., McCauley, J., and Gallagher, P. T. (2020), "Evolution of the Alfvén Mach number associated with a coronal mass ejection shock," *Astron. Astrophys.* **633**, A56, doi:10.1051/0004-6361/201936449.

Mahrous, A., Alielden, K., Vršnak, B., and Youssef, M. (2018), "Type II solar radio burst band-splitting: Measure of coronal magnetic field strength," *J. Atmos. Sol. Terr. Phys.* **172**, 75–82, doi:10.1016/j.jastp.2018.03.018.

Maia, D. J. F., Gama, R., Mercier, C., Pick, M., Kerdraon, A., and Karlický, M. (2007), "The radio-coronal mass ejection event on 2001 April 15," *Astrophys. J.* **660**, 874–881, doi:10.1086/508011.

Maia, D., Pick, M., and Vourlidas, A. (1999a), "Development of coronal mass ejections: Radio shock signatures," in *Proceedings of the 8th SOHO Workshop 'Plasma Dynamics and Diagnostics in the Solar Transition Region and Corona', Paris, France, 22–25 June 1999*, 473–476.

Maia, D., Vourlidas, A., Pick, M., Howard, R., Schwenn, R., and Magalhães, A. (1999b), "Radio signatures of a fast coronal mass ejection development on November 6, 1997," *J. Geophys. Res.* **104**, 12507–12513, doi:10.1029/1999JA900033.

Mann, G. (1994), "Radio emission from quasi-parallel shock waves in the corona," *Space Sci. Rev.* **68**, 199–203, doi:10.1007/BF00749138.

Mann, G. and Klassen, A. (2002), "Shock accelerated electron beams in the solar corona," in *Proceedings of the 10th European Solar Physics Meeting 'Solar Variabil-*

ity: From Core to Outer Frontiers', Prague, Czech Republic, 9–14 September 2002, 245–248.

Mann, G. and Klassen, A. (2005), "Electron beams generated by shock waves in the solar corona," *Astron. Astrophys.* **441**, 319–326, doi:10.1051/0004-6361:20034396.

Manuel-Hernandez, T., Aguilar-Rodriguez, E., Gonzalez-Esparza, J. A., and Ontiveros, V. (2013), "Speed evolution of CME/shocks using multi-spacecraft observations of type II radio bursts: A case study," *AIP Conf. Proc.* **1539**, 235–238, doi:10.1063/1.4811031.

Melnik, V. N., Shevchuk, N. V., Konovalenko, A. A., Rucker, H. O., Dorovskyy, V. V., Poedts, S., and Lecacheux, A. (2014), "Solar decameter spikes," *Solar Phys.* **289**, 1701–1714, doi:10.1007/s11207-013-0434-1.

Melrose, D. B. (1991), "Collective plasma radiation processes," *Annu. Rev. Astron. Astrophys.* **29**, 31–57, doi:10.1146/annurev.aa.29.090191.000335.

Melrose, D. B. (2017), "Coherent emission mechanisms in astrophysical plasmas," *Rev. Mod. Plasma Phys.* **1**, 5, doi:10.1007/s41614-017-0007-0.

Miteva, R. and Mann, G. (2007), "The electron acceleration at shock waves in the solar corona," *Astron. Astrophys.* **474**, 617–625, doi:10.1051/0004-6361:20066856.

Morosan, D. E., Carley, E. P., Hayes, L. A., Murray, S. A., Zucca, P., Fallows, R. A., McCauley, J., Kilpua, E. K. J., Mann, G., Vocks, C., and Gallagher, P. T. (2019a), "Multiple regions of shock-accelerated particles during a solar coronal mass ejection," *Nat. Astron.* **3**, 452–461, doi:10.1038/s41550-019-0689-z.

Morosan, D. E., Kilpua, E. K. J., Carley, E. P., and Monstein, C. (2019b), "Variable emission mechanism of a type IV radio burst," *Astron. Astrophys.* **623**, A63, doi:10.1051/0004-6361/201834510.

Morosan, D. E., Palmerio, E., Räsänen, J. E., Kilpua, E. K. J., Magdalenić, J., Lynch, B. J., Kumari, A., Pomoell, J., and Palmorth, M. (2020), "Electron acceleration and radio emission following the early interaction of two coronal mass ejections," *Astron. Astrophys.* **642**, A151, doi:10.1051/0004-6361/202038801.

Mäkelä, P., Gopalswamy, N., Reiner, M. J., Akiyama, S., and Krupar, V. (2016), "Source regions of the type II radio burst observed during a CME–CME interaction on 2013 May 22," *Astrophys. J.* **827**, 141, doi:10.3847/0004-637X/827/2/141.

Nindos, A. (2020), "Incoherent solar radio emission," *Front. Astron. Space Sci.* **7**, 57, doi:10.3389/fspas.2020.00057.

Nindos, A., Aurass, H., Klein, K.-L., and Trottet, G. (2008), "Radio emission of flares and coronal mass ejections," *Solar Phys.* **253**, 3–41, doi:10.1007/s11207-008-9258-9.

Nita, G. M., Gary, D. E., and Lee, J. (2004), "Statistical study of two years of solar flare radio spectra obtained with the Owens Valley Solar Array," *Astrophys. J.* **605**, 528–545, doi:10.1086/382219.

Ogilvie, K. W. and Desch, M. D. (1997), "The *Wind* spacecraft and its early scientific results," *Adv. Space Res.* **20**, 559–568, doi:10.1016/S0273-1177(97)00439-0.

Palmerio, E., Scolini, C., Barnes, D., Magdalenić, J., West, M. J., Zhukov, A. N., Rodriguez, L., Mierla, M., Good, S. W., Morosan, D. E., Kilpua, E. K. J., Pomoell, J., and Poedts, S. (2019), "Multipoint study of successive coronal mass ejections driving moderate disturbances at 1 AU," *Astrophys. J.* **878**, 37.

Parks, G. K. (2004), *Physics of Space Plasmas: An Introduction* (Westview Press, Boulder, CO).

Pence, W. D., Chiappetti, L., Page, C. G., Shaw, R. A., and Stobie, E. (2010), "Definition of the Flexible Image Transport System (FITS), version 3.0," *Astron. Astrophys.* **524**, A42, doi:10.1051/0004-6361/201015362.

Pesnell, W. D., Thompson, B. J., and Chamberlain, P. C. (2012), "The Solar Dynamics Observatory (SDO)," *Solar Phys.* **275**, 3–15, doi:10.1007/s11207-011-9841-3.

Pesses, M. E. (1981), "On the conservation of the first adiabatic invariant in perpendicular shocks," *J. Geophys. Res.* **86**, 150–152, doi:10.1029/JA086iA01p00150.

Pesses, M. E., Decker, R. B., and Armstrong, T. P. (1982), "The acceleration of charged particles in interplanetary shock waves," *Space Sci. Rev.* **32**, 185–204, doi:10.1007/BF00225184.

Pick, M., Steinberg, J.-L., Orchiston, W., and Boischot, A. (2011), "Highlighting the history of French radio astronomy 6: The multi-element grating arrays at Nançay," *J. Astron. Hist. Herit.* **14**, 57–77.

Pohjolainen, S., van Driel-Gesztelyi, L., Culhane, J. L., Manoharan, P. K., and Elliott, H. A. (2007), "CME propagation characteristics from radio observtions," *Solar Phys.* **244**, 167–188, doi:10.1007/s11207-007-9006-6.

Priest, E. (2014), *Magnetohydrodynamics of the Sun* (Cambridge University Press, New York, NY), doi:10.1017/CBO9781139020732.

Pérez-Suárez, D., Higgins, P. A., Bloomfield, D. S., McAteer, R. T. J., Krista, L. D., Byrne, J. P., and Gallagher, P. T. (2011), "Automated solar feature detection for space weather applications," in *Applied Signal and Image Processing: Multidisciplinary Advancements* (Information Science Reference, Hershey, PA), 207–225, doi:10.4018/978-1-60960-477-6.ch013.

The Radioheliograph Group (1983), "The Mark III Nançay Radioheliograph," *Solar Phys.* **88**, 383–390, doi:10.1007/BF00196201.

The Radioheliograph Group (1993), "The Nançay Multifrequency Radioheliograph: New developments and data acquisition for the solar physics community," *Adv. Space Res.* **13**, (9)411–(9)414, doi:10.1016/0273-1177(93)90513-B.

Rybicki, G. B. and Lightman, A. P. (2004), *Radiative Processes in Astrophysics* (Wiley-VCH, Weinheim), doi:10.1002/9783527618170.

Salas-Matamoros, C. and Klein, K.-L. (2020), "Polarisation and source structure of solar stationary type IV radio bursts," *Astron. Astrophys.* **639**, A102, doi:10.1051/0004-6361/202037989.

Sandroos, A. and Vainio, R. (2006), "Particle acceleration at shocks propagating in inhomogeneous magnetic fields," *Astron. Astrophys.* **455**, 685–695, doi:10.1051/0004-6361:20054754.

Santandrea, S., Gantois, K., Strauch, K., Teston, F., PROBA2 Project Team, Tilmans, E., Baijot, C., Gerrits, D., PROBA2 Industry Team, De Groof, A., Schwehm, G., and Zender, J. (2013), "PROBA2: Mission and spacecraft overview," *Solar Phys.* **286**, 5–19, doi:10.1007/s11207-013-0289-5.

Sarris, E. T. and Van Allen, J. A. (1974), "Effects of interplanetary shock waves on energetic charged particles," *J. Geophys. Res.* **79**, 4157–4173, doi:10.1029/JA079i028p04157.

Seaton, D. B., Berghmans, D., Nicula, B., Halain, J.-P., De Groof, A., Thibert, T., Bloomfield, D. S., Raftery, C. L., Gallagher, P. T., Auchère, F., Defise, J.-M., D'Huys, E., Lecat, J.-H., Mazy, E., Rochus, P., Rossi, L., Schühle, U., Slemzin, V., Yalim, M. S., and Zender, J. (2013), "The SWAP EUV Imaging Telescope part I: Instrument overview and pre-flight testing," *Solar Phys.* **286**, 43–65, doi:10.1007/s11207-012-0114-6.

Smerd, S. F., Sheridan, K. V., and Stewart, R. T. (1974), "On split-band structure in type II radio bursts from the Sun," in *Coronal Disturbances: Proceedings from IAU Symposium no. 57 held at Surfers Paradise, Queensland Australia, 7–11 September, 1973*, 389–393.

Smerd, S. F., Sheridan, K. V., and Stewart, R. T. (1975), "Split-band structure in type II radio bursts from the Sun," *Astrophys. Lett.* **16**, 23–28.

Street, A. G., Ball, L., and Melrose, D. B. (1994), "Shock drift acceleration and type II solar radio bursts," *Publ. Astron. Soc. Aust.* **11**, 21–24, doi:10.1017/S1323358000019603.

The SunPy Community, Barnes, W. T., Bobra, M. G., Christe, S. D., Freij, N., Hayes, L. A., Ireland, J., Mumford, S., Perez-Suarez, D., Ryan, D. F., Shih, A. Y., Chanda, P., Glogowski, K., Hewett, R., Hughitt, V. K., Hill, A., Hiware, K., Inglis, A., Kirk, M. S. F., Konge, S., Mason, J. P., Maloney, S. A., Murray, S. A., Panda, A., Park, J., Pereira, T. M. D., Reardon, K., Savage, S., Sipőcz, B. M., Stansby, D., Jain, Y., Taylor, G., Yadav, T., Rajul, and Dang, T. K. (2020), "The SunPy project: Open source development and status of the version 1.0 core package," *Astrophys. J.* **890**, 68, doi:10.3847/1538-4357/ab4f7a.

Thernisien, A. F. R., Howard, R. A., and Vourlidas, A. (2006), "Modeling of flux rope coronal mass ejections," *Astrophys. J.* **652**, 763–773, doi:10.1086/508254.

Thernisien, A., Vourlidas, A., and Howard, R. (2009), "Forward modeling of coronal mass ejections using STEREO/SECCHI data," *Solar Phys.* **256**, 111–130, doi:10.1007/s11207-009-9346-5.

Thompson, W. T. (2006), "Coordinate systems for solar image data," *Astron. Astrophys.* **449**, 791–803, doi:10.1051/0004-6361:20054262.

van Haarlem, M. P., Wise, M. W., Gunst, A. W., Heald, G., McKean, J. P., Hessels, J. W. T., de Bruyn, A. G., Nijboer, R., Swinbank, J., Fallows, R., Brentjens, M., Nelles, A., Beck, R., Falcke, H., Fender, R., Hörandel, J., Koopmans, L. V. E., Mann, G., Miley, G., Röttgering, H., Stappers, B. W., Wijers, R. A. M. J., Zaroubi, S., van den Akker, M., Alexov, A., Anderson, J., Anderson, K., van Ardenne, A., Arts, M., Asgekar, A., Avruch, I. M., Batejat, F., Bähren, L., Bell, M. E., Bell, M. R., van Bemmel, I., Bennema, P., Bentum, M. J., Bernardi, G., Best, P., Bîrzan, L., Bonafede, A., Boonstra, A.-J., Braun, R., Bregman, J., Breitling, F., van de Brink, R. H., Broderick, J., Broekema, P. C., Brouw, W. N., et al. (2013), "LOFAR: The LOw-Frequency ARray," *Astron. Astrophys.* **556**, A2, doi:10.1051/0004-6361/201220873.

Vasanth, V., Chen, Y., Lv, M., Ning, H., Li, C., Feng, S., Wu, Z., and Du, G. (2019), "Solar imaging of a moving type IV solar radio burst and its role in tracking coronal mass ejection from the inner to the outer corona," *Astrophys. J.* **870**, 30, doi:10.3847/1538-4357/aaeffd.

Virtanen, P., Gommers, R., Oliphant, T. E., Haberland, M., Reddy, T., Cournapeau, D., Burovski, E., Peterson, P., Weckesser, W., Bright, J., van der Walt, S. J., Brett, M., Wilson, J., Millman, K. J., Mayorov, N., Nelson, A. R. J., Jones, E., Kern, R., Larson, E., Carey, C. J., Polat, I., Feng, Y., Moore, E. W., VanderPlas, J., Laxalde, D., Perktold, J., Cimrman, R., Henriksen, I., Quintero, E. A., Harris, C. R., Archibald, A. M., Ribeiro, A. H., Pedregosa, F., van Mulbregt, P., and SciPy 1.0 Contributors, (2020), "SciPy 1.0: fundamental algorithms for scientific computing in Python," *Nat. Methods* **17**, 261–272, doi:10.1038/s41592-019-0686-2.

Vourlidas, A. (2004), "Radio observations of coronal mass ejections," in *Solar and Space Weather Radiophysics: Current Status and Future Developments* (Kluwer Academic Publishing, Dordrecht), 223–242, doi:10.1007/1-4020-2814-8_11.

Vourlidas, A., Howard, R. A., Esfandiari, E., Patsourakos, S., Yashiro, S., and Michalek, G. (2010), "Comprehensive analysis of coronal mass ejection mass energy properties over a full solar cycle," *Astrophys. J.* **722**, 1522–1538, doi:10.1088/0004-637X/722/2/1522.

Vourlidas, A., Howard, R. A., Esfandiari, E., Patsourakos, S., Yashiro, S., and Michalek, G. (2011), "Erratum: "Comprehensive analysis of coronal mass ejection mass energyproperties over a full solar cycle"," *Astrophys. J.* **730**, 59, doi:10.1088/0004-637X/730/1/59.

Vršnak, B., Aurass, H., Magdalenić, J., and Gopalswamy, N. (2001), "Band-splitting of coronal and interplanetary type II bursts: I. Basic properties," *Astron. Astrophys.* **377**, 321–329, doi:10.1051/0004-6361:20011067.

Webb, D. F. and Howard, T. A. (2012), "Coronal mass ejections: Observations," *Living Rev. Sol. Phys.* **3**, 3, doi:10.12942/lrsp-2012-3.

Weiss, A. A. (1963), "The type IV solar radio burst at metre wavelengths," *Aust. J. Phys.* **16**, 526–544, doi:10.1071/PH630526.

White, S. M. (2007), "Solar radio bursts and space weather," *Asian J. Phys.* **16**, 189–207.

Wild, J. P. and Smerd, S. F. (1972), "Radio bursts from the solar corona," *Annu. Rev. Astron. Astrophys.* **10**, 159–196, doi:10.1146/annurev.aa.10.090172.001111.

Wild, J. P., Smerd, S. F., and Weiss, A. A. (1963), "Solar bursts," *Annu. Rev. Astron. Astrophys.* **1**, 291–366, doi:10.1146/annurev.aa.01.090163.001451.

Wilson, T. L., Rohlfs, K., and Hüttemeister, S. (2009), *Tools of Radio Astronomy* (Springer, Berlin), doi:10.1007/978-3-540-85122-6.

Yashiro, S., Gopalswamy, N., Michalek, G., St. Cyr, O. C., Plunkett, S. P., Rich, N. B., and Howard, R. A. (2004), "A catalog of white light coronal mass ejections observed by the SOHO spacecraft," *J. Geophys. Res.* **109**, A07105, doi:10.1029/2003JA010282.

Zhang, J. and Dere, K. P. (2006), "A statistical study of main and residual accelerations of coronal mass ejections," *Astrophys. J.* **649**, 1100–1109, doi:10.1086/506903.

Zhang, J., Dere, K. P., Howard, R. A., Kundu, M. R., and White, S. M. (2001), "On the temporal relationship between coronal mass ejections and flares," *Astrophys. J.* **559**, 452–462, doi:10.1086/322405.